UNIVERSITÀ DEGLI STUDI DI BARI
ALDO MORO

DIPARTIMENTO INTERATENEO DI FISICA "M. MERLIN"

Dottorato di ricerca in FISICA – Ciclo XXX

Settore Scientifico Disciplinare FIS/01

Study of the $^{2}\mathrm{H}(\mathrm{p},\gamma)^{3}\mathrm{He}$ reaction in the Big Bang nucleosynthesis energy range

Dottorando:
Dott. Viviana Mossa

Supervisori:
Ch.mo Dott. Vincenzo Paticchio
Ch.mo Dott. Nicola Colonna

Coordinatore:
Ch.mo Prof. Gaetano Scamarcio

ESAME FINALE 2018

Contents

List of Figures

List of Tables

Abstract

The progress on direct observations of deuterium abundance and the accuracy of CMB data make the lack of ^{2}H(p,γ)^{3}He reaction data at BBN energies the main obstacle to derive the baryon density of the Universe with high accuracy, similar to the one obtained by CMB experiments and to constrain the existence of the so called "dark radiation", composed by undiscovered relativistic species permeating the Universe, such as sterile neutrinos. This is the reason why the LUNA collaboration has measured this reaction cross section in the energy range $30 < E_{cm} < 260$ keV, with the goal of reaching an accuracy of a few percent level to solve the tension between data and nuclear calculations and to improve the current 9% uncertainty quoted in the literature data.

This PhD thesis describes a new experimental campaign on the ^{2}H(p,γ)^{3}He reaction, recently performed by the LUNA collaboration at LNGS, using two different set-ups. The former foresees a deuterium gas target and a high efficiency BGO detector to investigate the low energy range ($30 < E_{cm} < 200$ keV). The second, instead, is based on a High Purity Germanium (HPGe) detector, whose high resolution allows the cross section to be measured also at higher energies (up to $E_{cm} \sim$260 keV) and the distribution of the emitted photons to be evaluated.

The experimental procedure adopted for the ^{2}H(p,γ)^{3}He measurement is described and all the steps for the data reduction are discussed, starting from the analysis of the ancillary measurements of the entire set-up characterization and arriving to the evaluation of the reaction S-factor. The preliminary results are presented, discussing their implications on the primordial deuterium abundance.

The HPGe phase data taking has ended in September 2017 and the data analysis is currently underway. Here the preliminary results about the detector characterization will be shown.

Introduction

The quest for the origin of matter in the Universe has been the subject of philosophical and theological debates over the history of mankind, but quantitative answers could be found only by the scientific achievements of the last years. According to our current knowledge, most of the ordinary matter in the Universe, from a tiny terrestrial pebble to a giant star, is composed of protons and neutrons assembled in a suite of different nuclear configurations. These elements were created by nuclear reactions in the hot interiors of remote and long-vanished stars over many billions of years.
Nuclear fusion reactions are the heart of nuclear astrophysics. They are the fundamental mechanism of the light elements nucleosynthesis in the earliest stages of the Universe and in all the objects formed thereafter and control the associated energy generation, neutrino luminosity and evolution of stars. A good knowledge of the rates of these reactions is thus essential for understanding the broad picture of Universe evolution.

This thesis is focused on the study of the radiative capture $^2\mathrm{H}(\mathrm{p},\gamma)^3\mathrm{He}$, relevant process in many astrophysical environments. In fact it plays a crucial role in the context of the Big Bang Nucleosynthesis (BBN), since it is one of the main processes through which deuterium can be destroyed and thus affects its primordial abundance. Deuterium is the first nucleus produced in the Universe, whose accumulation marked the beginning of the elements nucleosynthesis. Its primordial abundance results to be very sensitive to some cosmological parameters, like the baryon density and the number of neutrinos families, so that their values could be strictly constrained by it.
This reaction also plays an important role in the evolution of protostars. As a cloud of interstellar gas collapses on itself, the gas temperature rises to the point of $^2\mathrm{H}(\mathrm{p},\gamma)^3\mathrm{He}$ ignition, $\sim 10^6$ K. The main effect of the onset of

deuterium burning is to slow down the contraction and, in turn, the heating. As a consequence, the lifetime of the protostar increases and its observational properties (surface luminosity and temperature) are frozen until the original deuterium is fully consumed. Because of the slow evolutionary time scale, a large fraction of observed protostars are in the d-burning phase, while only a few are found in the earlier, cooler, rapidly evolving phase. A reliable knowledge of the rate of ^{2}H(p, γ)^{3}He down to a few keV (the so called Gamow peak) is of fundamental importance for modelling protostellar evolution.

In the present work, the reaction will be studied exactly at the energies of interest for the primordial nucleosynthesis. At first the physical motivations will be discussed and then the experimental procedure for measuring the reaction cross section will be explained. The thesis is developed in four chapters: the first introduces some basic topics of nuclear astrophysics. The calculation of the thermonuclear reaction rate for charged-particle-induced reactions is presented and an explanation of the experimental approach to measure them is given.
The second chapter describes the context of standard cosmology where the ^{2}H(p, γ)^{3}He reaction is placed. A synopsis of the physics relevant to a description of the early evolution of the Universe at the epoch of primordial nucleosynthesis is given, with an outline of the specific nuclear and weak-interaction physics of importance for BBN. A review of the present literature is given as well and the physical motivations for a cross section measurement in the BBN energy range are discussed.
The third chapter is dedicated to the description of the LUNA facility, stressing the attention on the two experimental set-ups used for the measurement.
In the fourth chapter the measurements procedure adopted for the ^{2}H(p, γ)^{3}He reaction is discussed. The analysis of the experimental spectra, describing their features, and the target characterization are also described to arrive, at the end, to the S-factor extrapolation.

CHAPTER 1

Nuclear Astrophysics

Nuclear astrophysics is an extremely rich field, strongly correlated with many other research fields like astronomy, stellar modelling, cosmology, neutrino physics and nuclear physics. One of the most ambitious task of nuclear astrophysics is to explain the origin and the relative abundance of the element in the Universe, formed through different nuclear processes in different astrophysical scenarios and to explain the energy generation in stars in all the stages of their evolution.

This chapter will introduce some of the basic concepts in nuclear astrophysics going through the definition and the general characteristics of thermonuclear reactions.

1.1 Thermonuclear reaction rate

Nuclear fusion reactions play a key role in understanding energy production and nucleosynthesis of the elements. To study how these reactions occur and their impact on energy production and isotopic abundances, two main quantities have to be introduced: the $Q - value$ and the Thermonuclear Reaction Rate [1].
The simplest type of nuclear reaction may be written as $x + A \rightarrow B + y$, where x represents the projectile, A the target nucleus, while y and B the products. The energy conservation implies that

$$m_x c^2 + m_A c^2 + E_x + E_A = m_y c^2 + m_B c^2 + E_y + E_B \tag{1.1}$$

where m and E are respectively the rest mass and the kinetic energy of each interacting particle. Rearranging equation (1.1), it is possible to define the reaction $Q - value$ as

$$Q \equiv m_x c^2 + m_A c^2 - m_y c^2 - m_B c^2 = E_y + E_B - E_x - E_A \qquad (1.2)$$

If Q is positive, there is a net production of energy in the reaction (exothermic reaction); conversely if Q is negative, a minimum energy equal to Q has to be provided to allow the process (endothermic reaction).
The $Q - value$ is thus the energy liberated for each event and could be calculated for nearly all possible nuclear reactions from the mass table. More difficult to measure, instead, is the probability that a given nuclear process will take place. This probability determines how many reactions occur per unit time and unit volume.
Associating with each target nucleus a geometrical area directly related to the probability of a projectile to interact with that nucleus, this area is referred to as the cross section σ for the reaction. Classically, it is equal to the combined geometrical area of the projectile and the target nuclei. Indicating their nuclear radii[1] respectively as R_p and R_t, the cross section will be $\sigma = \pi(R_p + R_t)^2$. In reality, since nuclear reactions are governed by the law of quantum mechanics, the geometrical cross section must be replaced by the energy-dependent quantity $\sigma = \pi\lambda\!\!\!^{-2}$, where $\lambda\!\!\!^{-}$ is the de Broglie wavelength reflecting the wave aspect of quantum mechanical processes:

$$\lambda\!\!\!^{-} = \frac{m_p + m_t}{m_t} \cdot \frac{\hbar}{(2m_p E_l)^{1/2}} \qquad (1.3)$$

with E_l the laboratory incident energy and m_p and m_t the masses of the projectile and the target respectively. In some cases the Coulomb and centrifugal barriers related to nuclear charge and angular momentum act to inhibit the penetration of the incident particle into the target nucleus, leading to a strong energy dependence of the cross section and, equivalently, to a velocity dependence ($\sigma = \sigma(v)$).
Let consider a mixture of two species x and A, with density N_x and N_A. The A nucleus is assumed to be at rest, while x is the projectile. The incoming particle current density is given by $J = vN_x$, where v is the relative velocity between the projectile and the target particle. The target offers to the beam a cross section per unit volume $F = \sigma(v)N_a$, thus the rate of nuclear reactions r is given by the product of both quantities

$$r = N_x N_A v \sigma(v) \qquad (1.4)$$

[1]The nuclear radius R is defined as the distance from the center of the nucleus to the point at which the nuclear density has been reduced by one half. Experimentally the radius is found to vary as $A^{1/3}$, where A is the mass number of the nucleus [2].

In a stellar gas, as in other gases, the velocity of particles varies over a wide range, following a probability distribution $\Phi(v)$ which describes the speed of particles in thermal equilibrium and gives the probability for a particle to have a speed in a certain interval. To calculate a value for $v\Phi(v)$ averaged over the velocity distribution $\langle \sigma v \rangle$, the product $v\sigma(v)$ in equation (1.4) has to be folded with this velocity distribution $\Phi(v)$:

$$\langle \sigma v \rangle = \int_0^\infty \Phi(v) v \sigma(v) dv \tag{1.5}$$

and thus the reaction rate may be written as

$$r = N_x N_A \langle \sigma v \rangle \tag{1.6}$$

In a gas in thermodynamic equilibrium, the nuclei velocities can be described by the Maxwell-Boltzmann distribution:

$$\Phi(v) = 4\pi v^2 \left(\frac{m}{2\pi kT} \right)^{3/2} e^{-mv^2/2kT} \Rightarrow \Phi(E) \propto E \cdot e^{-\frac{E}{kT}} \tag{1.7}$$

where E is the kinetic energy of the nucleus. At low energy, $E \ll kT$, $\Phi(E)$ increases linearly with E and reaches a maximum at $E = kT$. At higher energies, $E \gg kT$, $\Phi(E)$ decreases exponentially, approaching asymptotically to zero at very high energies (figure 1.1) For nuclear reactions in stellar media, the velocities of both the interacting nuclei x and A are described by the Maxwell-Boltzmann distribution

$$\Phi(v_x) = 4\pi v_x^2 \left(\frac{m_x}{2\pi kT} \right)^{3/2} e^{-m_x v_x^2/2kT} \tag{1.8}$$

$$\Phi(v_A) = 4\pi v_A^2 \left(\frac{m_A}{2\pi kT} \right)^{3/2} e^{-m_A v_A^2/2kT} \tag{1.9}$$

Therefore the reaction rate involves a double integral over both distributions:

$$\langle \sigma v \rangle = \int_0^\infty \int_0^\infty \Phi(v_x)\Phi(v_A) v \sigma(v) dv_x dv_A \tag{1.10}$$

The variables v_x and v_A are related to the relative speed v and to the centre of mass speed V by the usual kinematics relations[2] and, indicating with μ and M respectively the reduced mass and the total mass of the interacting particles, the rate can be written as:

$$\langle \sigma v \rangle = \int_0^\infty \int_0^\infty \Phi(V)\Phi(v) v \sigma(v) dV dv \tag{1.11}$$

[2]Relative speed $v = v_x - v_A$, centre of mass speed $V = \frac{m_x}{m_x+m_A} v_x + \frac{m_A}{m_x+m_A} v_A$.

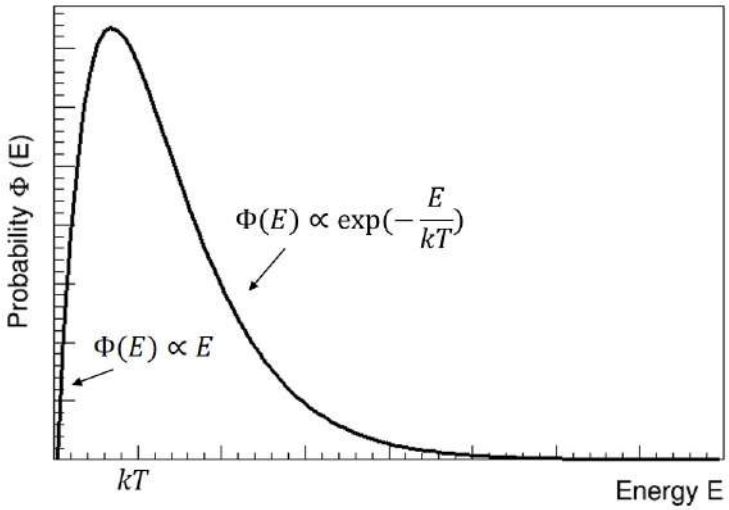

Figure 1.1: Maxwell-Boltzmann energy distribution of a gas at a temperature T.

where the transformed velocity distributions are

$$\Phi(V) = 4\pi V^2 \left(\frac{M}{2\pi kT}\right)^{3/2} e^{-MV^2/2kT} \tag{1.12}$$

$$\Phi(v) = 4\pi v^2 \left(\frac{\mu}{2\pi kT}\right)^{3/2} e^{-\mu v^2/2kT} \tag{1.13}$$

Since the nuclear cross section $\sigma(v)$ depends only on relative velocity v, equation (1.11) can be immediately integrated over the velocity V, obtaining

$$\langle \sigma v \rangle = \int_0^\infty \Phi(v) v \sigma(v) dv \tag{1.14}$$

Inserting equation (1.13), it follows

$$\langle \sigma v \rangle = 4\pi \left(\frac{\mu}{2\pi kT}\right)^{3/2} \int_0^\infty v^3 \sigma(v) e^{-\mu v^2/2kT} dv \tag{1.15}$$

Finally, using the center of mass energy $E = \frac{1}{2}\mu v^2$, this equation can be written in the form

$$\langle \sigma v \rangle = \left(\frac{8}{\pi\mu}\right)^{1/2} \frac{1}{(kT)^{3/2}} \int_0^\infty \sigma(E) E e^{-E/kT} dE. \tag{1.16}$$

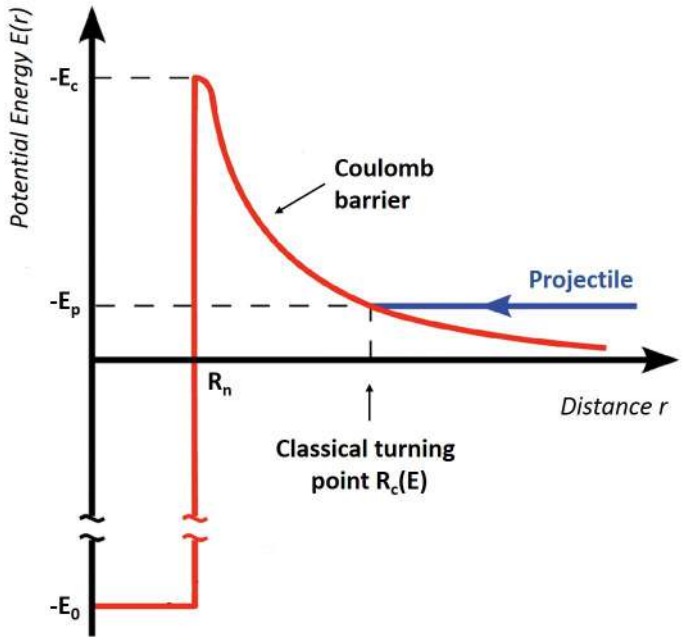

Figure 1.2: Schematic representation of the potential energy due to the combined effect of the Coulomb repulsive force and the nuclear attractive force.

1.2 Charged particle-induced nonresonant reactions

Let's consider the interaction between two nuclei, where the forces in play are both electromagnetic and nuclear. The nuclear force has a very short range, comparable with the dimensions of the interacting nuclei $R_n = R_x + R_A$. At distance smaller than R_n, the nuclear force dominates and the interaction is attractive. At distance larger than R_n, the Coulomb force dominates and the interaction is repulsive. The qualitative behaviour of the potential energy (figure 1.2) can be thus summarized as

$$E_c(r) = \begin{cases} -E_0 & r < R_n \\ \frac{1}{4\pi\epsilon_0}\frac{Z_x Z_A e^2}{r} & r > R_n \end{cases} \tag{1.17}$$

Fusion takes place if the projectile crosses the Coulomb barrier, requiring classically a projectile energy higher than $E_C = \frac{1}{4\pi\epsilon_0}\frac{Z_x Z_A e^2}{R_n}$. This energy corresponds to a temperature ($E = kT$) higher than the one measured inside the stars. Quantum mechanics explains how these reactions can actually occur at lower temperatures. Even though the projectile energy is lower than the Coulomb barrier, a small but finite probability exists for the projectile

to cross the barrier. This is the well known tunnel effect. The tunnelling probability is the ratio of the squared wave function modulus in two different positions:

$$P = \frac{|\Psi(R_n)|^2}{|\Psi(R_c)|^2} \tag{1.18}$$

where R_C is the classical turning point corresponding to the distance where the barrier is equal to the projectile energy. At low energies where $E \ll kT$ or, equivalently, where the classical turning point R_c is much larger than the nuclear radius R_n, the tunnelling probability can be approximated by the Gamow factor

$$P = e^{-2\pi\eta} \tag{1.19}$$

where η is called Sommerfeld parameter and is equal to

$$\eta = \frac{Z_x Z_A e^2}{\hbar v} \tag{1.20}$$

Because of the exponential behaviour of the tunnelling probability, the cross section for charged particle induced reactions drops rapidly for energies below the Coulomb barrier:

$$\sigma(E) \propto e^{-2\pi\eta} \tag{1.21}$$

As shown in the previous section (equation 1.3), another non nuclear energy dependent term involves the de Broglie wavelength:

$$\sigma(E) \propto \pi\lambda\!\!\!^{-2} \propto \frac{1}{E} \tag{1.22}$$

Using both relations, the cross section can be expressed as

$$\sigma(E) = \frac{1}{E} e^{(-2\pi\eta)} S(E) \tag{1.23}$$

where all the nuclear effects are included in S(E), referred to as the astrophysical S-factor. For nonresonant reactions, this factor is a smoothly varying function of energy and varies much less rapidly with beam energy than cross section.This is the reason why the S-factor is much more useful in extrapolating measured cross section to astrophysical energies where measurement are not possible (figure 1.3). Inserting the cross section defined in (1.23) in equation (1.16), the reaction rate can be written as

$$\langle \sigma v \rangle = \left(\frac{8}{\pi\mu}\right)^{1/2} \frac{1}{(kT)^{3/2}} \int_0^\infty S(E) \cdot e^{-\frac{E}{kT} - \frac{b}{E^{1/2}}} dE. \tag{1.24}$$

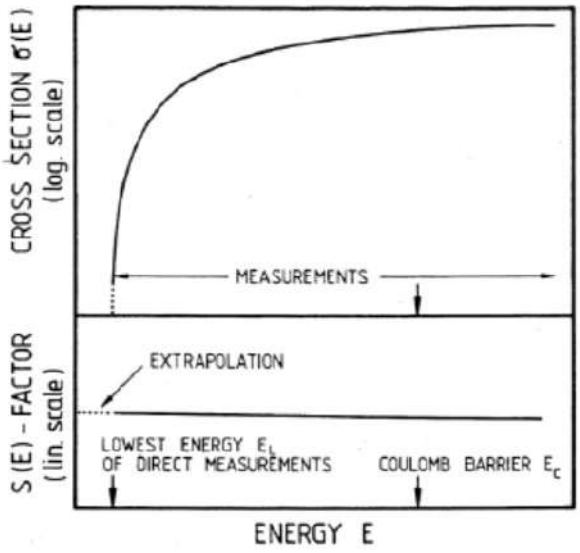

Figure 1.3: Charged-particle-induced reaction cross section. The cross section drops very quickly at low energy, making direct measurements impossible below a certain limit, depending on the expected counting rate and the background [1].

where b, which arises from the barrier penetrability, is given by

$$b = \frac{\sqrt{2\mu}e^2 Z_x Z_A \pi}{\hbar} \tag{1.25}$$

The quantity $b^2 = E_G$ is called Gamow energy.
Since for nonresonant reactions S(E) varies smoothly with energy, the energy dependence of the integrand in equation (1.24) is governed by the two exponential terms:

- the factor $e^{-(E_G/E^{1/2})}$ comes from the penetration through the Coulomb barrier and becomes very small at low energy;
- the factor $e^{-\frac{E}{kT}}$, which vanishes at high energy, is a measure of the number of particles available under the Maxwell-Boltzmann distribution.

The product of the two terms leads to a peak around the energy $E_0 = \left(\frac{\sqrt{E_G}kT}{2}\right)^{2/3}$, known as the Gamow peak (figure 1.4). For a given temperature T nuclear reactions are likely to occur in a specific energy range around

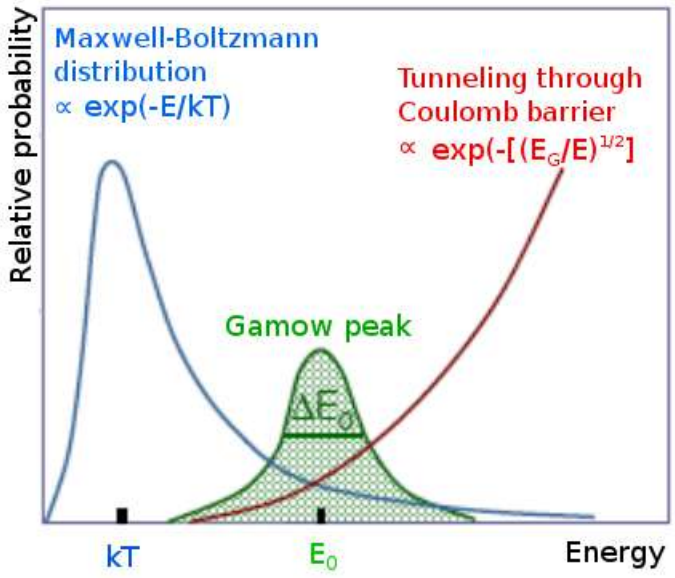

Figure 1.4: The Gamow peak as the convolution between the energy distribution function (Maxwell-Boltzmann) and the quantum mechanical tunnelling function through the Coulomb barrier.

E_0 (the Gamow window). In this particular energy range, in case of non-resonant reaction, the S-factor can be considered constant and can be carried out of the integral:

$$\langle \sigma v \rangle = \left(\frac{8}{\pi\mu}\right)^{1/2} \frac{1}{(kT)^{3/2}} S(E_0) \int_0^\infty e^{-\frac{E}{kT} - \frac{b}{E^{1/2}}} dE \tag{1.26}$$

By taking the first derivative of the integrand in the previous equation, the energy E_0 for which the integrand has the maximum value can be find. Inserting this E_0 value in equation (1.26), the maximum value of the integrand is found ($I_{max} = e^{-3E_0/(kT)}$). The exponential term in (1.26) can be fairly well approximated by a Gaussian function centered in E_0:

$$exp\left(-\frac{E}{kT} - \sqrt{\frac{E_G}{E}}\right) \sim exp\left(-\frac{3E_0}{kT}\right) exp\left[-\left(\frac{E - E_0}{\Delta/2}\right)^2\right] \tag{1.27}$$

with $\Delta = \frac{4}{\sqrt{3}}\sqrt{E_0 kT}$. Most of the nuclear reactions of astrophysical interest take place between $(E_0 - \Delta/2)$ and $(E_0 + \Delta/2)$. For this reason a precise knowledge of the cross section close to the Gamow peak is crucial.
Unfortunately Gamow window is often situated at very low energy, where

a direct measurement of the cross section could be very challenging, if not impossible. A possible workaround is to measure S(E) in a wide energy range, extending this range as low as possible and then to extrapolate S(E) down to the Gamow window. This solution is only possible for non-resonant reactions, where S(E) has a smooth trend and it could be expressed through a Taylor series. The Taylor expansion of the S-factor about zero is given by

$$S(E) = S(0) + \dot{S}(0)E + \frac{1}{2}\ddot{S}(0)E^2 + ... \tag{1.28}$$

where $\dot{S}(0)$ and $\ddot{S}(0)$ are respectively the first and second derivative of S(E) in E = 0.

A good example of nonresonant reaction relevant to astrophysical measurements is the process of direct capture, described in figure 1.5. Here the incoming projectile x with energy E, (which can be thought as a plane wave) goes directly to a standing wave, corresponding to the population of a specific nuclear orbital. The incoming particle interacts with the electromagnetic field of the nucleus and radiate a photon with energy $E_\gamma = E + Q - E_i$, where E_i is the energy of the bound state of the final nucleus. There is no intermediate state and no compound nucleus is formed. The cross section for the $\gamma - ray$ emission is described by a single matrix element [1]. Indicating the initial state with $|A + x\rangle$ and the final state with $|B\rangle$:

$$\sigma_\gamma \propto |\langle B|H_\gamma|A + x\rangle|^2 \tag{1.29}$$

where H_γ describes the photon emission. Direct processes are so called because they involved a direct transition from the initial to the final state, without passing through some intermediate state (such as a compound nucleus).

1.3 Resonant charged particle induced reactions

In contrast to the nonresonant reactions discussed above, there is another type of reaction mechanism in which an excited state E_r of the compound nucleus is first formed in the entrance channel, which subsequently decays to lower-lying states (figure 1.6). This process occurs only if the energy of the entrance channel $Q + E_R$ matches the energy E_r of the excited state in the compound nucleus:

$$E_R = E_r - Q \tag{1.30}$$

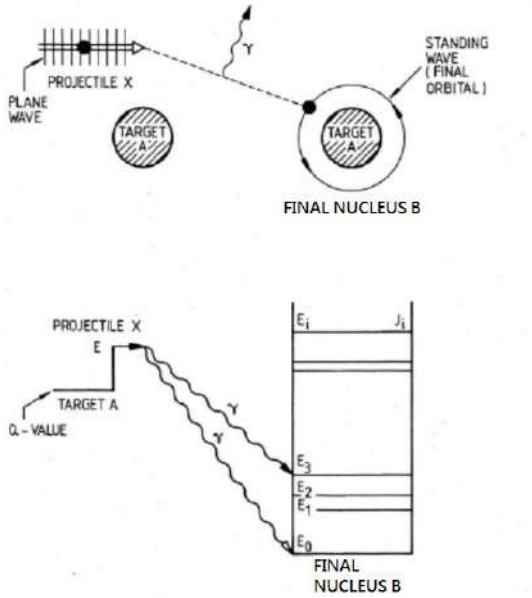

Figure 1.5: Direct capture reaction $A(x,\gamma)B$, where the entrance channel goes directly to states in the final nucleus B with the emission of a photon [1].

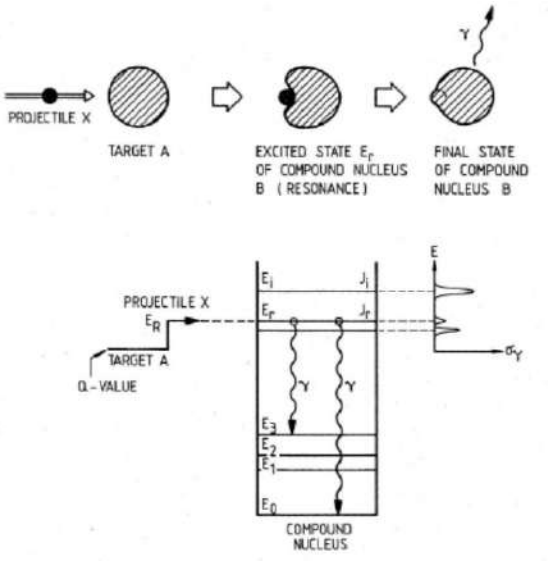

Figure 1.6: Resonant capture reaction $A(x,\gamma)B$, where the entrance channel forms an excited state E_r in the compound nucleus B [1].

In this equation the Q-value is constant and the process can occur for all the exited states E_i above the energy of the Q-value, the threshold energy, whenever the projectile energy E_R fulfills the condition of equation (1.30). If the excited state E_r decays by emission of a photon to a state E_f at lower energy, the cross section σ_γ is described by the product of two matrix elements:

$$\sigma_\gamma \propto |\langle E_f|H_\gamma|E_r\rangle|^2 |\langle E_r|H_f|A+x\rangle|^2 \tag{1.31}$$

where the matrix element involving the operator H_f describes the formation of the compound state E_r and the other matrix element the subsequent γ-decay of the state E_r. Near the resonant beam energies E_R the cross section may be extremely high. Each matrix element represents the probability for that step in the reaction to occur and is usually named partial widths Γ. The previous equation becomes thus

$$\sigma_\gamma \propto \Gamma_\gamma \Gamma_f \tag{1.32}$$

Let's consider now a *narrow* resonance that is a resonance in which the corresponding partial widths are approximately constant over the total resonance width. In this case the resonance is conventionally described by the one-level Breit-Wigner formula [3]:

$$\sigma_{BW} = \frac{\lambda^2}{4\pi}\frac{(2J+1)(1+\delta_{xA})}{(2j_A+1)(2j_x+1)}\frac{\Gamma_\gamma\Gamma_f}{(E_r-E)^2+\Gamma^2/4} \tag{1.33}$$

where j_i are the spins of target and projectile, J and E_r are the spin and the energy of the resonance, Γ_i are the resonance partial width of entrance and exit channel and Γ is the total resonance width.
The reaction rate for a single narrow resonance can be calculated inserting equation (1.33) in the definition (1.16):

$$\begin{aligned}\langle\sigma v\rangle &= \left(\frac{8}{\pi\mu}\right)^{1/2}\frac{1}{(kT)^{3/2}}\int_0^\infty \sigma_{BW}(E)Ee^{-E/kT}dE \\ &= \frac{\sqrt{2\pi}\hbar^2}{(\mu kT)^{3/2}}\omega\int_0^\infty \frac{\Gamma_\gamma\Gamma_f}{(E_r-E)^2+\Gamma^2/4}e^{-E/kT}dE\end{aligned} \tag{1.34}$$

where $\omega \equiv \frac{(2J+1)(1+\delta_{xA})}{(2j_A+1)(2j_x+1)}$. For sufficiently narrow resonances the Maxwell-Boltzmann factor $e^{-E/kT}$ and the partial widths Γ_i are approximately constant over the total width of the resonance. They can be replaced by their values at E_r and the integral can thus be calculated analytically:

$$\langle\sigma v\rangle = \left(\frac{2\pi}{\mu kT}\right)^{3/2}\hbar^2(\omega\gamma)\cdot e^{-E_r/kT} \tag{1.35}$$

where $\omega\gamma = \frac{\omega\Gamma_x\Gamma_A}{\Gamma}$. This quantity is proportional to the area under the resonance cross section, or equivalently, to the product of maximum cross section $\sigma_{BW}(E = E_r) = (\lambda_r^2/\pi)\omega\Gamma_x\Gamma_A/\gamma^2$ and the total width Γ of the resonance:

$$\Gamma \cdot \sigma_{BW}(E = E_r) = \Gamma \cdot \frac{\lambda_r^2}{\pi}\omega\frac{\Gamma_x\Gamma_A}{\Gamma^2} = \frac{\lambda_r^2}{\pi}(\omega\gamma) \tag{1.36}$$

Therefore $\omega\gamma$ is referred to as the *resonance strength*. It is clear from the above expressions that the reaction rates for narrow resonances depend only on the energy and the strength of the resonance, but not on the exact shape of the cross section curve.
When a nuclear reaction has several narrow resonances, their contributions to $\langle\sigma v\rangle$ are simply summed:

$$\langle\sigma v\rangle = \left(\frac{2\pi}{\mu kT}\right)^{3/2}\hbar^2\sum_i(\omega\gamma)_i \cdot e^{-E_r/kT} \tag{1.37}$$

A resonance whose width is not negligible with respect to the resonance energy is defined *broad* resonance. In this case, since the resonance extends over a much wider range, the energy dependence of λ, Γ_γ, Γ_f and Γ is not negligible. The cross section is given by

$$\sigma_{BW} = \frac{\lambda^2(E)}{4\pi}\omega\frac{\Gamma_\gamma(E+Q)\Gamma_f(E)}{(E-E_r)^2 + \Gamma(E)^2/4} \tag{1.38}$$

where all the energy dependencies have to be considered for numerical integration. The reaction rate per particle pair can be calculated numerically replacing the previous relation in equation (1.16):

$$\langle\sigma v\rangle = \frac{\sqrt{2\pi}\hbar^2\omega}{(\mu kT)^{3/2}}\int_0^\infty e^{-E/kT}\frac{\Gamma_\gamma(E+Q)\Gamma_f(E)}{(E-E_r)^2 + \Gamma(E)^2/4} \tag{1.39}$$

Finally, let's consider a bound state in the final nucleus with energy $E_r < Q$. There is no positive beam energy E to match the resonance condition $E = E_r - Q$. Nevertheless, if this bound state is broad enough, a significant tail extends over the Q-value and low energy projectiles can populate the high-energy tail of the bound state. This may result in increasing cross section with decreasing energy. Depending on the Gamow window this *subthreshold* resonance can play a significant role in the reaction rate.

Nuclear reactions may occur through resonant and non-resonant mechanisms. If interference effects between these two mechanisms can be neglected the cross section is the sum of the two contributions $\sigma_{tot} = \sigma_R + \sigma_{NR}$ and the reaction rate per particle pair will be $\langle\sigma v\rangle_{tot} = \langle\sigma v\rangle_R + \langle\sigma v\rangle_{NR}$.

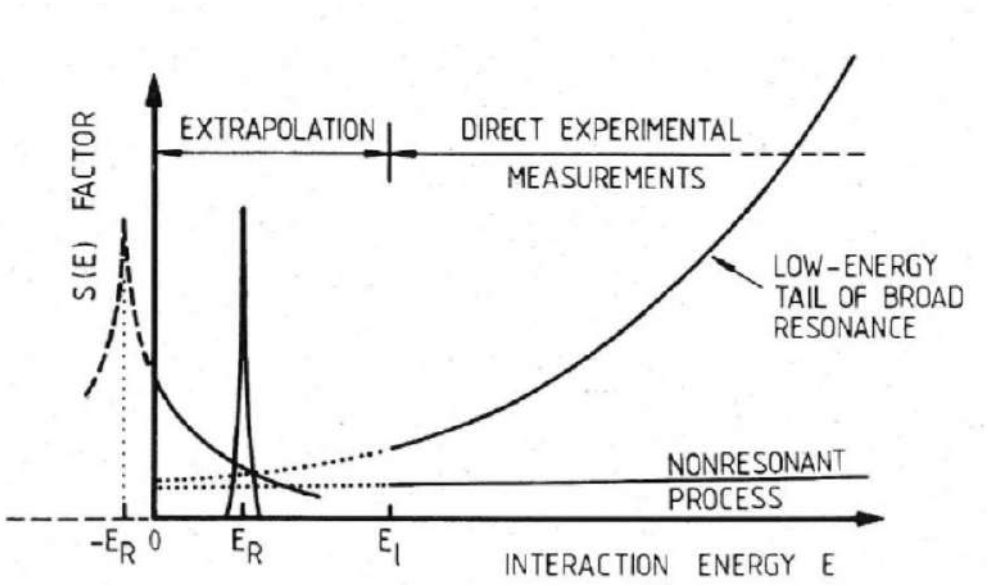

Figure 1.7: The sloped drop of the cross section owing the Coulomb barrier results in a lower energy limit E_l below which direct measurement are not possible. The extrapoation to zero of the S-factor may be not correct if sub-threshold resonances at $-E_R$ are present [1].

The cross section for charged-particle-induced reactions drops very quickly with decreasing energy because of the tunnelling probability through the Coulomb barrier. This makes measurements at low energy (inside the Gamow window) very difficult. Extrapolations are often required to retrieve the value of the cross section at energies of astrophysical interest. Similarly it is possible to extrapolate the S-factor which does not take into account the dependence of the cross section on the Coulomb repulsive potential. Since the extrapolation is only an evaluation of the cross section in an energy range which is not accessible, it is possible to obtain an incorrect extrapolation of the cross section because of resonant phenomena (figure 1.7).

1.4 Experimental measurement of nuclear astrophysical reactions

Thermonuclear reactions induced by charged particles are mainly studied by means of γ-ray or particle spectroscopy both hampered predominantly by background effects of natural radioactivity and cosmic rays in the detectors. This leads typically to a background signal rate much higher than the ex-

pected count rate at ultra-low energies. The main sources of natural γ-ray background arise from several sources: radionuclides belonging to natural radioactive series, radon, long-lived natural radionuclides such as ^{40}K, radionuclides of cosmogenic origin and radionuclides of artificial origin. All these radionuclides lead to γ-ray background with signals below $E_\gamma = 3.5$ MeV. In comparison, the γ-ray background above $E_\gamma = 2.6$ MeV is mainly dominated by the effects of cosmic rays in the detectors, i.e. muon and neutron-induced events. Conventional passive or active shielding around the detectors can only partially reduce the problem. The best solution is to install an accelerator facility in a laboratory deep underground [4].

The LUNA (Laboratory for Underground Nuclear Astrophysics) collaboration has exploited the low-background environment of the underground laboratory under the Gran Sasso Mountain in Italy (LNGS) to perform direct measurements at the relevant astrophysical energies. The rock overburden of about 1400 m (3800 m water equivalent) reduces the muon component of the cosmic background by a factor 10^6, the neutron component by a factor 10^3 and the gamma component by a factor 10, with respect to a laboratory on the Earth surface. All this leads to a reduction of the gamma background above 3 MeV in an HPGe detector placed underground at LNGS by a factor ~ 2500 with respect to the same detector placed overground. In addition, going underground enhances the effect of passive shielding particularly for lower energy gammas where the background is dominated by environmental radioactivity. Indeed, a passive shield can be built around the detector also in a laboratory at the Earth surface. However, passive shielding are of limited utility since additional background from interactions of the cosmic rays with the shielding material overwhelms the positive effect of attenuation in the shielding itself (figure 1.8).

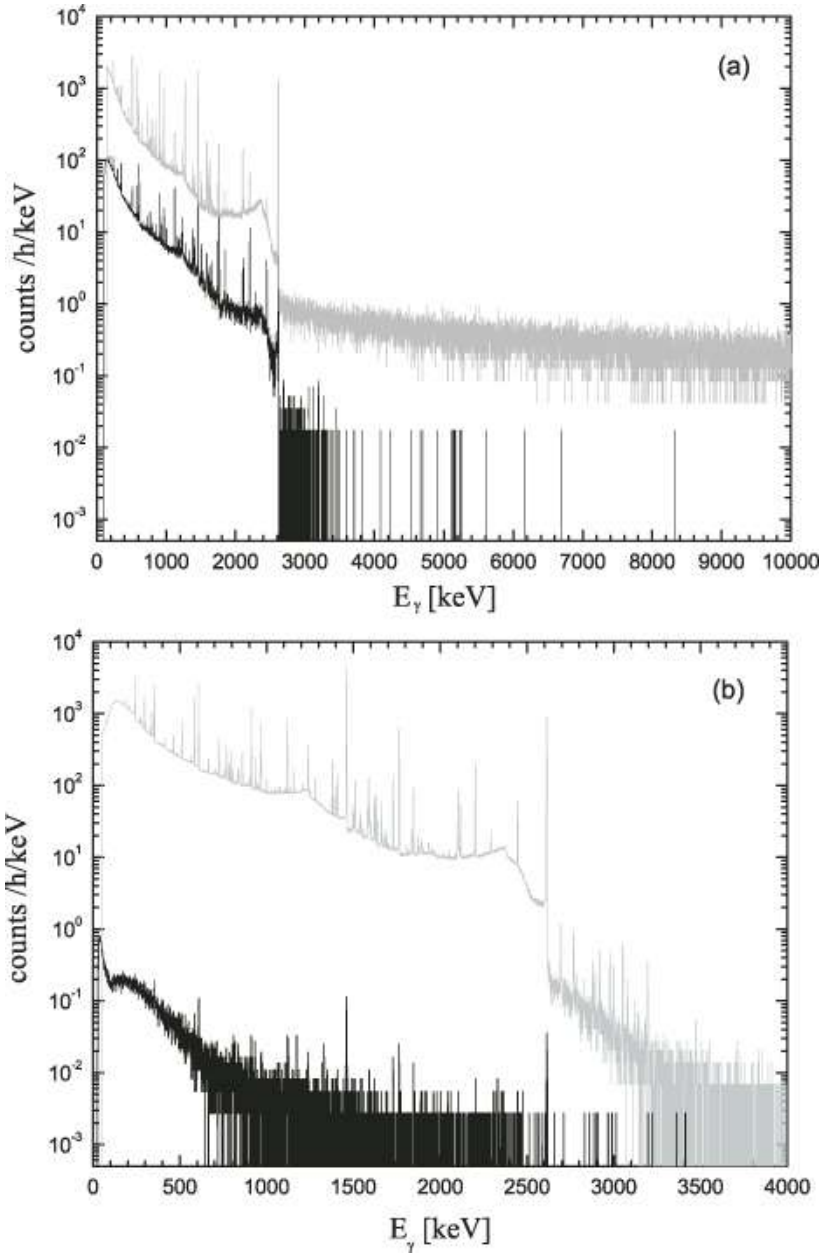

Figure 1.8: The upper panel illustrates spectra of γ-ray background as observed with a Ge detector placed outside (grey line) and inside (black line) of LNGS. The lower panel shows a comparison of low-energy spectra inside LNGS without lead shielding (grey line) and including a heavy lead shield (black line) [4].

CHAPTER 2

The $^2H(p,\gamma)^3He$ reaction in the Big Bang Nucleosynthesis energy range

This chapter is finalized to describe the cosmological context in which the ^{2}H(p, γ)^{3}He is inserted. The current status of the art of the reaction will be shown and the physical motivations for a new measurement in the Big Bang Nucleoshyntesis energy range will be also discussed.

2.1 The standard cosmology

Our current understanding of the evolution of the Universe is based upon the standard model of cosmology. It subsumes the standard model of particles physics (specifically three neutrinos families) and uses the general relativity, through which Einstein describes gravity interaction as a consequence of the space-time curvature due to the effect of mass and energy, to track the time evolution of the universal expansion rate and its matter and radiation content.
The pillars on which the cosmological standard model is based are [5]:

1. the expansion of the Universe, described by the Hubble's law;

2. the almost perfect black body spectrum of the background photon radiation, the so called Cosmic Microwave Background Radiation (CMBR);

3. the nucleosynthesis of the light elements;

4. the homogeneity and the isotropy of the Universe on large scale.

The latter, also known as the Cosmological Principle, implies that the metric itself should be homogeneous and isotropic and singles out the $Friedmann-Lema\widehat{i}tre-Robertson-Walker$ (FLRW) models. In comoving spherical coordinates one has:

$$ds^2 = g_{\mu\nu}dx^\mu dx^\nu = dt^2 - a^2(t)\left[\frac{dr^2}{1-kr^2} + r^2(d\theta^2 + sin^2\theta d\Phi^2)\right] \tag{2.1}$$

where $g_{\mu\nu}$ is the metric tensor of the four-dimensional space-time, $a(t)$ is the cosmic scale-factor and $k = 1, 0, -1$ the rescaled spatial curvature signature for an elliptic, euclidean or hyperbolic space, respectively.
The Einstein field equations relate $g_{\mu\nu}$ to the energy-momentum tensor $T_{\mu\nu}$ of the perfect fluid representing the matter-energy content of the universe:

$$R_{\mu\nu} - \frac{1}{2}Rg_{\mu\nu} - \Lambda g_{\mu\nu} = 8\pi G T_{\mu\nu} \tag{2.2}$$

where $R_{\mu\nu}$ is the Ricci tensor, R the scalar curvature, G the Newton gravitational constant and Λ is a hypothetical constant, called cosmological constant, originally introduced by Einstein to obtain a static cosmological model as solution of the equation (2.2). Substituting the FLRW metric (2.1) in the Einstein's equations (2.2), the Friedmann-Lemaitre (FL) equation for the Hubble parameter H is obtained:

$$H^2 \equiv \left(\frac{\dot{a}}{a}\right)^2 = \frac{8\pi G}{3}\cdot\rho - \frac{k}{a^2} + \frac{\Lambda}{3} \tag{2.3}$$

The equation of state of the fluid filling the universe, $P = P(\rho)$, specifying the pressure as a function of the energy density, with the covariant conservation of the energy momentum tensor

$$\frac{d(\rho a^3)}{da} = -3Pa^2, \tag{2.4}$$

allows one to get the evolution of ρ as function of a:

$$\rho_M \propto a^{-3} \tag{2.5}$$

$$\rho_R \propto a^{-4} \tag{2.6}$$

$$\rho_\Lambda \propto const \tag{2.7}$$

respectively for matter (both baryonic and dark matter,$P_B, P_{DM} \sim 0$), radiation ($P_R = \rho_R/3$), or cosmological constant ($P_\Lambda = -\rho_\Lambda$).

As usual, the present values of radiation, baryon matter, dark matter and cosmological constant energy densities will be expressed in terms of the parameters $\Omega_i = \rho_i^0/\rho_{cr}$, $i = R, B, DM, \Lambda$, with $\rho_{cr} = 3H_0^2/8\pi G$ the critical density today and $H_0 = 100h$ km $s^{-1}Mpc^{-1}$, with $h = 0.73^{+0.04}_{-0.03}$ [6]. To quantify the baryon density parameter $\omega_b \equiv \Omega_B h^2$ and the baryon to photon density ratio, $\eta = n_B/n_\gamma$ will be also used.

Matter and radiation can be described in terms of a bath of particles and quantum fields. In particular, at high temperatures rapid interactions among them ensures thermodynamical equilibrium and each particle specie is described by an equilibrium (homogeneous and isotropic) phase space distribution function

$$f_i(|\mathbf{p}|, T) = \left[exp(\frac{E_i(|\mathbf{p}|) - \mu_i}{T}) \pm 1 \right]^{-1} \tag{2.8}$$

where $E_i(|\mathbf{p}|) = \sqrt{|\mathbf{p}|^2 + m_i^2}$ is the energy, $\pm$ corresponds to the Fermi-Dirac/Bose-Einstein statistics, and μ_i the chemical potential which is zero for particles which can be emitted or absorbed in any number (like photons). In the comoving frame, the number density, energy density and pressure can be expressed as follows

$$n_i(T) = g_i \int \frac{d^3\mathbf{p}}{(2\pi)^3} f_i(|\mathbf{p}|, T) \tag{2.9}$$

$$\rho_i(T) = g_i \int \frac{d^3\mathbf{p}}{(2\pi)^3} E_i(|\mathbf{p}|) f_i(|\mathbf{p}|, T) \tag{2.10}$$

$$P_i(T) = g_i \int \frac{d^3\mathbf{p}}{(2\pi)^3} \frac{|\mathbf{p}|^2}{3E_i(|\mathbf{p}|)} f_i(|\mathbf{p}|, T) \tag{2.11}$$

where g_i is the number of internal degrees of freedom. The BBN takes place in the radiation dominated phase, hence non-relativistic particles contribute negligibly to the total energy density which, therefore, can be conveniently written in terms of the photon energy density $\rho_\gamma = \pi 2T^4/15$,

$$\rho \sim \rho_R = g * \frac{\rho_\gamma}{2} \tag{2.12}$$

which defines $g*$, the total number of relativistic degrees of freedom,

$$g* = \sum_{B_i} g_i \left(\frac{T_i}{T}\right)^4 + \frac{7}{8} \sum_{F_i} g_i \left(\frac{T_i}{T}\right)^4 \tag{2.13}$$

where the first and second terms are due to all boson and fermion species, respectively.

2.2 The nucleosynthesis and the early Universe

At the earliest time the Universe is a plasma of short-lived, exotic particles and antiparticles at very high density, temperature and pressure. The combination of high temperature and density ensures that collision rates are very high during early epochs, guaranteeing that all particles are in thermal equilibrium [7]. As the Universe expands and cools interaction rates decline and, depending on the strength of their interactions, different particles depart from equilibrium at different epochs.

Let's consider the state of the Universe at t = 0.1 seconds [8]. At that time the temperature was $T \sim 3 \cdot 10^{10} K$ and consequently the main energy per photon was about 10 MeV. This energy is much greater than the rest energy of an electron or positron, so there were positrons as well as electrons present at t = 0.1 s created by pair production.
At that time protons and neutrons are in equilibrium with each other, via interactions:

$$n + \nu_e \leftrightarrow p + e^- \tag{2.14}$$

$$n + e^+ \leftrightarrow p + \overline{\nu}_e. \tag{2.15}$$

As long as neutrons and protons are kept in equilibrium by the reactions (2.14) and (2.15), their number density is given by the Maxwell-Boltzmann equation:

$$n_n = g_n \cdot \left(\frac{m_n kT}{2\pi\hbar^2}\right)^{3/2} \cdot e^{(-\frac{m_n c^2}{kT})} \tag{2.16}$$

$$n_p = g_p \cdot \left(\frac{m_p kT}{2\pi\hbar^2}\right)^{3/2} \cdot e^{(-\frac{m_p c^2}{kT})} \tag{2.17}$$

Since the statistical weights of protons and neutrons are equal ($g_p = g_n = 2$), the neutron-to-proton ratio is:

$$\frac{n_n}{n_p} = \left(\frac{m_n}{m_p}\right)^{3/2} \cdot e^{(-\frac{(m_n - m_p)c^2}{kT})} \tag{2.18}$$

Approximating $\frac{m_n}{m_p}$ to one and calculating the difference in rest energy of the two nucleons as $(m_n - m_p)c^2 = Q_n = 1.29 MeV$, the equilibrium neutron-to-proton ratio becomes

$$\frac{n_n}{n_p} = e^{-\frac{Q_n}{kT}}. \tag{2.19}$$

At temperatures $kT >> Q_n$, corresponding to $T >> 1.5 \cdot 10^{10}$ K and $t << 1$ s, the number of neutrons is nearly equal to the number of protons. However,

as the temperature starts to drop because of the Universe expansion, protons begin to be strongly favoured and the neutron-to-proton ratio plummets exponentially.
The interactions mediating neutrons and protons in the early Universe (equations (2.14), (2.15)) involve the interaction of a baryon with a neutrino or anti-neutrino. Neutrinos interact with baryons via the weak nuclear force. Being the cross section for these weak interaction processes proportional to T^2 [9] and the number density of massless particles to T^3 [9], the interaction rate $\Gamma = n\sigma|v|$ will depends on T^5. The Hubble parameter, instead, which describes the expansion rate of the Universe, is only decreasing as T^2. When the interaction rate is greater than the expansion one, that, as shown in the following, occurs for temperatures above 1 MeV, neutrinos are in good thermal contact with the plasma. At temperature below 1 MeV the interaction rate is less than the expansion one and neutrino interactions becomes too weak to keep them in equilibrium. Thus, when $\Gamma \sim H$, the neutrinos decouple from neutrons and protons and the ratio $\frac{n_n}{n_p}$ is "frozen" at least until the neutrons start to decay at $t \sim \tau_n$. They ceased to play an active role, but continue to contribute to the Universe total density. An exact calculation of the freezing temperature requires a knowledge of the exact cross section of the proton and neutron weak interactions. Using the best available laboratory information a $T_{freeze} = 9 \cdot 10^9$ K turns out, corresponding to a time of one second. Once the temperature drops below T_{freeze}, the neutron to proton ratio is frozen at the value

$$\frac{n_n}{n_p} = e^{-\frac{Q_n}{kT_{freeze}}} \sim e^{\frac{1.29MeV}{0.8MeV}} \sim 0.2 = \frac{1}{5} \tag{2.20}$$

that means that at $t_{freeze} < t << \tau_n$, there is one neutron for every five protons in the Universe.
The scarcity of neutrons relative to protons explains why the Big Bang Nucleosynthesis (BBN) is so incomplete, leaving 3/4 of the baryons in the form of unfused protons. A neutron will fuse with a proton much more readily than a proton will fuse with another proton because, when two protons fuse to form a deuterium nucleus, a positron must be emitted to conserve charge and a ν_e must be also emitted to conserve the electron quantum number. The involvement of a neutrino in this reaction tells us that weak nuclear force is involved with its minuscule cross section. Furthermore, since protons are all positively charged, they must surmount the Coulomb barrier between them in order to fuse. By contrast the neutron-proton fusion reaction, giving rise to a deuterium nucleus plus a photon, is a strong interaction having a cross section much larger than the previous one. Finally the neutron-neutron fusion rate is negligible in the early Universe because once again the presence

of an anti-neutrino tells us this is an interaction involving the weak nuclear force and, although there is no Coulomb barrier to be surmounted, the number of neutrons is considerably lower than the protons one.
Given the alacrity of neutron-proton fusion, it is possible to state that BBN proceeds until every free neutron is bonded into an atomic nucleus, with the leftover protons remaining solitary. In this approximation the maximum possible value of Y_p, the fraction of the baryon mass in the form of ^4He, can be computed supposing that every neutron present after the freezout is incorporated into a ^4He nucleus. Considering, for example, a group of 2 neutrons and 10 protons, being $\frac{n_n}{n_p} = \frac{1}{5}$, the 2 neutrons can fuse with 2 protons to form a ^4He nucleus, while the remaining 8 protons will remain unfused. The ^4He mass fraction will then be

$$Y_{max} = \frac{4}{12} = \frac{1}{3}. \tag{2.21}$$

Adopting a more general formalism, if $f \equiv \frac{n_n}{n_p}$, with $0 \leq f \leq 1$, then the maximum possible value of Y_p is $Y_{max} = 2f/(1+f)$. In order to compute this value accurately, as well as the other isotopes abundances, it will be necessary to consider the process of nuclear fusion in more detail.

Shortly after the neutrinos decoupling the temperature drops below the mass of the electron, making the photons energy no longer enough to create further electron-positron pairs. This destroys the equilibrium between photons and pairs since, while positrons and electrons continue to combine to produce photons, they can no longer be replaced by the reverse reaction.
Until the thermal equilibrium is maintained, $T_\gamma = T_e = T_\nu$, but from this point on the temperature evolution of neutrinos and photons are decoupled and two different temperatures had to be defined. Initially neutrinos and photons temperature change at the same rate, but shortly after the neutrino decoupling, the temperature drops below the electron mass favouring the electron-positron annihilation and consequently an additional energy for photons. Assuming that this entropy transfer does not effect the neutrinos because they are already decoupled, it is easy to calculate the change in photons temperature before and after $e^\pm$ annihilation by assuming the entropy conservation. The result is the following ratio between neutrinos and radiation temperatures:

$$\frac{T_\nu}{T_\gamma} = \left(\frac{4}{11}\right)^{\frac{1}{3}} \tag{2.22}$$

The behaviour is well described in figure 2.1 where photon temperature coincides with the neutrino one until $T \sim 10^{10}$ K is reached and then, as a consequence of the electron-positron annihilation, it raises up by a 1.4 factor.

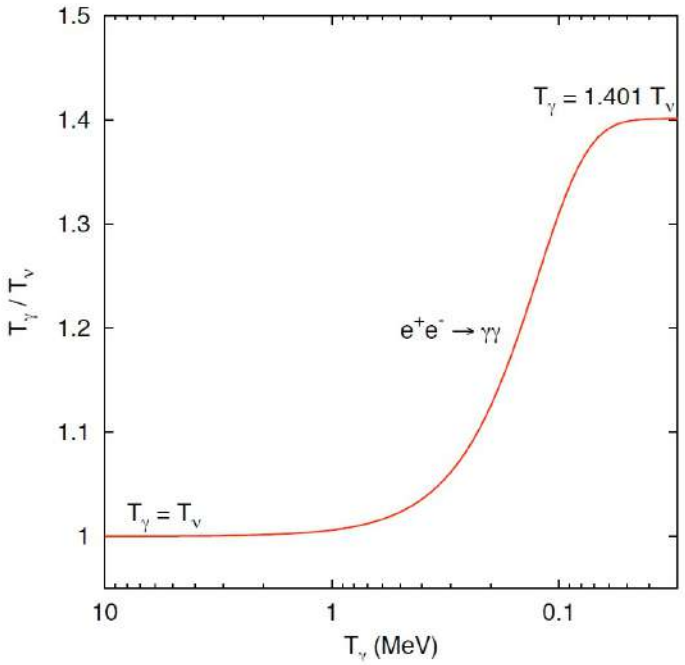

Figure 2.1: Photons and neutrinos temperatures during the $e^{\pm}$ annihilation [10].

Let's move on to the next stage of BBN: the time is $t \sim 2$ seconds and the neutrinos are decoupled from the rest of the universe, while the photons are still strongly coupled to protons and neutrons. Big Bang Nucleosynthesis takes place through a series of two-body reactions, building heavier nuclei step by step. The first step in BBN is the fusion of a proton and a neutron to form a deuterium nucleus:

$$p + n \leftrightarrow D + \gamma \tag{2.23}$$

When a proton and a neutron fuse, the energy released, carried away by a photon, is the binding energy of a deuterium nucleus:

$$B_D = (m_n + m_p - m_D)c^2 = 2.22\ MeV \tag{2.24}$$

Conversely, a photon having an energy higher than B_D can photodissociate a deuterium nucleus into its component proton and neutron. This bottleneck to BBN persists until the temperature drops even further below the deuteron binding energy, when there are too few sufficiently energetic photons to photodissociate the deuteron before it captures additional nucleons, launching BBN [11]. This transition occurs after $e^{\pm}$ annihilation, when the Universe is about 3 minutes old and the temperature has dropped below 0.1 MeV.

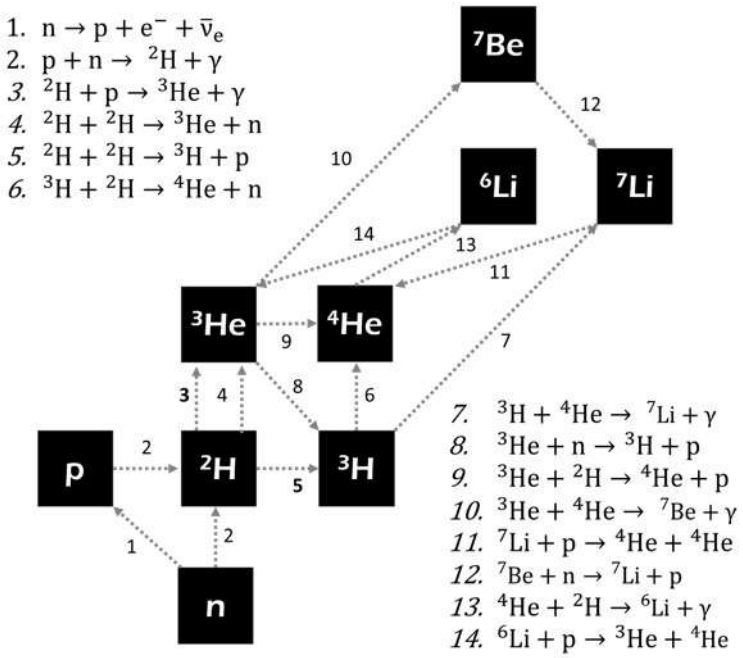

Figure 2.2: BBN reaction network.

Once a significant amount of deuterium forms, a whole nuclear process network sets in, leading to heavier nuclei production (figure 2.2). For instance, a deuterium nucleus can fuse with a proton to form ^3He or with a neutron to form ^3H, also known as tritium. Tritium is unstable, it spontaneously decays to ^3He emitting an electron and an anti-neutrino in the process. However the decay time of tritium is about 18 years; during the brief time that BBN lasts tritium can be regarded as effectively stable.
Deuterium nuclei can also fuse with each other to form a tritium nucleus with the emission of a proton or a ^3He nucleus with the emission of a neutron. A large amount of ^3He and ^3H is never present during the time of nucleosynthesis: soon after they are formed, they are converted to ^4He by reactions as

$$^3H + p \leftrightarrow^4 He + \gamma \tag{2.25}$$

$$^3He + n \leftrightarrow^4 He + \gamma \tag{2.26}$$

$$^3H + D \leftrightarrow^4 He + n \tag{2.27}$$

$$^3He + D \leftrightarrow^4 He + p \tag{2.28}$$

None of these reactions involve neutrinos, they all involve strong nuclear force, having a large cross section and fast reaction rate. Thus, once nucleosynthesis begins, D, ^3H and ^3He are efficiently converted to ^4He.

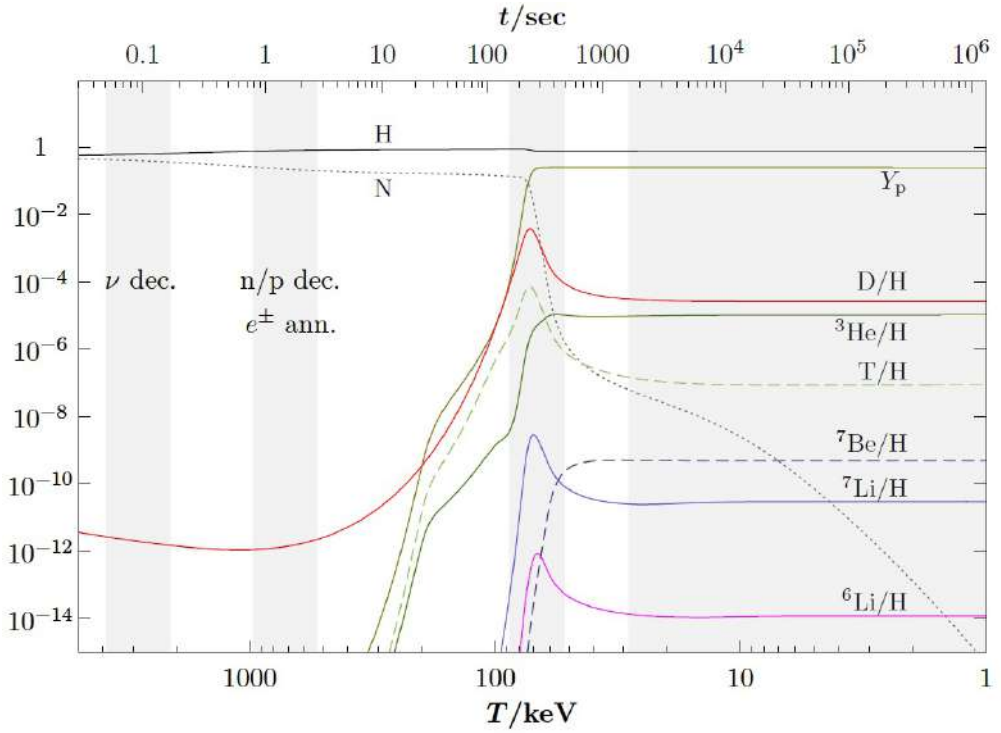

Figure 2.3: Mass fraction of nuclei as a function of time and temperature during the BBN.

Once ^4He is reached, however, the march of nucleosynthesis to heavier nuclei reaches a roadblock. For such a light nuclei, in fact, ^4He is exceptionally tightly bound; by contrast, there are no stable nuclei with $A = 5$. Fusing a proton or a neutron to ^4He does not work because ^5He and ^5Li are not stable nuclei. Only small amount of ^6Li, ^7Li, the two stable lithium isotopes, and ^7Be are made by reactions such as

$$^4He + D \leftrightarrow^6 Li + \gamma \tag{2.29}$$

$$^4He +^3 H \leftrightarrow^7 Li + \gamma \tag{2.30}$$

$$^4He +^3 He \leftrightarrow^7 Be + \gamma \tag{2.31}$$

The synthesis of nuclei with $A > 7$ is hindered by the absence of stable nuclei with $A = 8$. Figure 2.3 shows the chemical species evolution occurs during the epoch of primordial nucleosynthesis as a function of time and temperature.

2.3 Cosmological implication

The yields of D, ^3He, ^4He, ^6Li and ^7Li depend on various physical parameters. Most importantly they depend on the proton-to-photon ratio η. A higher η increases the temperature at which deuterium synthesis occurs, giving hence an earlier start to the BBN. Since BBN is a race against the clock as the density and the temperature of the Universe drop, getting an earlier start means that nucleosynthesis is more efficient in producing ^4He, leaving less D and ^3He as leftovers. A plot of the mass fraction of various elements produced by Big Bang Nucleosynthesis is shown in figure 2.4. Note that larger values of η produce larger values for Y_p and smaller values for the deuterium density, as explained above. The dependence of the ^7Li density on η is more complicated. Within the range of η plotted in figure the direct production of ^7Li by the fusion of ^4He and ^3H is a decreasing function of η, while the indirect production of ^7Li by ^7Be electron capture is an increasing function of η. The net result is a minimum in the predicted density of ^7Li at $\eta \sim 3 \cdot 10^{-10}$.

Broadly speaking, it is immediately evident that the baryon-to-photon ratio can't be as small as $\eta \sim \cdot 10^{-12}$. If it were, BBN would be extremely inefficient and we would expect only tiny amounts of helium to be produced ($Y_p < 0.01$). Conversely it is evident also that the baryon-to-photon ratio can't be as large as $\eta \sim \cdot 10^{-7}$. If it were, nucleosynthesis would have taken place very early (before neutrons had a chance to decay), the universe would be essentially deuterium-free and Y_p would be near its maximum permissible value of $Y_{max} \sim 0.33$. In determining the value of η it is most useful to determine the primordial abundance of deuterium. This is because its abundance is strongly dependent on η in the range of interest. Thus, determining the deuterium abundance with appropriate accuracy will allow η to be determined fairly well. By contrast, the primordial helium fraction, Y_p, has only a weak dependence on η for the range of interest, as shown in figure 2.4. Thus, determining η with a fair degree of accuracy would require measuring Y_p with high precision.

For a given η the light elements abundances are sensitive to the cosmic expansion rate H at that epoch, which, as demonstrated in paragraph 2.1, is given by the Friedmann equation:[1]

$$H^2 = 8\pi G\rho \sim g * T^4/m_{Pl}^2 \tag{2.32}$$

being sensitive through $g*$ to the number of relativistic degrees of freedom in equilibrium. Thus the observed primordial abundance measures the number

[1] m_{Pl} is the Plank mass defined as $[\hbar c/G]^{1/2}$

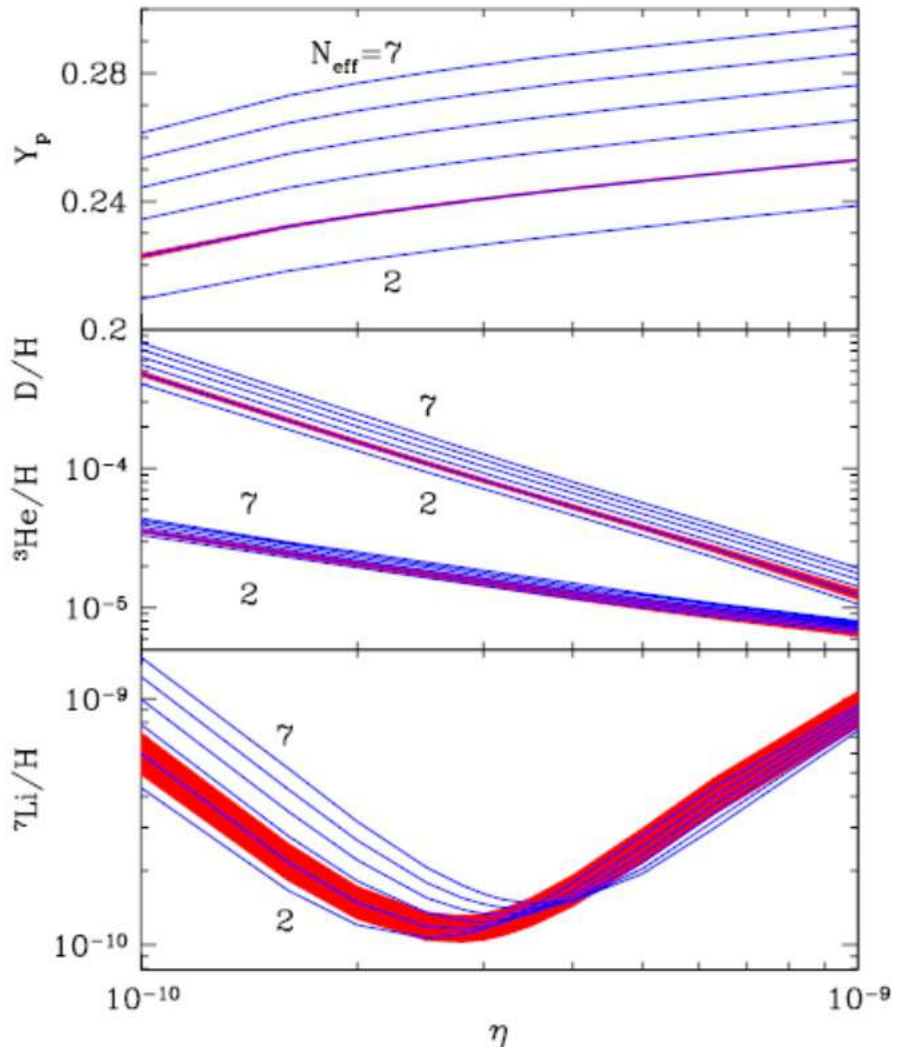

Figure 2.4: Yields of light nuclides as functions of the baryon-to-photon ratio, η. The blue lines indicate yields for a single value of N_{eff} changing from 2 to 7. The red bands indicates the nuclear uncertainty on those yields for $N_{eff} = 3$ [12].

Reaction	$\Delta_{^2H/H} \cdot 10^5$
$p(n,\gamma)^2H$	$\pm$ 0.002
$^2H(p,\gamma)^3He$	$\pm$ 0.062
$^2H(^2H,n)^3He$	$\pm$ 0.020
$^2H(^2H,p)^3H$	$\pm$ 0.013

Table 2.1: List of the leading reactions controlling the deuterium abundance after BBN. The last column shows the error on the ratio $^2H/H$ coming from experimental (or theoretical) uncertainties in the cross section of each reaction, for a fixed baryon density $\Omega_b h^2 = 0.02207$ [14].

of relativistic species at the epoch of the BBN, usually expressed in terms of the effective number of neutrino species $N_{\nu,eff}$ [13]. Adopting the standard BBN the number of massless species of neutrinos $N_{\nu,eff}$ is three. In this case BBN has only one free parameter, η. Relaxing the assumption of exactly three light neutrino species BBN becomes a two-parameter theory, with light element abundance predictions a function of η and $N_{\nu,eff}$. Figure 2.4 shows how the primordial abundances vary as a function of η for a range of $N_{\nu,eff}$ from 2 to 7.

2.4 Primordial deuterium abundance

As just shown, the theoretical value of the primordial $^2H/H$ abundance is a rapidly decreasing function of the baryon density parameter[2] $h^2\Omega_b$. Considering a slightly more general cosmological model with extra radiation, it grows as $N_{\nu,eff}$ increases. Finally, this value depends on the cross section of a few leading nuclear processes responsible for the initial deuterium production and its subsequent processing into $A = 3$ nuclei. More precisely, the calculation depends on the thermal rate of such processes, obtained by convolving their energy-dependent cross section $\sigma(E)$ with the thermal energy distribution of incoming nuclei during BBN. The four leading reactions involved in deuterium creation and destruction are listed in table 2.1. It is evident that the main source of uncertainty is presently due to the radiative capture process ^{2}H(p,γ)^{3}He converting deuterium into helium. The present

[2]With the present day temperature $T_{CMB} = 2.73$ K, it can be shown that the ratio of baryons-to-photons is $\eta = \frac{n_b}{n_\gamma} = 5.4 \cdot 10^{-10}(\frac{\Omega_b h^2}{0.02})$, where Ω_b is the ratio of the mean density of baryons to the critical density and the Hubble constant is written as $h \equiv H_0/100 kms^{-1}Mpc^{-1}$.

experimental state for the corresponding astrophysical factor $S(E)$ will be discussed in section 2.5 showing that, in the energy range relevant for BBN, the uncertainty is in the range $6 - 10\%$, which gives an error on the primordial deuterium abundance of order $\Delta_{^2H/H} \cdot 10^5$, as reported in table 2.1. This uncertainty dominates the overall error budget. Furthermore, knowing the cross sections of the processes and assuming a given cosmological scenario and standard BBN dynamics, it is possible to infer indirectly from Planck data the abundance of primordial nuclides with exquisite precision. For example, assuming the standard model of Big Bang cosmology, the Planck experiment constraint on the baryon density, $\Omega_b h^2 = 0.02207$, can be translated into a prediction for the primordial deuterium fraction using the public BBN code PArthENoPE [15]:

$$^2H/H = (2.65 \pm 0.07) \cdot 10^{-5} \tag{2.33}$$

This constraint is competitive with the most recent and precise direct observations. Recently, the authors of [16] presented a new analysis of all known deuterium absorption-line systems, including some new data from very metal-poor Lyman-alpha systems at redshift $z = 2.8528$, visible in the spectrum of the quasar $J1358 + 0349$. Their result

$$^2H/H = (2.547 \pm 0.033) \cdot 10^{-5} \tag{2.34}$$

is smaller than the (indirect, model-dependent) cosmological determination from CMB data, with a smaller uncertainty. The structure of the absorption lines and the unfortunate level of unrelated contamination limit the accuracy with which the deuterium abundance has been measured in this system.
These two deuterium abundance determinations, while broadly consistent, are off by about one standard deviations. This small tension might be the result of experimental systematics due to the poor knowledge of the reactions cross section, as stated above.

All the terms examined above are plotted in figure 2.5 together with the baryon density provided by the Plank collaboration [18], who studies the anisotropies of the CMBR. The helium abundance (Y_p) shows a huge error bar on the astronomical observation (the green band) due to the difficulties in discriminating the primordial He, much bigger than the theoretical calculations. Conversely the deuterium observations have a narrow uncertainty, but a higher error on the theoretical abundance due to the poor knowledge of the reactions cross sections.

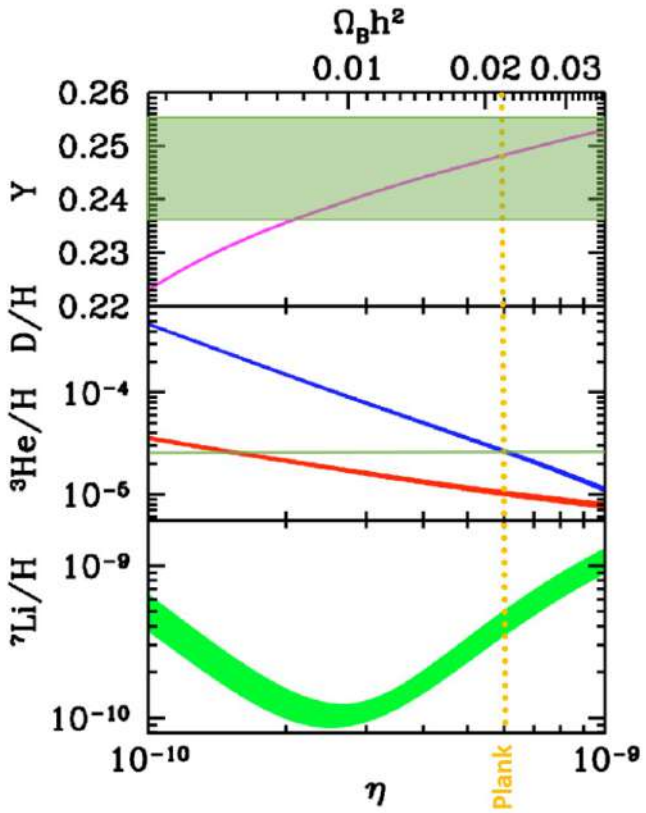

Figure 2.5: ^4He, ^2H, ^3He and ^7Li abundances plotted against the baryon-to-photon ratio. The width of each curve represents the 1s errors in the light element predictions. The vertical yellow line corresponds to Planck baryonic densities. The horizontal green areas represent the adopted observational abundances [17].

2.5 ^{2}H(p, γ)^{3}He state of the art

The ^{2}H(p, γ)^{3}He reaction has been studied in a huge energy range, using different set-ups. The results are summarized in figure 2.6, where the reaction S-factor is plotted as a function of the energy in the center of mass frame. The low energy range is dominated by the data acquired by the Luna collaboration in [19] (the red points), where the reaction has been studied within the Solar Gamow peak using a gas target and a BGO detector. In the energy range of interest for the solar processes (0 keV$< E_{cm} <$ 50 keV), the measurements of Griffiths et al. [20], Schmid et al. [21] and Bystritsky et al. [22] are also available, using proton beam on a D_2O ice solid target.

Some discrepancies exist for the lower energies data, but in [21] the authors stress on the presence of a systematic error in Griffiths's and Bailey's data due to the wrong stopping power used for the heavy-ice target, affecting the S-factor value by about 15%.
In the 200 keV$< E_{cm} <$ 1 MeV energy range, Griffiths et al. [23] and Bailey et al. [24] have measured the ^{2}H(p,γ)^{3}He cross section using once again a solid target. Warren et al. [25], instead, has measured the cross section of ^3He photodisintegration on a gas target and reaching a good agreement with direct measurement data.
Finally, in the intermediate energy range of interest for the BBN, only one data set is currently available with a systematic error of 9% [26].

One of the most important fit in literature is the one performed by Adelberger et al. in [27] using the experimental data [23], [19], [21] and [26]. The four data sets have been fitted by quadratic polynomial and plotted with the blue band in figure 2.6 that represents the 68% lower and upper bounds of the adopted best-fit.
Figure 2.6 shows also the fit performed by Angulo et al. in NACRE [28]. Because of the lack of experimental data down to very low energies in performing the fit and due to the 50% difference between [20] and [21] data sets, a unique extrapolation to zero has not been possible. Therefore the S-factor has been fitted with a polynomial of third degree, using [21] as lower limit and [20] as upper limit. An updated version of NACRE fit has been developed by [29], adding the post-NACRE data set of LUNA [19], extending thus the energy range down to 2 keV.
Finally an evaluation of the ^{2}H(p,γ)^{3}He S-factor has been performed by Descouvemont et al. in [30] (black dotted line in figure 2.6), where they extrapolate data down to very low energies without using a polynomial approximation, that could introduce significant uncertainties, but a more rigorous approach based on R-matrix technique, in which the cross section energy dependence is obtained from coulomb functions.

2.6 Theoretical nuclear physics

The astrophysical S-factor of the radiative capture ^{2}H(p,γ)^{3}He is of high interest also for theoretical nuclear physics, in particular for what concern "ab-initio" calculations, as light nuclei are involved in this process [31]. This method introduces a quasi-exact solution of the Schröndinger equation without introducing any parameter determined by experimental measurement. The aim of the "ab initio" calculations is to determine the reaction cross section that physically depends on the way the three nucleons interact with

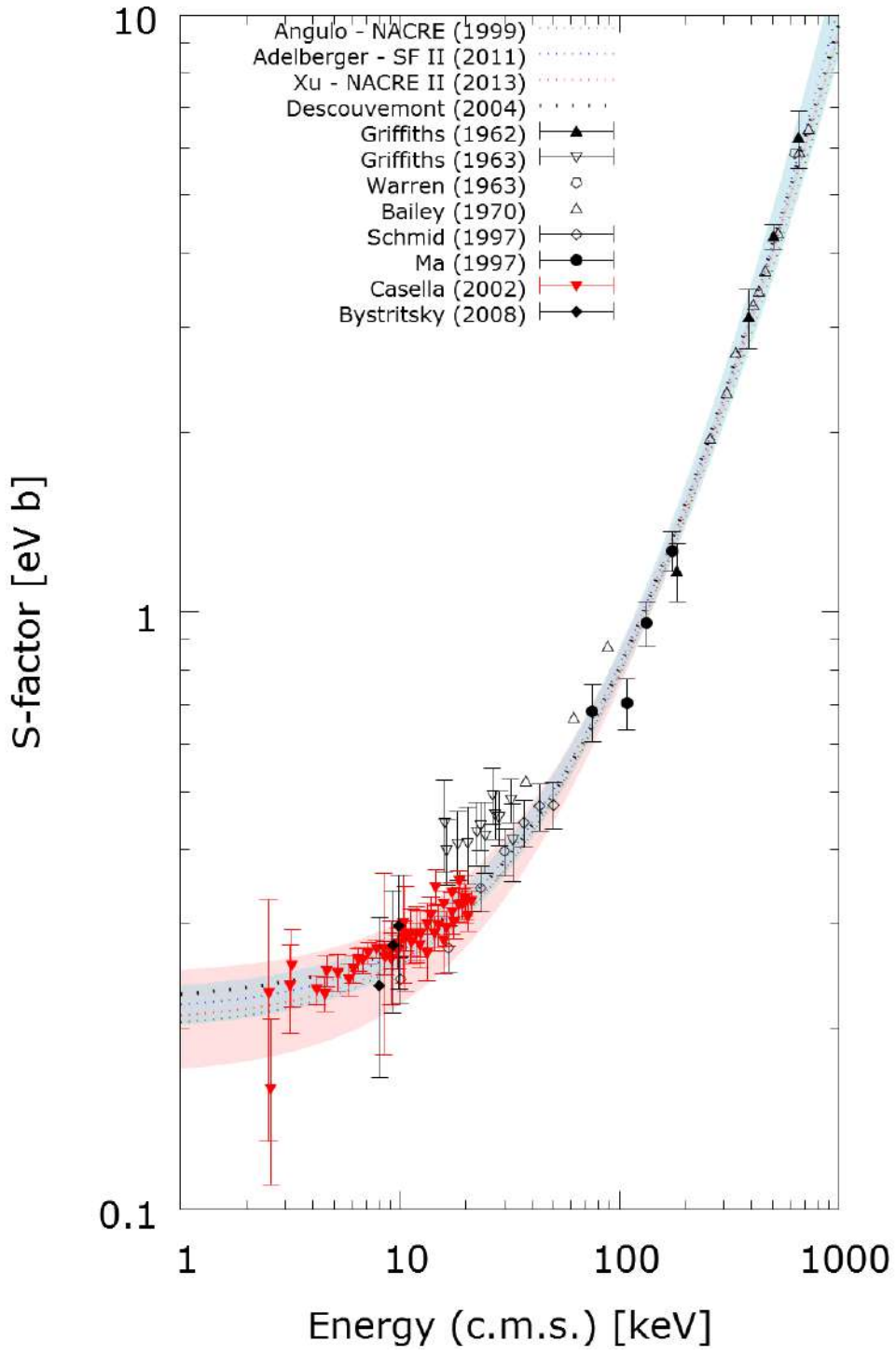

Figure 2.6: ^{2}H(p,γ)^{3}He S-factor as a function of center of mass energy. The dots are the experimental data, the colored bands the best-fit.

each other and with electroweak probes, without making any approximation out of control. To describe the *pd* continuum and ^3He bound states, the author uses variational wave functions built in a correlated-hyperspherical-harmonics (CHH) basis for a Hamiltonian consisting of the Argonne ν_{18} twonucleon ([32]) and the Urbana IX ([33]) three-nucleon potentials. This Hamiltonian is known to reproduce a variety of three-nucleon bound- and scattering-state properties, including binding energies, charge radii, elastic and inelastic cross sections and low-energy polarization observables, while the accuracy of the CHH variational method is comparable to that of other quasiexact methods. The nuclear electromagnetic current consists of one-body terms, originating from the convection and spin-magnetization currents of individual protons and neutrons, and two- and three-body exchange currents, constructed from the corresponding potentials by a procedure that preserves current conservation (CC). The method by which this is achieved has been improved over the years and its latest implementation is discussed in [31]. The theoretical astrophysical S-factor is plotted in figure 2.7 in comparison with the experimental measurements and the polynomial fit discussed in the previous section: the trend seems to be quite defined for the low and high energy limits, but in the energy range of interest for the BBN (30 keV$< E_{cm} <$ 300 keV) the situation is really unclear due to the fact that only one data set is available with a high uncertainty. A maximum discrepancy of about 30% exists between these experimental data and the theoretical prediction (black solid line)(figure 2.8).

2.7 Physical motivation for a new cross section measurement in the BBN energy range

As discussed above, a huge difference exists between theory and data making the situation really undefined and letting some author to adopt the theoretical curve and others the S-factor value obtained from direct measurements.
Since the deuterium primordial abundance depends also on the $^2\mathrm{H}(\mathrm{p},\gamma)^3\mathrm{He}$ cross section, currently known with a low accuracy, a new accurate measurement of it could reduce the error budget with which its value is presently known (equation (2.33)), trying to reach the same low uncertainty level of the direct observations.
As stated in the previous section, precise cross section measurements could have important consequences also in the cosmological field, putting some strict constrains on the cosmological parameters. Figure 2.9, in fact, shows the 1σ and 2σ confidence contour for the number of neutrinos families and

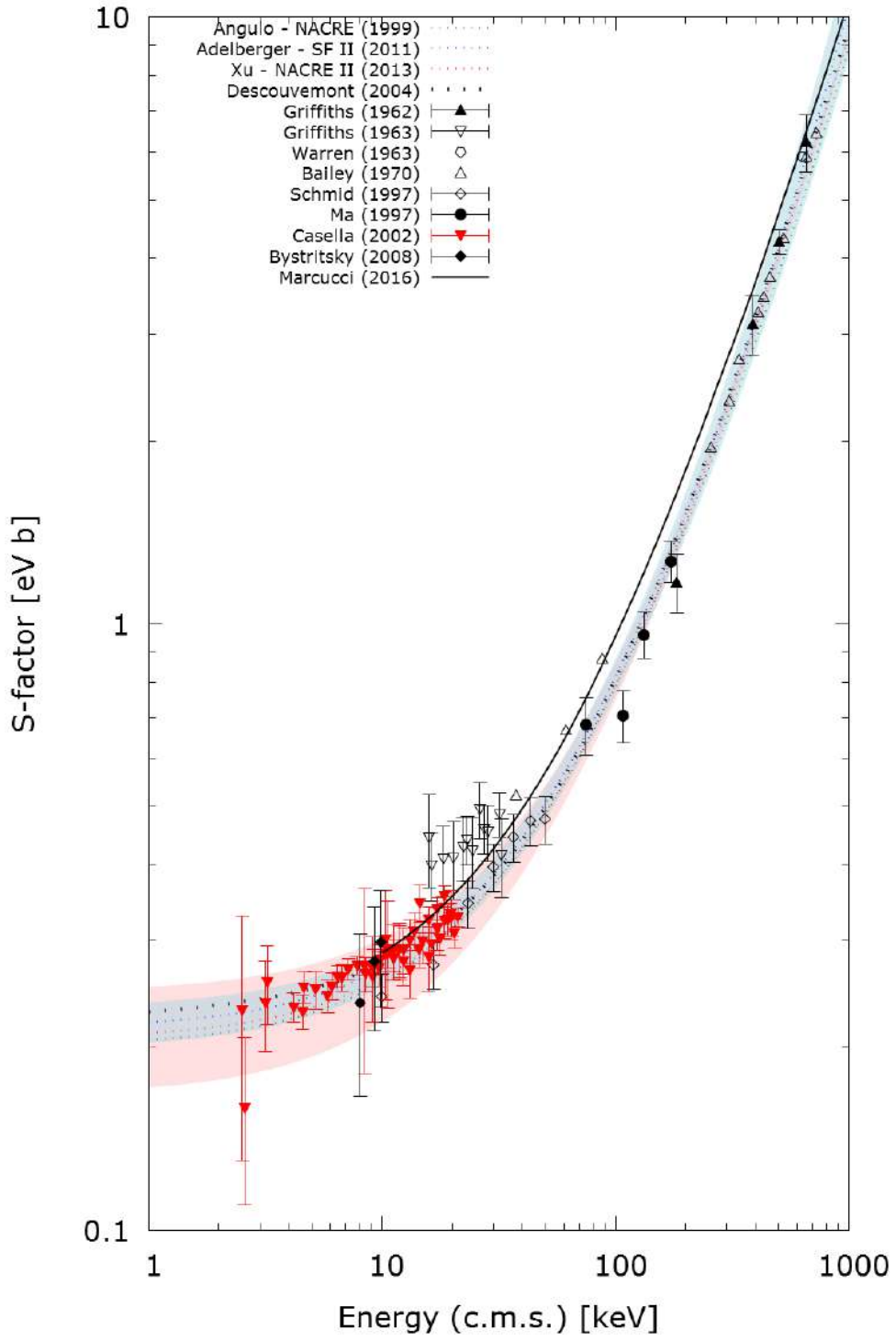

Figure 2.7: ^{2}H(p,γ)^{3}He S-factor as a function of center of mass energy, including the theoretical "ab initio" predictions.

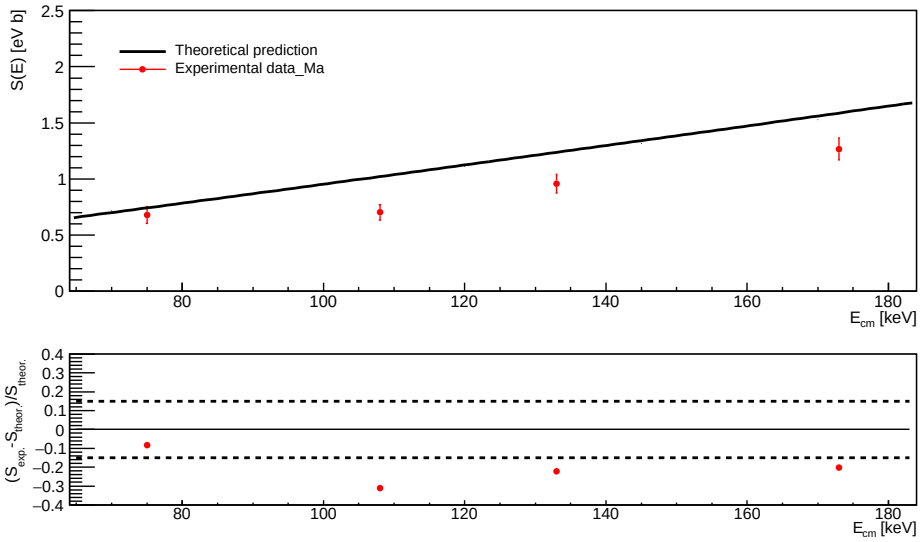

Figure 2.8: (on the top) Comparison between the theoretical prediction (black line) and the experimental data by Ma et al. (on the bottom) Residual plot to underline the percentage differences between the two trends.

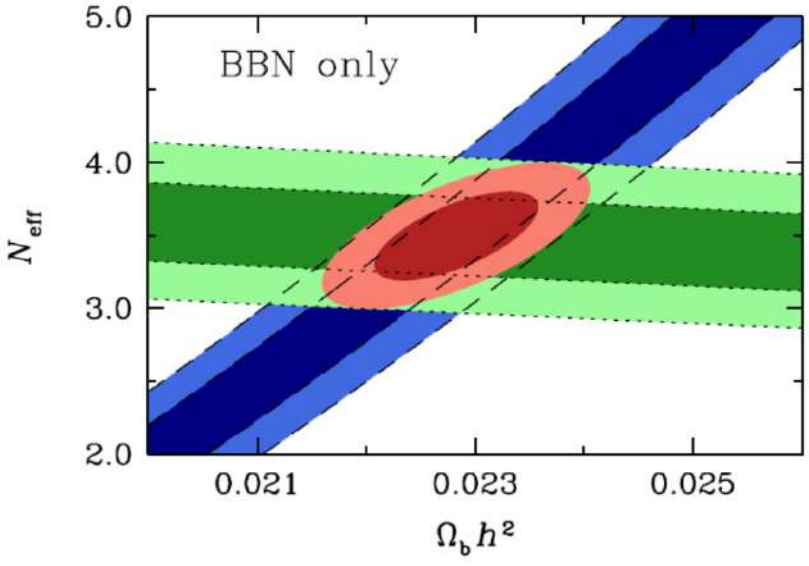

Figure 2.9: 1σ and 2σ confidence contours (dark and light shades, respectively) for N_{eff} and $\Omega_b h^2$ derived from the primordial deuterium abundance (blue), the primordial He mass fraction (green) [34].

for the baryon density, derived from the primordial deuterium abundance (blue band) and the primordial He mass fraction (green band). The width of confidence contour depends on the observational and theoretical uncertainties for each isotope. In particular, as it can be inferred by the green band width in figure 2.5, helium is dominated by the observational error, while the uncertainty for deuterium is dominated by the theoretical error and hence by the $^2\mathrm{H}(\mathrm{p},\gamma)^3\mathrm{He}$ cross section uncertainty. A high precision measurement could imply a narrow blue band and consequently stricter limits on the two cosmological parameters.

CHAPTER 3

The $^2H(p,\gamma)^3He$ reaction at LUNA: the experimental set-up

In this chapter is described the experimental approach proposed by the LUNA collaboration for measuring with high precision the ^{2}H(p, γ)^{3}He reaction cross section.
The study foresees for two main phases characterized by two different set-ups. The former set-up consists of a windowless gas target filled with deuterium gas and a 4π BGO detector. This high efficiency detector has been used for investigating the energy range between 30 keV and 260 keV in the centre of mass reference frame, extending the previous results obtained by the LUNA collaboration, where the ^{2}H(p, γ)^{3}He cross section was studied in the Solar Gamow peak (2.5 keV $< E_{cm} <$22 keV) [19]. The latter phase, instead, covers the medium-high energies (70 keV $< E_{cm} <$ 260 keV) using a High Purity Germanium detector (HPGe), whose high resolution allows the evaluation of the total reaction cross section and also of the emitted photons angular distribution.

3.1 The LUNA facility

The LUNA experiment exploits the low background environment of the underground INFN laboratory under the Gran Sasso Mountain (LNGS) to perform direct cross section measurements at relevant astrophysical energies. Two different accelerators have been used at LUNA: a compact 50 kV "home-made" accelerator and a commercial 400 kV one. The first machine

was operating between 1992 and 2001, while the second one started to operate in the year 2000 and still operating.
The LUNA accelerator is connected by a dipole switching magnet to two channels (figure 3.1): one dedicated for experiments using solid target and the other hosts a windowless gas target [35].
A solid target is spatially well defined, allowing the cross section angular dependency to be measured being the beam-hit position on the target precisely determined. However this kind of target is subject to rapid deterioration during the beam exposure, making mandatory its periodical replacement. They are commonly realized by evaporation or implantation and, in both cases, an accurate density profile has to be determined. Since it changes in time during the beam exposure, the measurements performed by a solid target are usually normalized to well known resonance yields, introducing thus a systematic error due to the normalization procedure. On the other hand the gas target is more stable to beam bombardment and may reach extreme purity, essential to minimize the beam-induced background.

3.1.1 The LUNA II 400 kV accelerator

Luna II is a 400 kV single ended electrostatic accelerator installed in the underground LNGS by the High Voltage Engineering Europe [36]. It is embedded in a 2 m^3 steel tank filled with a gas mixture of $N_2(75\%)$ and $CO_2(25\%)$, at 20 bar total pressure to prevent sparks at high electrical field intensities.
A radio frequency ion source mounted directly on the accelerator tube produces ion beams up to 1 mA intensity for hydrogen at 75% purity and up to 0.5 mA for helium. The ions can be sent into the two different parallel beam lines (figure 3.1).
The High Voltage (HV) is provided by an Inline-Cockcroft-Walton power supply, stabilized by a RC-filter at the HV power supply output and by an active feedback loop based on a chain of resistors.
A highly stable analysing magnet, bending the beam to 45°, and a vertical steering magnet guide the beam to the gas target. Before reaching the interaction chamber, the beam passes through a Farady cup, used for monitoring the proton beam current, a gate valve, insulating the accelerator in case of pressures exceeding 10^{-4} mbar and three water-cooled apertures of decreasing diameter for optimizing the beam focusing on the gas target line.

The machine has been calibrated [36] using the radiative capture reaction $^{12}\mathrm{C(p,}\gamma)^{13}\mathrm{N}$, which is non-resonant all over the energy range accessible to the accelerator. Some well known resonances of (p,γ) capture from ^{23}Na, ^{25}Mg and ^{26}Mg isotopes were used to measure the energy spread and long term stability. As a result, the beam energy spread at the exit of the accelerator

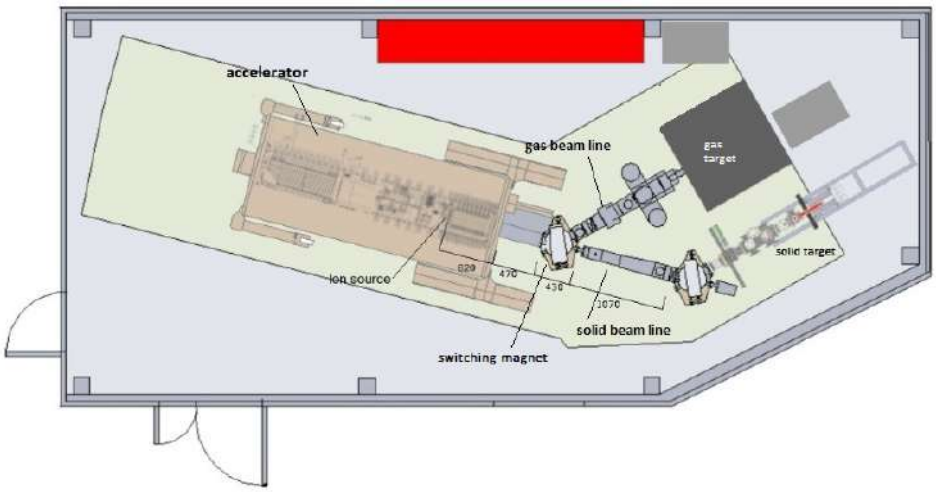

Figure 3.1: Drawing of the accelerator and the two beam lines [37].

was determined to be $< 100\ eV$ while the energy drift is $< 5\ eV/h$. These measurements led to the following calibration:

$$E_{beam} = (HV + PV) \cdot (0.9933 \pm 0.0002)\frac{keV}{kV} - (0.41 \pm 0.05)\ keV \qquad (3.1)$$

where E_{beam} is the calibrated beam energy, HV is the accelerating voltage applied to the high voltage terminal and PV is the bias voltage applied to the anode of the source. The uncertainty on E_{beam}, equal to 0.3 keV, is mainly due to the uncertainty on the $^{12}C(p,\gamma)^{13}N$ reaction Q-value. The calibration has been checked again in 2014 using the $^{20,21}Ne(p,\gamma)^{21,22}Na$ resonances.

3.1.2 The gas target

One of the two beam lines is dedicated to an extended windowless gas target [38] preventing, thus, the beam energy loss before entering the interaction chamber and limiting the beam energy straggling. To confine the gas inside the interaction chamber, a strong pressure gradient between the target and the beam line is produced by three pumping stages separated by three water cooled apertures of decreasing diameter (figure 3.2). These apertures operate not only to collimate the beam, but also to increase the impedance for the gas flow from the target to the pumping stages.
The gas enters into the chamber through the valve VT and flows through the aperture AP_1 (length L = 40 mm and inner diameter d = 7 mm) towards the first pumping stage equipped with a root pump (pumping velocity 2050 m^3/h) which pumps away the 99.5% of the gas. The remaining gas may

pass aperture AP_2 (L = 80 mm and d = 15 mm) entering thus the second pumping stage, equipped with two 1000 l/s and one 1500 l/s turbo-molecular pumps. The small still remaining quantity of gas may pass aperture AP_3 (L = 25 mm and d = 25 mm) entering the third pumping stage evacuated by a 360 l/s turbo-molecular pump. A further root pump (505 m^3/h) collects the gas coming from the previous pumps and is itself connected to a ecodry (48 m^3/h) pump. For deuterium gas at 0.3 mbar of pressure in the target chamber, for example, typical working pressure values are 10^{-3}, 10^{-6} and 10^{-6} mbar respectively in the first, second and third stage.

A MKS Baratron type 626 pressure gauge, together with its controller and the MKS 248A valve, provides the feedback which keeps stable the pressure inside the interaction chamber.
A LabVIEW software and a NI FieldPoint based system are used for the slow control of the gas target. The pressures inside the pumping stages are monitored and logged. The software allows to open and close the remotely controlled valves inside the accelerator room and to monitor the status of the pumps.

3.2 The beam calorimeter

When protons pass through a gas target are partially neutralized by the gas itself and additionally several secondary electrons can be generated. The electrical current reading using the classical Faraday cup method is thus not precise. Therefore the current can be determinated using a beam calorimeter with a constant temperature gradient between a hot and a cold side [38]. A chiller keeps the cold side at the constant temperature $T_{cold} = -20^oC$, while eight heating resistors provide a power W_0 to keep the hot side at the constant temperature $T_{hot} = 70^oC$, so that, in stationary conditions, a constant power is delivered by the resistors to maintain the temperature gradient. Four Pt100 probes in a 3-wire configuration are used for measuring the temperature in four different positions: three are located in the hot side, one close to the heating resistors, one in the middle between the beam spot and the resistors and one in a lateral position, while the fourth one is placed on the cold side (figure 3.3) [37]. When the ion beam hits the hot side, it contributes to its heating and reduces correspondingly the electric power needed to keep the temperature gradient constant. Being W_0 the power delivered by the resistors in beam off condition and W_{beam} the power when the beam is on, the current impinging on the target can be calculated as follow:

$$I = \frac{W_0 - W_{beam}}{E_{cal}/e}. \tag{3.2}$$

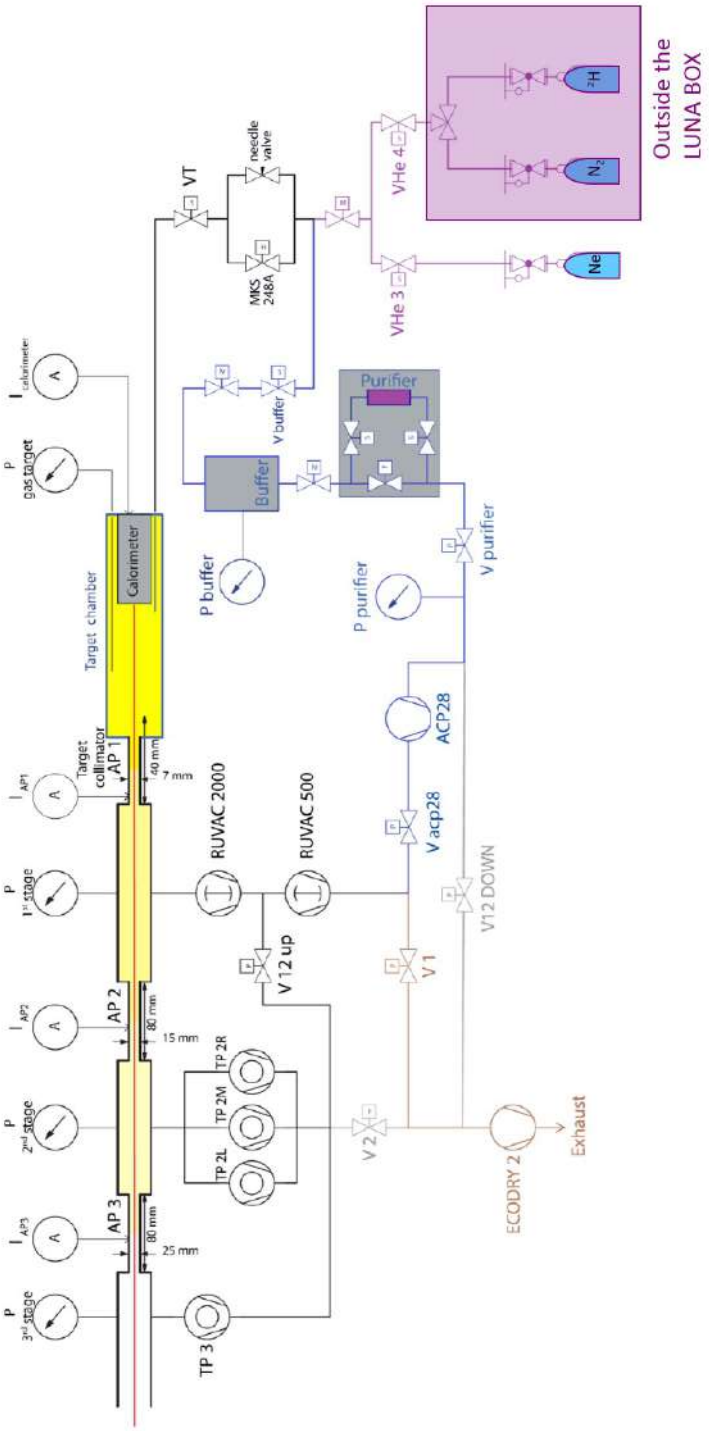

Figure 3.2: Scheme of the LUNA windowless gas target.

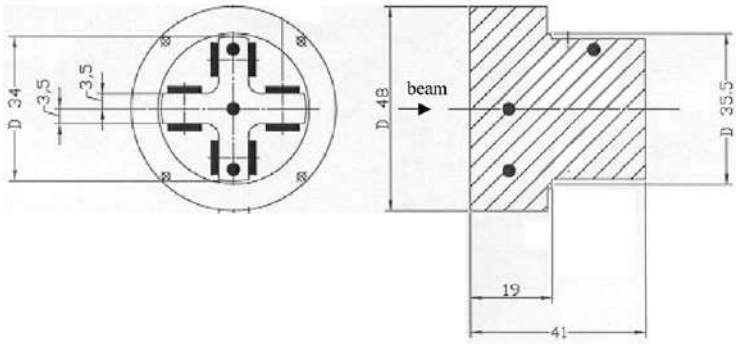

Figure 3.3: Downstream view (left panel) and section (rigth panel) of the calorimeter beam stop. The black rectangles represent the positions of the resistors, while the black circles the PT100s locations [38].

E_{cal} is the energy of the ion beam when it heats the calorimeter and it is obtained from the initial beam energy minus the energy lost by the beam in the target gas:

$$E_{cal} = E_{beam} - \Delta E_p^{target} = E_{beam} - \int_0^L \frac{dE}{d(\rho z)} \rho(z)\, dz \tag{3.3}$$

where L and $\rho(z)$ are respectively the target length and density as function of the beam path. The energy loss $\frac{dE}{d(\rho z)}$ is obtained by the well-known stopping power compilation by Ziegler (SRIM) [39] and $\rho(z)$ is deduced by the target density profile studied in the next section (section 4.1.1).

The calorimeter has been calibrated evacuating the target chamber and using the calorimeter as a Faraday cup. In running conditions the calorimeter and the target chamber are electrically insulated from the upstream part by a 10 mm thick Teflon disk; furthermore a mylar foil is inserted between the chamber and the detector. During the calibration the calorimeter and the target chamber are connected together to form the Faraday cup. Thanks to an additional pump connected directly to the chamber, a 10^{-4} mbar vacuum has been reached inside the target, reducing thus the ionization current due to the residual gas. Furthermore a metallic ring holding the AP_1 collimator has been biased to -300 V to prevent the losses of secondary electrons to the first pumping stage. Several runs have been performed varying the proton energy from 120 keV to 380 keV using a high precision current integrator and a counter unit collecting the total charge reaching the calorimeter and the chamber.

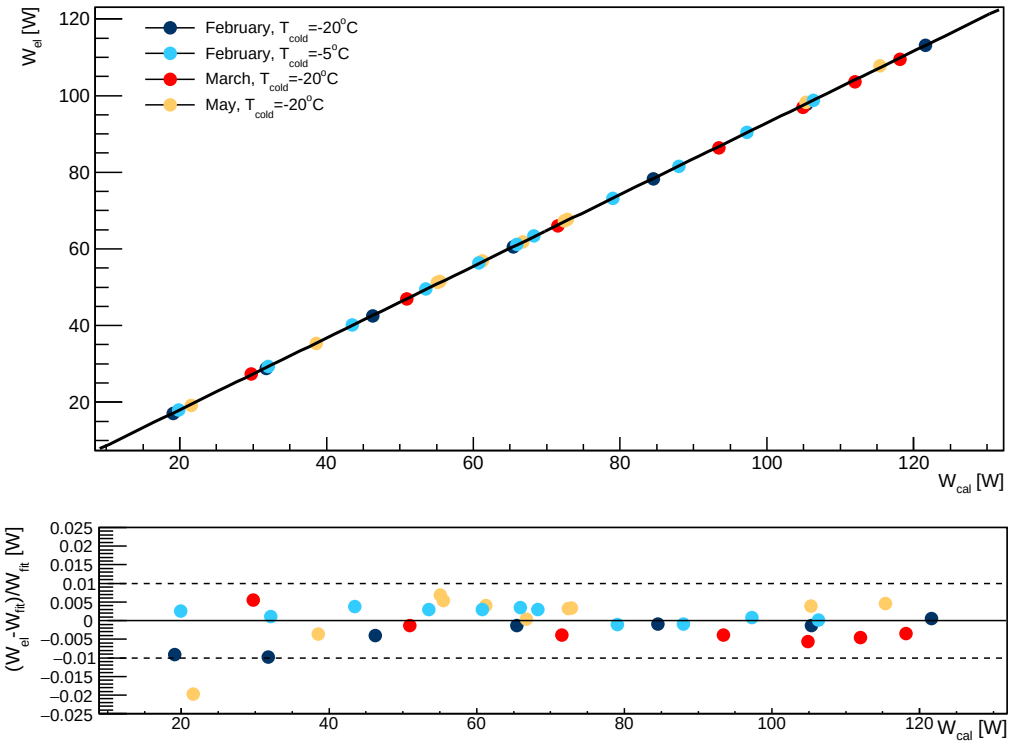

Figure 3.4: Calorimeter calibration function (top) and relative residuals (bottom). The error bars are smaller than the point dimension.

The electrical power W_{el} has been calculated for each run as:

$$W_{el} = \frac{E_{beam} \cdot I_{target}}{q_e} \tag{3.4}$$

where I_{target} has been measured with the current integrator and the counter unit. The calorimetric power W_{cal}, instead, has been calculated as the difference between the average value of the zero power W_0 and the beam power W_{beam} during the run.
Four calibration campaigns have been performed in different periods of the year and the results obtained, summarized in figure 3.4, show the trend of W_{el} as a function of W_{cal}:

$$W_{el} = (0.93 \pm 0.0018) \cdot W_{cal} - (0.7 \pm 0.1) \tag{3.5}$$

All data lie on the same line, proving that the calibration remains constant in time and the residual plot shows that, for almost all data points, the deviation

from the fitting line is less than 1%. In the plot the uncertainty associated to the calorimetric power is the standard deviation of the W_0 values, acquired during all the measurement campaign (about 0.3 W), because it is mainly due to the fact that the zero and the beam power are not acquired simultaneously so that while W_{beam} is measured, W_0 is assumed to remain constant. The uncertainty on the electric power, instead, has been calculated propagating the error on the proton beam energy (0.3 keV) and the 0.2% due to the accuracy of the current integrator and the counter unit.

3.3 The BGO set-up

The γ-rays emitted by the ^{2}H(p,γ)^{3}He reaction have been detected by an optically segmented Bismuth Germanate Oxide (BGO) detector [38] placed on the gas target beamline, housed on a frame which can be moved along the beam direction. With this set-up, the counting rate (full detection γ-peak) obtained is of the order of $10^4 - 10^5 events/hour$ in the considered energy range, making the measurement with the BGO detector relatively fast for reaching 10000 events under the photopeak to ensure a low systematic uncertainty ($< 1\%$). On the other hand the large angular coverage of BGO makes the counting yield independent of the angular distribution of the emitted photons.
Data acquisition has been performed using a digital acquisition chain saving data on a server for the subsequent analysis.

3.3.1 The target chamber

The target chamber has been designed to fit inside the central hole of the BGO crystal, described in section 3.3.2, allowing the interaction region to be entirely contained inside the 28 cm long cylindrical detector where the efficiency is maximum and almost constant.
The target chamber (figure 3.5) mainly consists of

- a tube, connecting the first pumping stage to the chamber, sufficiently long to place the chamber on the beam focus;
- a copper collimator (AP_1), determining the strong pressure gradient between the target region and the pumping stages, continuously water cooled to prevent overheating;
- the interaction chamber consisting of a stainless steel tube having a inner diameter of 56 mm and a length of 108 mm from the collimator to the beam stop surface.

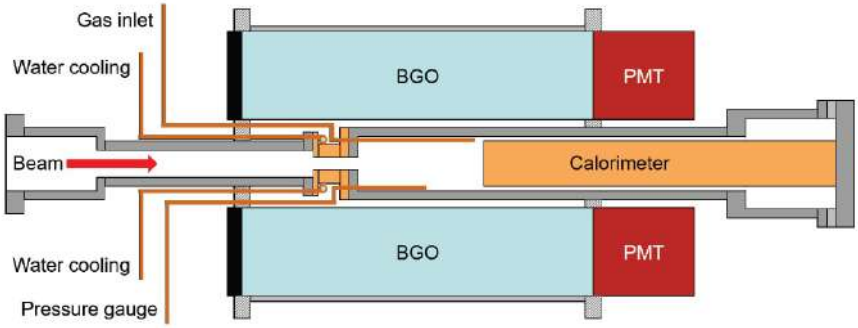

Figure 3.5: Drawing of the target chamber inside the BGO detector in their final configuration.

3.3.2 The BGO detector

The BGO is an inorganic scintillator whose main characteristics, the large mass density (7.13 g/cm^3) and the high atomic number of Bi, make it the scintillator with the highest probability of photoelectric absorption per unit volume.
The crystal is a cylinder 28 cm long, with a coaxial hole of 6 cm of diameter and a radial thickness of 7 cm. It is optically divided in six sectors, each covering a 60^o azimuthal angle, granting a 4π configuration geometry (figure 3.6). The detector crystals are optically isolated and read out separately by photomultiplier tubes located at one end of the bar, with the other end covered by plastic light reflectors.
The light yield of the BGO strongly depends on temperature: at around 20^oC of temperature the yield decreases by 1% every 1^oC temperature increase [40]. This makes the energy calibration of the detector change from time to time requiring a new calibration for each acquired spectrum.

3.3.3 Electronics and DAQ

The configuration of the electronics used for the acquisition is shown in figure 3.7. The six PMTs (Hamamatsu R1847-07) for the detector segments has been fed by a programmable VME high voltage supply (CAEN V6533P) having six independent channels, so that the voltage for each PMT could be set individually to match the gain. The anode output of each PMT has been connected to a ORTEC 113 preamplifier together with a pulser signal sent to the test input to check the stability of the electronics and to evaluate the dead time of the acquisition. The preamplifier output of each segment is then acquired by a CAEN V1724 digitizer (8 channels, 14 bit,

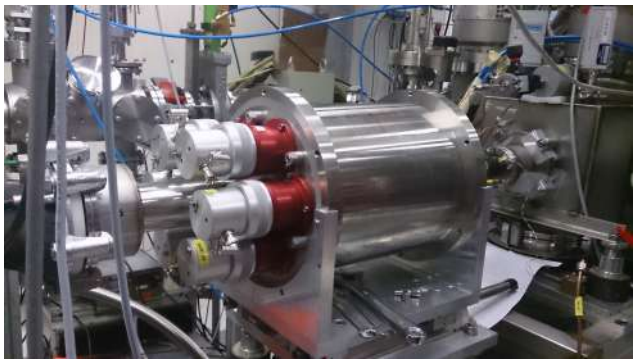

Figure 3.6: The six crystals BGO detector.

100 MS/s), connected to the PC through a CAEN VME-USB bridge. Each channel has been set to trigger independently and has independent threshold adjustable according to the electronic noise. The software $MC^2Analyzer$ by CAEN has been used for the acquisition of list mode data, acquiring and saving information event by event. Each saved event consisted of a trigger timestamp, energy and some additional information to indicate special events and conditions. A software program has been written to process the data after the acquisition, converting the acquired binary files into ROOT files and building the spectra for each segment, using a proper energy calibration. The spectra have been calibrated using two low energy peaks owing to the natural background: one at 1460 keV due to the ^{40}K and the other at 2614 keV due to the ^{208}Tl. These peaks are visible and clearly distinguishable in all the ^{2}H(p,γ)^{3}He runs as well as in the background ones. The linearity of the calibration (figure 3.8) has been verified up to higher energies using the peaks originated by ^{14}N(p,γ)^{15}O resonant reaction and the γ-rays emitted by the radioactive capture on deuterium.

3.4 The HPGe set-up

An exhaustive study of the ^{2}H(p,γ)^{3}He reaction includes the study of the angular distribution of the emitted $\gamma-$rays for calculating not only the total but also the differential cross section. As shown in detail below, this study can be accomplished using a HPGe detector facing the gas target in a close geometry, thanks to its good energy resolution (about 5 keV at $E_\gamma = 6$ MeV) that allows to precisely measure the emitted photon energy. On the other hand, because of the the low germanium efficiency (about 0.3%), the counting rate obtained with this set-up is about 2 order of magnitude less than the BGO phase requiring thus longer acquisition time: it varies from

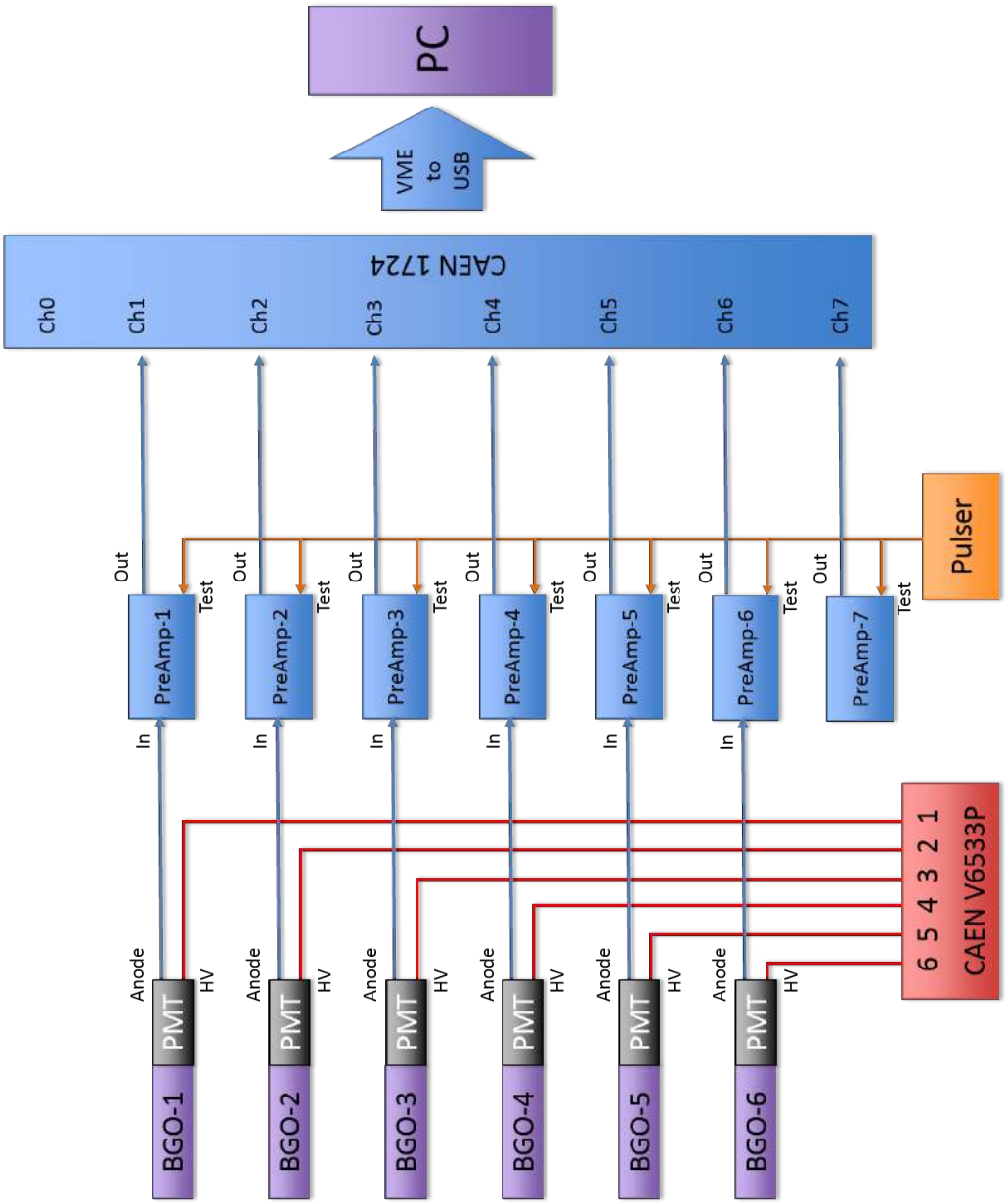

Figure 3.7: Scheme of the BGO electronics chain.

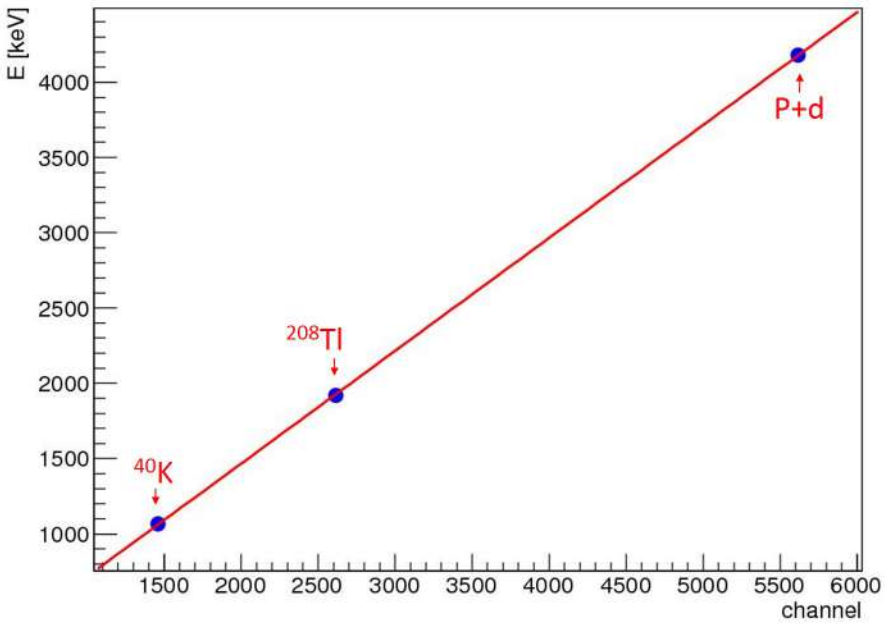

Figure 3.8: Linear BGO calibration.

$10^2 events/hour$, at the lowest measured energies, to $10^4 events/hour$, at the highest ones.
Data acquisition has been performed using two different digital acquisition chains, saving data on a server for subsequent analysis.

3.4.1 The target chamber

The angular distribution of the emitted $\gamma-$rays can be inferred exploiting the high energy resolution of a HPGe detector and the Doppler effect affecting the photons emitted along the beam line. Using an extended deuterium gas target, in fact, the emitted photons are Doppler broadened. The peak width, varying from 38 to 112 keV, will be dominated by kinematics and the angular distribution of the emitted gammas will determine the peak shape. Therefore, starting from the $\gamma-$ray energy spectrum, it is possible to extract the differential cross section of the process.
The target chamber has been designed to satisfy this request: a total length of 33 cm, in fact, allows the HPGe detector placed at the center to detect photons produced in the $20° \lesssim \theta_{lab} \lesssim 160°$ angular range. The good energy resolution of the detector allows to precisely measure the photon energy, that

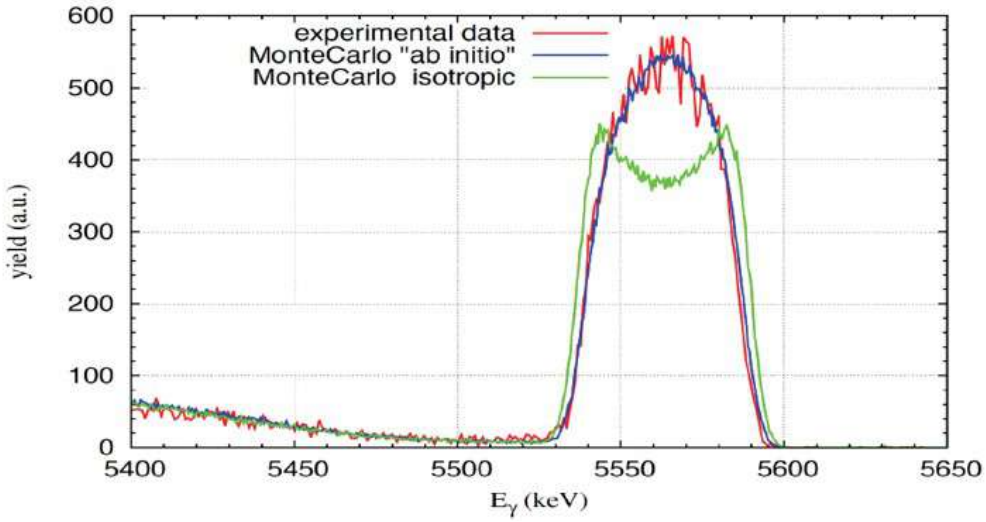

Figure 3.9: Simulated spectra of the ^{2}H(p, γ)^{3}He reaction, assuming isotropic (green) and ab-initio (blue) angular distributions at E_{cm} = 112.5 keV. The experimental data (red) are also shown. Data have been normalized to remark the close agreement with the ab-initio angular distribution.

mainly depends on the proton beam energy E_{beam} and on the angle of emitted photons with respect to the beam axis θ_{lab}:

$$E_\gamma = \frac{m_p^2 + m_d^2 - m_{He}^2 + 2(E_{beam} + m_p)m_d}{2(E_{beam} + m_p + m_d - p_p cos\theta_{lab})} \tag{3.6}$$

In the previous equation, assuming $c = \hbar = 1$, E_γ is the photon energy, m_p, m_d and m_{He} are the masses of the nuclides involved in the reaction and $p_p = \sqrt{E_{beam}(E_{beam} + 2m_p)}$ is the proton momentum. It follows that, for a given beam energy, the photon energy is uniquely determined by $cos\theta_{lab}$ due to the Doppler effect. Figure 3.9 shows the result of a preliminary measurement performed with the HPGe detector, where the energy distribution of the emitted photons is well in agreement with ab-initio calculations [31].

The interaction chamber, as shown in figure 3.10, consists of a stainless steel tube having a total length of 330 mm and a inner diameter of 56 mm. It is equipped with 8 apertures having a radius of 6 mm: one is used for the gas inlet, another for connecting a MKS Baratron gauge for measuring the reference pressure; the remaining apertures has been used for monitoring during the measurements the pressure and the temperature along the target. A big advantage in using this chamber is that no dedicated set-up is needed to measure the temperature and pressure profiles, exploiting the existing apertures for introducing the measurements gauges.

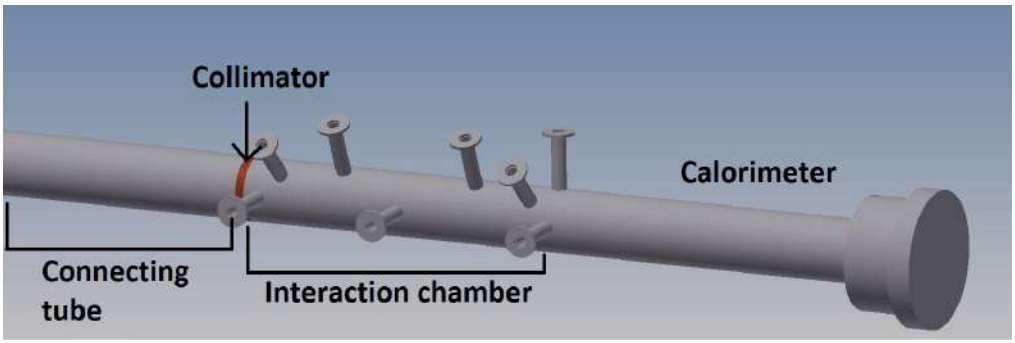

Figure 3.10: Sketch of the HPGe phase target chamber.

Once again the interaction chamber is preceded by a copper collimator 40 mm long and with a inner diameter of 7 mm and by a connecting tube for placing the chamber on the beam focus.

3.4.2 The HPGe detector

The $\gamma-$rays produced by the ^{2}H(p, γ)^{3}He reaction have been detected by a High Purity Germanium detector, p-type. It is basically a cylinder of germanium having a n-type contact on the outer surface and a p-type contact on the surface of an axial well (figure 3.11). Having a net impurity level of around 10^{10} $atoms/cm^3$, with a 5000 V reverse bias, the entire volume between the electrodes is depleted and an electric field extends across this active region inducing thus a drift of the charge produced by the photon interaction within this zone. The collected charge is proportional to the

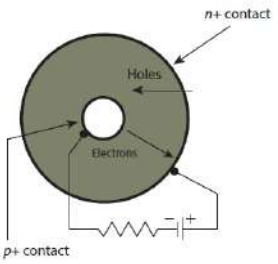

Figure 3.11: Sketch of a p-type germanium detector.

energy released and it is converted into a voltage pulse by a charge sensitive preamplifier. The main feature of a germanium detector is the high energy resolution, very sensitive to the noise produced by the leakage currents of free charges. In order to reduce the thermal generation of charge carriers,

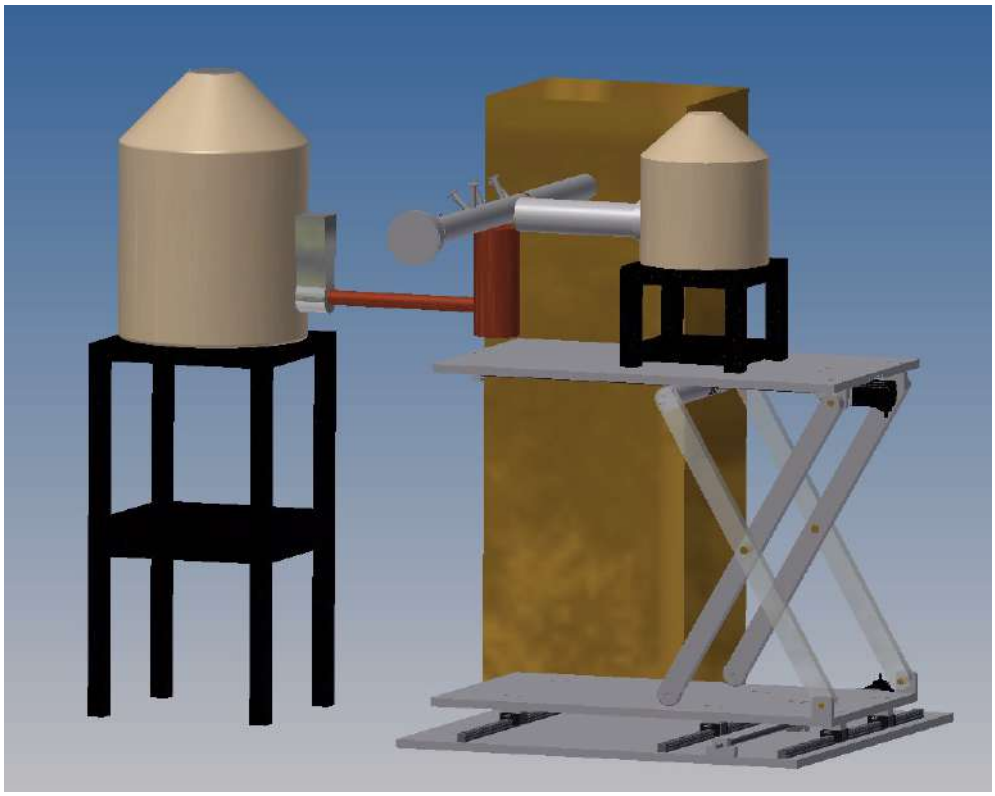

Figure 3.12: HPGe phase experimental set-up.

the germanium detector has to be cooled with liquid nitrogen.
The germanium crystal, having a 91 mm diameter and a 91 mm height, is protected by a copper envelope in contact with the liquid nitrogen dewar.

In order to evaluate the angular distribution of the emitted photons, the detection efficiency has to be known with high accuracy along all the target chamber. The procedure adopted for measuring it, accurately described in section 4.2.1, introduces an additional HPGe detector having a crystal diameter of 84.6 mm and a length of 87.8 mm enclosed in an aluminium envelope, as shown in figure 3.12.

3.4.3 Electonics and DAQ

The two germanium detectors outputs have been processed with two data acquisition systems running in parallel. As shown in figure 3.13, a SILENA 7716 power supply provides 5000 V to the main germanium detector, while an ORTEC 660 provides 4900 V to the auxiliary one. The preamplified signals coming from both the detectors are splitted using two active splitters

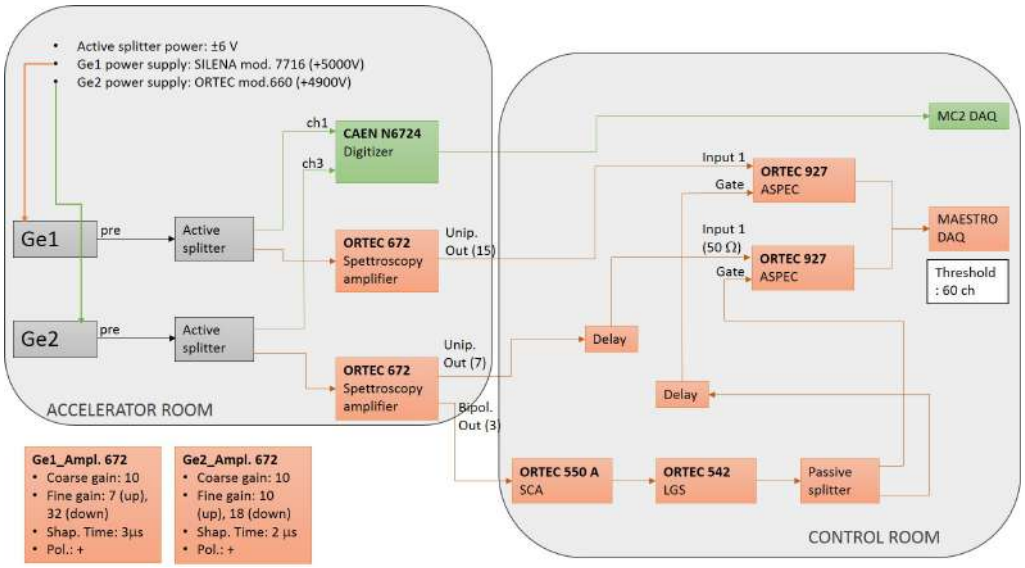

Figure 3.13: Block diagram of the HPGe acquisition chain.

leaving their amplitude unchanged. One of the two splitted signals is sent to a CAEN N6724 digitizer module (4 channels, 14 bit, 100 MS/s) and read by the *MC²Analyzer* software. The other splitted signal, sent to an ORTEC Spettroscopy Amplifier 672, is properly processed by the ORTEC electronic chain shown in figure 3.13 (further informations in section 4.2.1) and acquired by the MAESTRO software.
The main difference between the two acquisitions is that in the MAESTRO DAQ the coincidence between the two detectors signals is physically provided by an ASPEC module, while the CAEN DAQ is a list mode acquisition. This means that a timestamp is associated to each recorded event, allowing the signals coincidence to be performed offline.

CHAPTER 4

The $^2H(p,\gamma)^3He$ data analysis

This chapter is devoted to the description of the ^{2}H(p, γ)^{3}He measurements and the subsequent data analysis of the BGO phase. All the steps for the data reduction will be discussed starting from the analysis of the ancillary measurements of characterization of the entire set-up (ion beam, gas target and detectors) and arriving to the evaluation of the reaction *S-factor*.
Since the HPGe phase data taking has ended in September 2017, the data analysis is still ongoing and here only the preliminary results about the detector characterization will be shown.

4.1 The BGO phase

4.1.1 Target density study

The reaction yield Y is directly proportional to the target density ρ:

$$Y = \int_{z_0}^{z_1} \rho(z) \cdot \sigma(E(z)) \cdot \eta(E(z))\, dz \tag{4.1}$$

where z_0 and z_1 are the beginning and the end of the target, $\sigma(E(z))$ is the cross section at $E(z)$ energy and $\eta(E(z))$ is the absolute efficiency for a $\gamma - ray$ of energy E originating at position z. In case of an extended gas target, it is thus of crucial importance to know the density through which the ion beam passes. The gas pressure inside the chamber is always kept at a constant level by the feedback system, but the calorimeter hot side

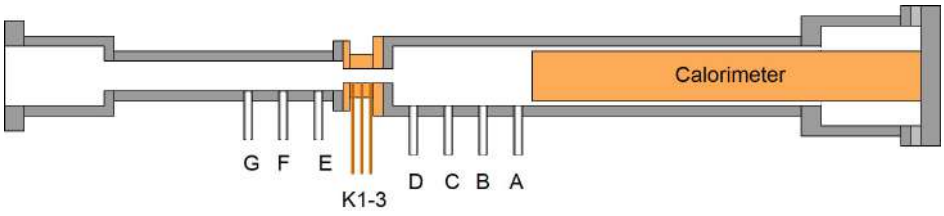

Figure 4.1: Sketch of the modified chamber used to measure the pressure and the temperature profiles.

and the collimator water cooling introduce a temperature gradient along the target chamber making the density to change. In order to evaluate the gas density profile, a set of measurements of pressure and temperature have been performed using a dedicated set up.
The target chamber used for this purpose has the same geometry as the chamber used for the ^{2}H(p,γ)^{3}He study but it is equipped with additional side tubes and flanges for connecting pressure and temperature gauges (figure 4.1). Three measurement points are obtained in the connecting tube, three in the collimator and four in the interaction chamber. Since no beam is required for these measurements, a simplified version of the collimator was made, consisting of a single copper piece with the three side tubes used for the pressure measurements. The side tubes, about 40 cm long and 3 mm in diameter, allowed to measure the pressure trend inside the collimator. The positioning of the side tubes in the interaction chamber has been designed to allow the simultaneous pressure measurements in different positions.

The target pressure profile has been measured using two capacitance pressure gauges: one MKS Baratron type 626A with 0.25% accuracy and one Pfeiffer CMR363 with 0.20% accuracy. An additional MKS gauge has always measured the nominal reference pressure at the interaction chamber center, through the small tube entering the chamber from the flange on the accelerator side. The two pressure gauges have been moved in order to cover all the apertures positions. The vacuum inside the second pumping stage (about a few 10^{-7}mbar) has been used as the reference value for the zero-adjustment of the pressure gauges. The deuterium profiles have been measured at different nominal pressures from 0 to 1 mbar (figure 4.2) in order to establish the optimal working condition and test the gas target capabilities. Inside the target chamber, the pressure is constant to $\pm$0.5%. Inside the collimator there is a monotonous decrease of the target pressure, as expected for a high-impedance tube. In the connecting tube, the trend continues to decrease with a lower slope, consistent with the fact that the 100 mm wide tube is significantly larger than the collimator and thus it has a lower gas

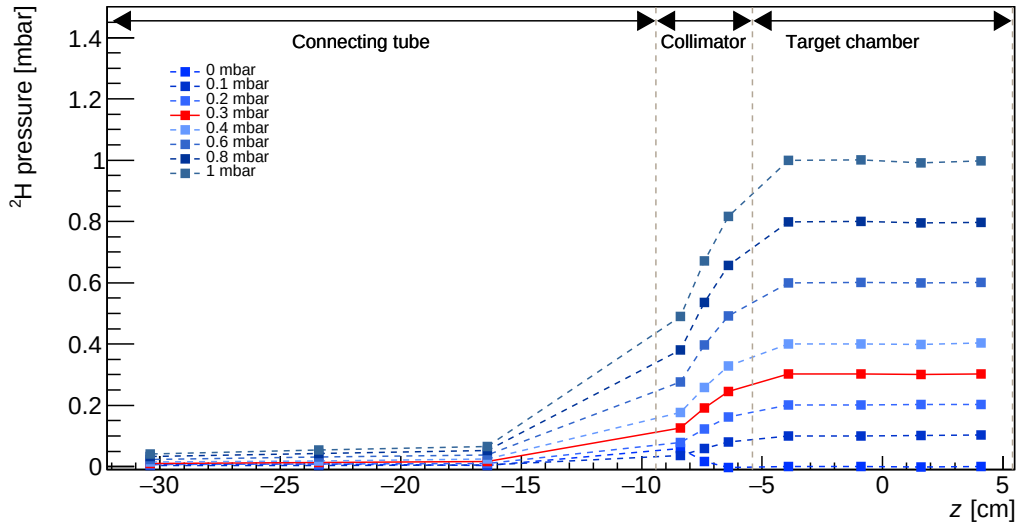

Figure 4.2: Measured pressure profiles in ^{2}H. Lines are only a guide to the eye. The red points refer to the reference working pressure.

flow impedance.

The gas temperature was measured in the target chamber and in the tube using three 1/3 DIN thin film Pt100 RTDs reaching the beam path and read by NI 9217 modules (4-Channel, 24-Bit, 100 Ω RTD Analog Input) in three-wire mode. The uncertainty associated to the RTD is 0.15 K, while an uncertainty of 0.2 K is quoted for the NI 9217 module. The thin platinum resistance of the RTD is deposited on a ceramic substrate and, depending on the RTD orientation, the platinum resistance may face the calorimeter or be on the opposite side. A maximum variation of 1 K has been observed changing the orientation of the RTD (4 different orientations) respect to the calorimeter hot surface so that an additional 1 K uncertainty has to be taken into account for the measurements. The temperature profile (figure 4.3) in the interaction chamber and in the tube is thus determined with a total uncertainty of 1 K, corresponding to 0.34%. Inside the target chamber, the temperature drops monotonously between the beam stop, heated to 343 K, and the collimator, cooled at 286 K, whose temperature has been measured by a RTD outside it. Consequently a 1% uncertainty on the absolute temperature is considered in the collimator measurement. Inside the connecting tube, the temperature increases from the cooling value to a constant plateau at about 294 K.

Knowing the p and T profiles, the density $\rho(z)$ (figure 4.4) has been

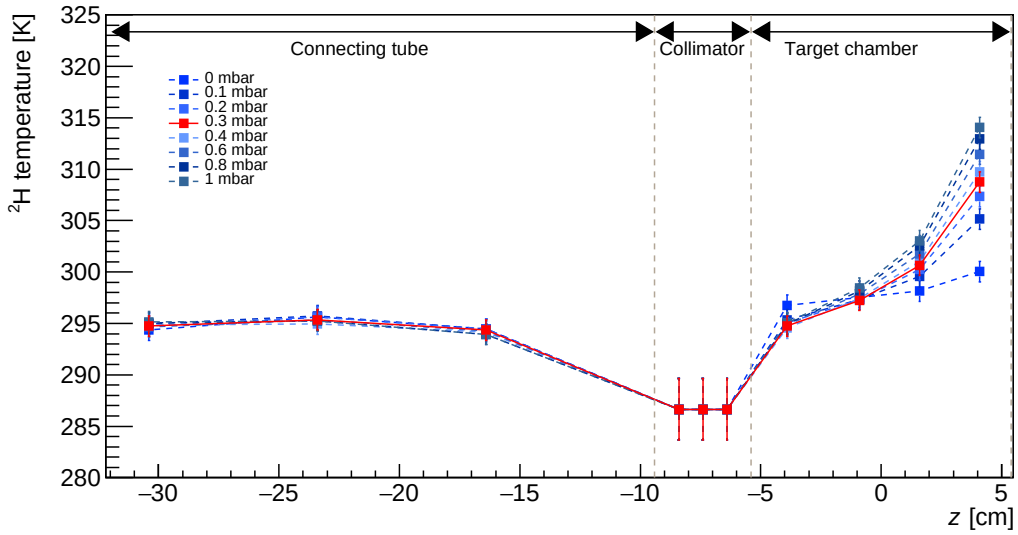

Figure 4.3: Measured temperature profiles in ^{2}H. Lines are only a guide to the eye. The red points refer to the reference working pressure.

obtained by the equation of state for an ideal gas[1]:

$$\rho(z) = \frac{\nu N}{V} = \frac{\nu \cdot p(z)}{k_B \cdot T(z)} \tag{4.2}$$

where N is the number of gas molecules per volume V, ν the number of gas atoms per molecule and k_B is the Boltzmann constant. The density values on the edges of the collimator, where no data are available, were extrapolated linearly from the trend in the interaction chamber and the connecting tube; while the density between successive points has been obtained by linear interpolation of the experimental points. Applying the propagation law, the uncertainty on the density profile inside the target chamber and the tube is 0.5%, while inside the collimator is 1%. An additional 1.1% uncertainty should be considered because of the choice of the interpolation used for the density evaluation. The total uncertainty on the density is thus 1.2% in the interaction chamber and in the tube and 1.5% in the collimator.
Integrating the density profile and normalizing it to the reference density in the middle of the chamber ρ_c, it is possible to define the effective target

[1]At the working conditions (high temperature and low pressure), the system can be approximated to an ideal gas because the potential energy due to intermolecular forces becomes less significant compared with the particles kinetic energy and the size of the molecules becomes less significant compared to the empty space between them.

	Nominal length [mm]	Effective length [mm]
Connecting tube	280	13.7± 0.2
Collimator	40	26.8 ± 0.4
Interaction chamber	108	107 ± 1.3
Total length	428	147.5 ± 1.9

Table 4.1: Effective lengths of the target chamber and its components.

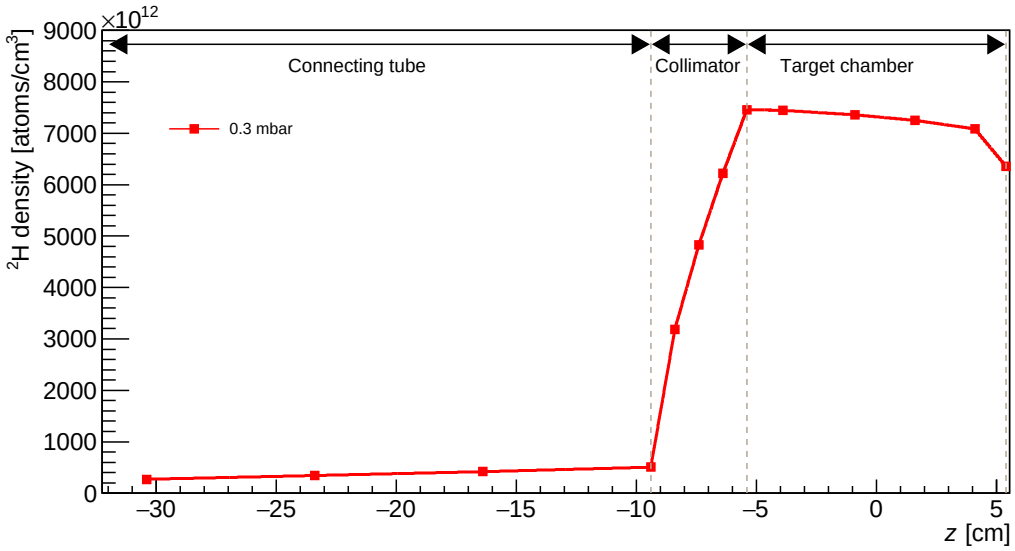

Figure 4.4: Calculated ^{2}H density profile at 0.3 mbar (reference operation pressure) according to equation (4.2). The line represents the interpolated density used in the energy loss calculations.

length:

$$l_{eff} = \frac{1}{\rho_c} \int_{z_0}^{z_1} \rho(z)\, dz \tag{4.3}$$

A summary of the calculated effective lengths is reported in table 4.1. Taking into account the uncertainties from the pressure and temperature measurements and the extrapolation, a total uncertainty of 1.3% is found for the integrated gas thickness.

4.1.2 The Beam Heating Effect

A high intensity beam passing through a gas volume loses energy by scattering with the target atoms. The power dissipated by the beam in the

gas depends mainly on the energy loss per unit length $\frac{dE}{dx}$ and on the beam current I [41]:

$$\frac{dW}{dx} = \frac{dE}{dx} \cdot I \cdot \frac{1}{e} \tag{4.4}$$

where e is the elementary charge. The energy loss is converted in heat, causing a local density reduction. In fact, the ideal gas law (equation (4.2)) allows the density to be expressed as a function of the temperature and the pressure. Since the target pressure is kept constant through the feedback system, an increase in temperature directly leads to a density reduction.

This effect has been studied experimentally for the deuterium gas target at 0.3 mbar of pressure performing measurements at constant beam energy and different currents. In figure 4.5 the results obtained with a proton beam of 300 keV of energy and a current changing from about 90 to 400 μA are shown, plotting the rate of events of the ^{2}H(p,γ)^{3}He reaction ROI, normalized to the charge, as a function of the current. Since all the points lay on the same line within 2σ error, no beam heating effect is thus experimentally appreciable. An estimation of it has been done using the data already published at LUNA, studing the beam heating effect in extended gas target of ^{14}N [42], using the resonance scan method, and of ^3He using the elastic double scattering [43]. These works find a linear behaviour between the relative target density $\frac{\rho}{\rho_0}$, where ρ_0 is the gas density without beam heating correction, and the power dissipated by the beam inside the gas per unit length $\frac{dW}{dx}$:

$$BH = \frac{\rho}{\rho_0} = 1 - \alpha \times \frac{dW}{dx}\left[\frac{mW}{cm}\right]. \tag{4.5}$$

Being the nitrogen a biatomic gas as deuterium and having the helium an atomic number comparable to the deuterium one, the α parameters known for these two gases have been used for evaluating the beam heating contribution in ^2H, calculating for each run conditions the power dissipated by the beam inside this gas. Considering the more critical experimental run conditions with a high current of 300 μA at 100 keV of proton energy, the beam heating contribution for deuterium has been obtained calculating BH as in equation (4.5), using the α parameters of nitrogen and helium and considering an average of them:

$$BH_1(deuterium) = 1 - \alpha_N \times \frac{dW}{dx} \tag{4.6}$$

$$BH_2(deuterium) = 1 - \alpha_{He} \times \frac{dW}{dx} \tag{4.7}$$

$$BH(deuterium) = 1.8\% \pm 0.5 \tag{4.8}$$

where the uncertainty has been calculated as $(BH_1 - BH_2)/2$.

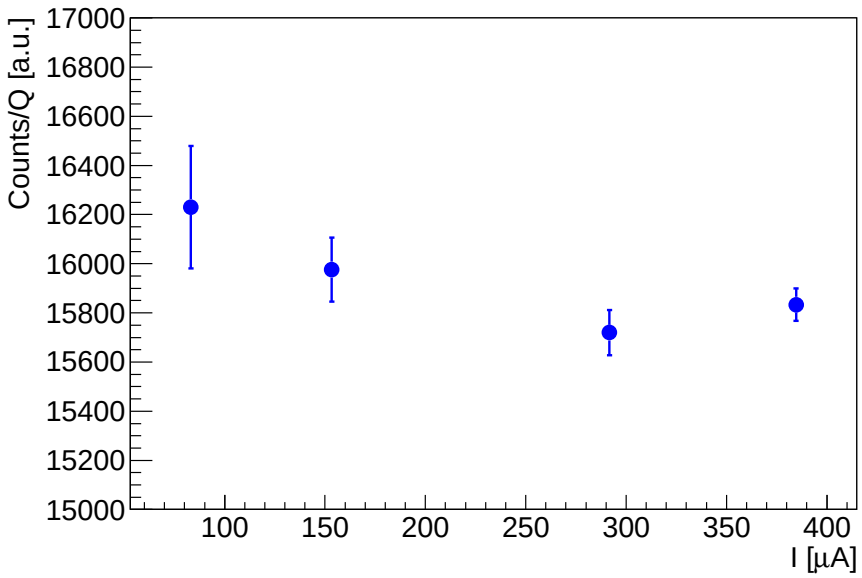

Figure 4.5: Experimental beam heating measurements in deuterium at 0.3 mbar of pressure at $E_p = 300$ keV: the counting rate normalized to the charge is plotted as a function of the proton current.

4.1.3 BGO energy resolution

The detector resolution has been studied initially using the ^{137}Cs, ^{60}Co and ^{88}Y radioactive sources for investigating the low energy range up to 2.7 MeV. The energy resolution is conventionally defined as the full width half maximum (FWHM) divided by the location of the peak centroid H_0 [44]:

$$R = \frac{FWHM}{H_0} \tag{4.9}$$

This definition assumes that any background or continuum on which the peak may be superimposed is negligible or has to be subtracted.
Since all BGO segments show a practically equal resolution (figure 4.6 left side), the fitting procedure for subtracting the background contribution and for calculating the peak FWHM has been applied only to one crystal (figure 4.6 right side). The results obtained for the three sources are shown in figure 4.7, where the FWHM is plotted as a function of the square root of the peak energy. The measured values, together with their uncertainty due to the fitting procedure, have been fitted with a first order polynomial to extrapolate the FWHM, and consequently the resolution, at higher energies. In the plot the ^{60}Co contribution is limited only to the sum peak of the

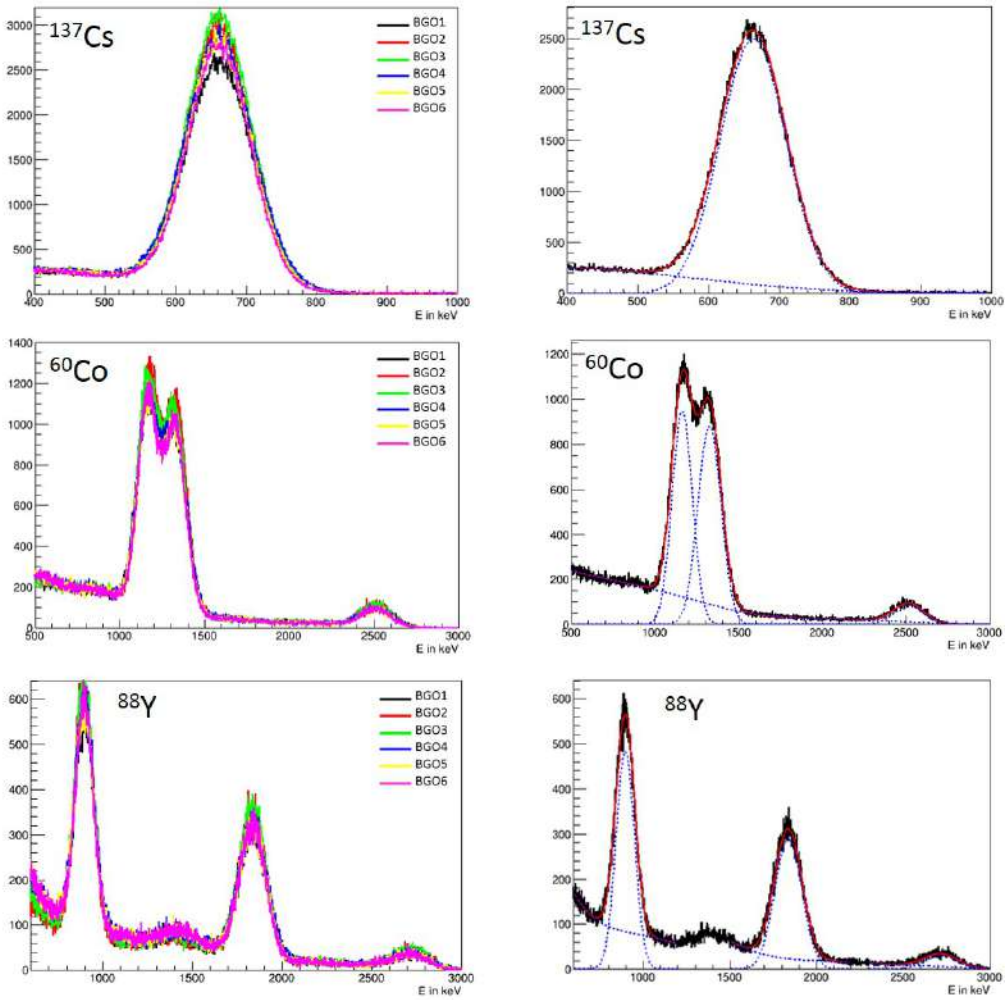

Figure 4.6: The left plots show the superimposition of the six BGO crystals for ^{137}Cs, ^{60}Co and ^{88}Y sources. The right plots represent the fit used for the resolution calculation for the same radioactive sources.

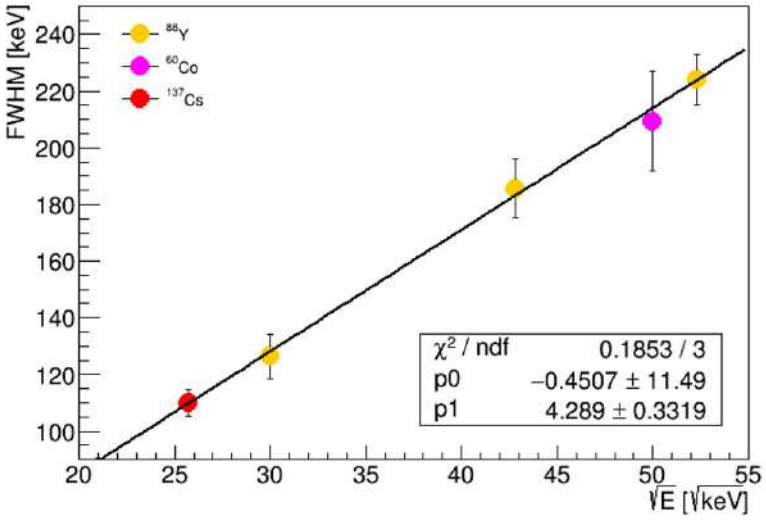

Figure 4.7: FWHM of ^{137}Cs, ^{60}Co and ^{88}Y as a function of the peak energy.

two emitted $\gamma - rays$, because of the poor BGO resolution making the fit of the double peak not precise. In order to verify the fit behaviour at higher energies, the well-known resonance at $E_p = 278$ keV in the reaction $^{14}\mathrm{N(p,\gamma)^{15}O}$ has been studied. Initially the agreement with the sources data is verified using the nitrogen $\gamma - rays$ at 1.3 and 2.3 MeV. Then, using the extrapolated FWHM value to fit the nitrogen spectrum, the resolution up to 7.5 MeV has been determined. In the graph 4.8 only the 7.5 MeV point is plotted, being the corresponding peak the least distorted by the other peaks contribution (figure 4.9). The final resolution results are summarized in table 4.2.

4.1.4 Detection efficiency

The absolute full-energy peak efficiency is defined as the ratio between the measured peak area and the number of gammas emitted at the same energy in the whole solid angle by a source. It can be determined as the ratio between the number of counts under the peak at a given energy $N(E)$ and the source activity A, the measurement time t and the branching ratio Br:

$$\eta = \frac{N(E)}{A \cdot t \cdot Br} \tag{4.10}$$

In an extended gas target, the interaction with the beam can take place in different positions along the beam axis, each one characterized by a different

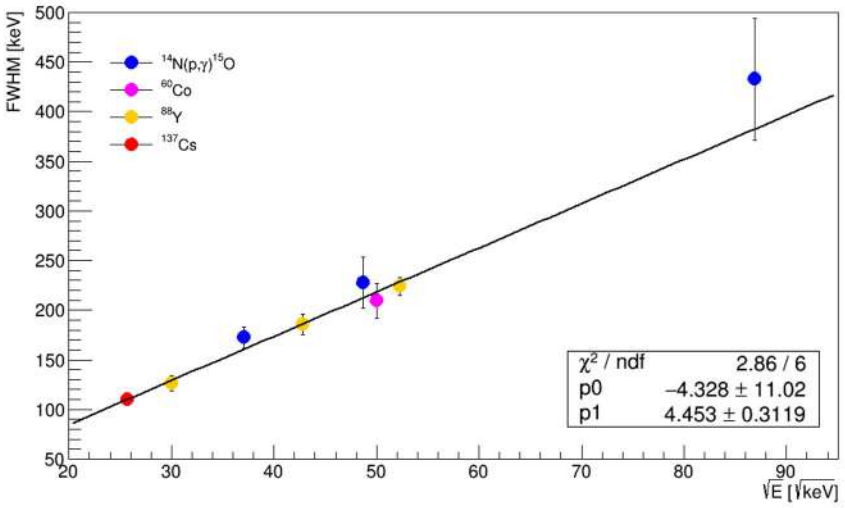

Figure 4.8: FWHM as a function of the peak energy for ^{137}Cs, ^{60}Co, ^{88}Y and ^{14}N(p, γ)^{15}O resonance at $E_p = 278$ keV.

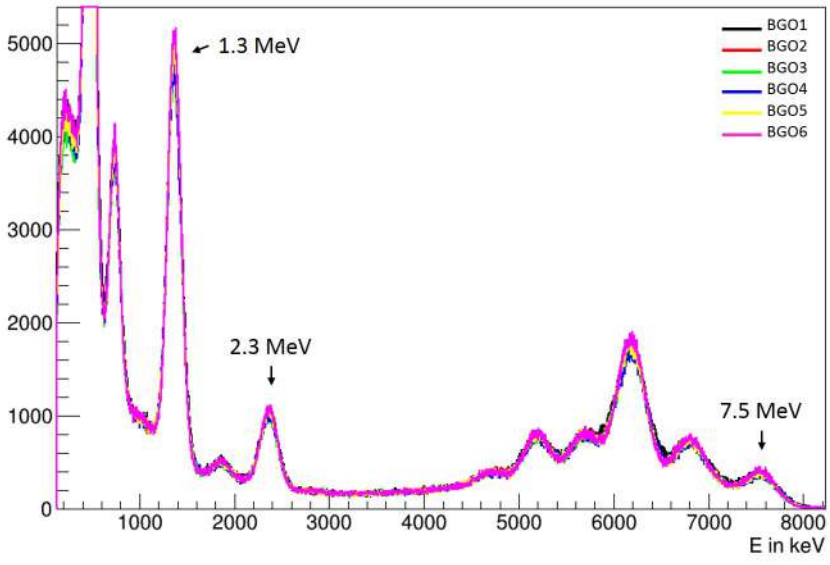

Figure 4.9: Spectrum of the ^{14}N(p, γ)^{15}O resonance at $E_p = 278$ keV of each BGO segment.

E_γ [keV]	FWHM [keV]	Resolution [%]
662	110	16.6
898	126	14.1
1384	172	12.5
1836	185	10.1
2315	227	9.6
2505	209	8.3
2734	224	8.2
7555	435	5.7

Table 4.2: Energy resolution of the BGO detector as a function of the peak energy.

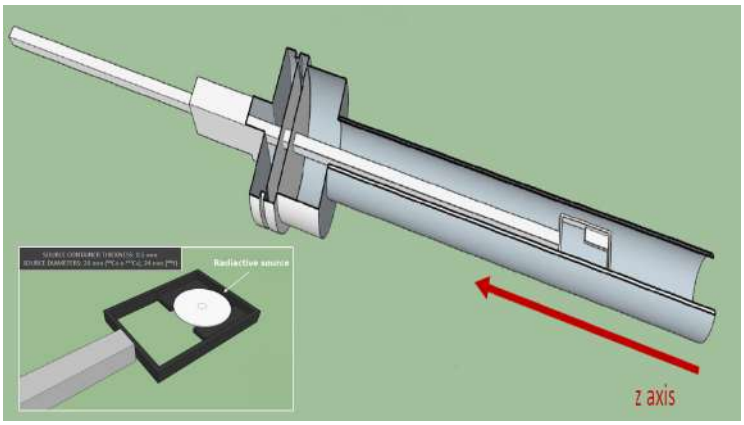

Figure 4.10: Draft of the sliding holder used for the sources measurement.

geometrical subtended angle to the detector. Since the detection efficiency depends on the emitted $\gamma - ray$ position inside the target chamber and on the photon energy, the study of the BGO set-up efficiency has been performed with several γ sources varying the position along the beam axis. A Geant3 Monte Carlo simulation has been developed to study the detection efficiency of the set-up. The simulation has been tuned to match the experimental data: at low energies the efficiency is measured with radioactive calibrated sources; while at higher energies, where the signals are expected during the $^{2}\mathrm{H}(\mathrm{p},\gamma)^{3}\mathrm{He}$ study, using the photons emitted from the $^{14}\mathrm{N}(\mathrm{p},\gamma)^{15}\mathrm{O}$ resonance at $E_p^{res} = 278$ keV [45].

Three pointlike sources are used for the measurement: ^{137}Cs emitting a 662 keV photon, ^{60}Co emitting two gammas in cascade one at 1173 keV and the other at 1332 keV and ^{88}Y emitting also two photons in cascade at 898 keV and at 1836 keV. A sliding holder (figure 4.10) fixed to the

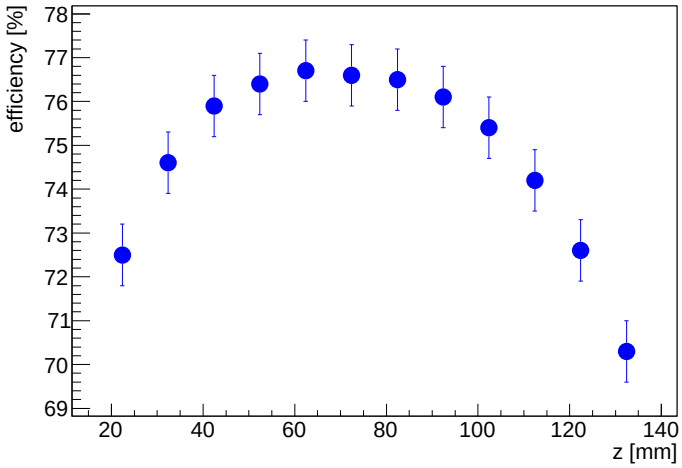

Figure 4.11: BGO efficiency as a function of the distance from the collimator measured moving a ^{137}Cs source along the beam axis. The zero position corresponds to the collimator.

back flange of the chamber has been realized in order to place the source at several distances from the collimator to the calorimeter along the beam axis. The holder consists of a plastic frame supported by an aluminium rod which can slide inside a guide till the end of the chamber. Figure 4.11 shows the experimental efficiency profile for the ^{137}Cs source as a function of the distance from the collimator. The plot confirms that the detector reachs the maximum efficiency value at the centre. Similar curves have been obtained for all radioactive sources, arriving to the maximum photon energy of 2.7 MeV of the ^{88}Y sum peak.

At higher energies, as already said, the $^{14}\mathrm{N(p,\gamma)^{15}O}$ resonance at $E_p = 278$ keV has been used. A nitrogen gas target is employed at 5 mbar of pressure to allow the resonance strength to be sufficiently narrow in safe pumps operating conditions. Varying the proton energy in 1-2 keV steps, the resonance is populated at different positions inside the chamber. In order to reduce the uncertainty on this measurement, a collimated NaI detector is used in a close geometry with the chamber to physically identify the position of the resonance inside the target at the same measurement positions used for the sources. Figure 4.12 shows, for example, the results obtained keeping the NaI detector fixed at 54 mm from the collimator and moving the resonance forward and backward changing the proton energy until the achievement of the maximum counting rate.

The result of the comparison between the experimental data and the

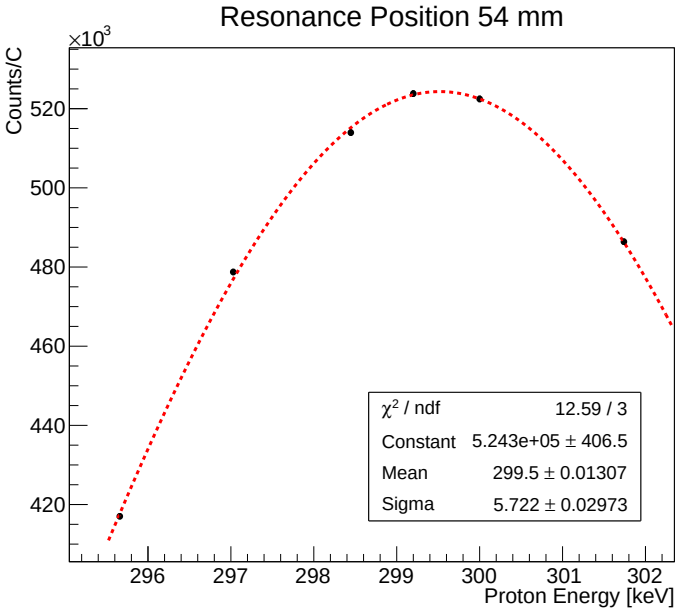

Figure 4.12: Energy scan of the $^{14}\mathrm{N}(\mathrm{p},\gamma)^{15}\mathrm{O}$ resonance keeping the NaI detector fixed at 54 mm from the collimator.

Monte Carlo simulation, both for the sources and the nitrogen, shows a really good agreement between the two curves (figure 4.13), granting that the Geant3 code works fine in a large gamma energy interval: from 662 keV of the ^{137}Cs source up to 8 MeV of the $^{14}\mathrm{N}(\mathrm{p},\gamma)^{15}\mathrm{O}$ reaction. Using this approach, a total BGO efficiency of 62% is evaluated at 5.6 MeV of energy.
The uncertainty on the efficiency has been calculated comparing the experimental and the simulated summing spectra[2] of the $^{14}\mathrm{N}(\mathrm{p},\gamma)^{15}\mathrm{O}$ resonance at $E_p = 278$ keV. 10^6 events have been simulated and the two spectra have been normalized so that both the integrals in the energy range 3-8.4 MeV were equal to 10^6. Then, selecting the energy ROI used for the $^{2}\mathrm{H}(\mathrm{p},\gamma)^{3}\mathrm{He}$ reaction 4000-6500 keV, the comparison between the spectra integral in that region, reveals that the simulated spectrum detects the 45.3% of the total events, while the experimental one the 43.5%, as shown in figure 4.14. The difference in the counts number between the two spectra, normalized to the total number of events 10^6, is 2% and it has been assumed as the uncertainty

[2]Since the same photon can be simultaneously detected by more than one crystal, the summing spectrum in figure 4.14 has been realized fixing a time windows of 3.5 μs and summing the coincident events within that interval, exploiting the list mode saved spectra. The window choice is due to the shaping time of the trapezoidal filtering algorithm used in the pulse height analysis operate by the digitizer.

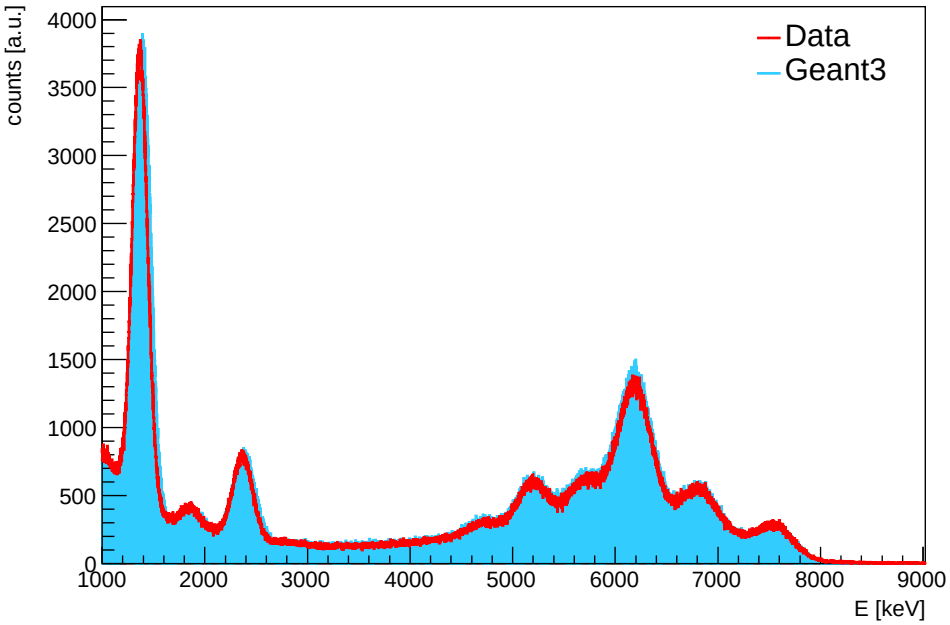

(a)

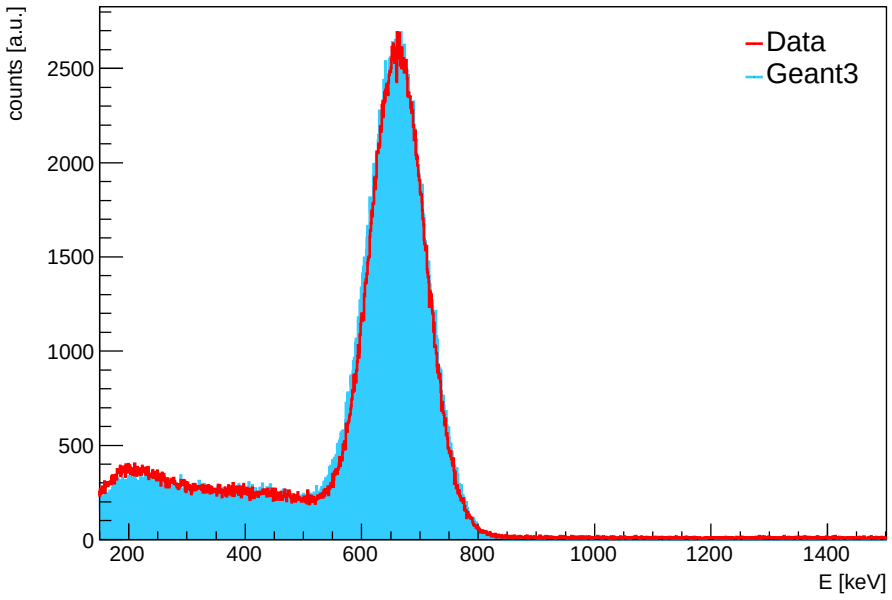

(b)

Figure 4.13: Comparison between experimental data and Geant3 simulation: (a) ^{14}N(p, γ)^{15}O resonance spectra; (b) ^{137}Cs spectra.

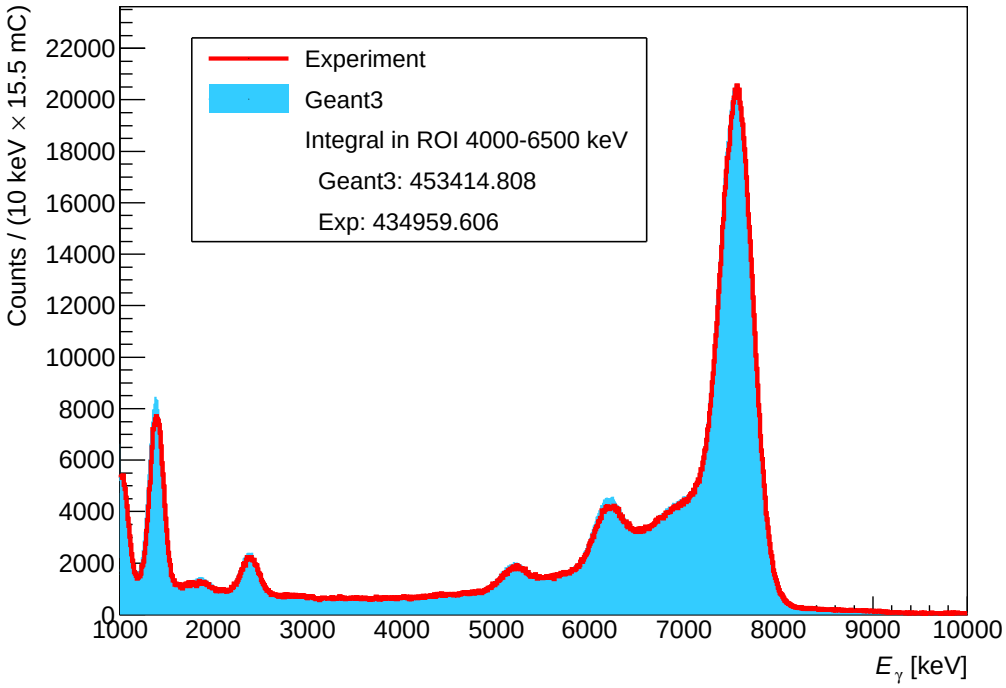

Figure 4.14: Comparison between the experimental and simulated summing spectra of the $^{14}\mathrm{N}(\mathrm{p},\gamma)^{15}\mathrm{O}$ resonance at $E_p = 278$ keV for the efficiency uncertainty evaluation.

on the BGO detecting efficiency.

A further measurement has been performed to test the detector operation. After removing the target chamber, the ^{88}Y source, included between two lead cylinders, has been moved inside the BGO cavity. Thanks to this lead collimator, the detector response has been tested all along its length, for $\gamma - rays$ emitted perpendicularly to its axis. The efficiency profile measured for each of the six segments is shown in figure 4.15 where the detector exhibits a constant behaviour in the center where the scattering chamber is placed, while closer to the PMTs the efficiency starts decreasing slightly before than expected. This is probably due to an inefficient light collection close to the PMTs, because their circular shape don't match exactly the crystal shape.

4.1.5 The BGO background

Direct measurements of cross section at energies of astrophysical interest require a very low background because its magnitude ultimately determines

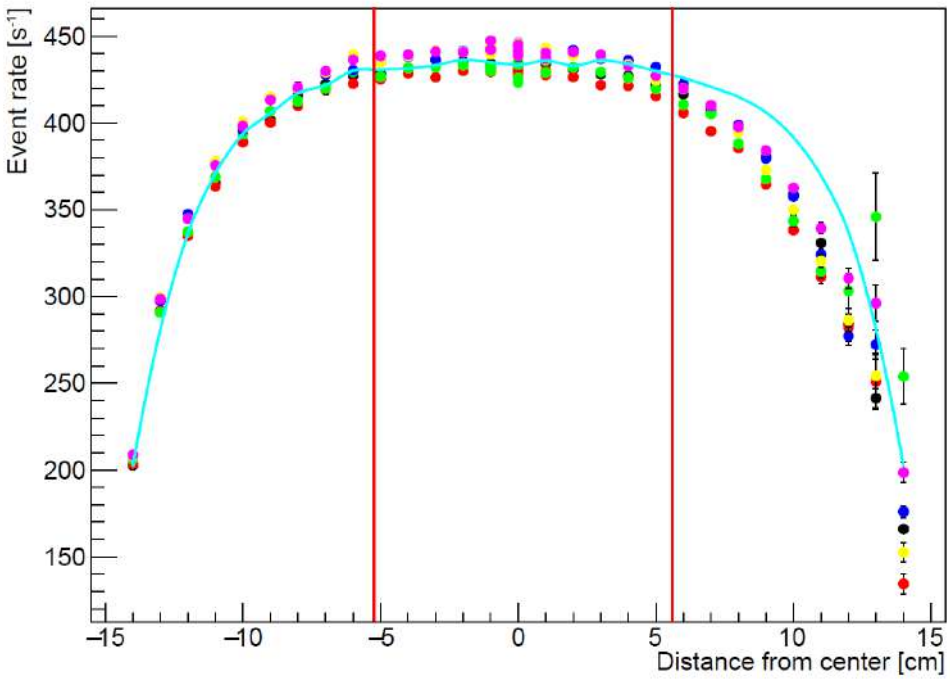

Figure 4.15: Comparison between the experimental and simulated data (blue line) for the test with the ^{88}Y source. The two red vertical lines delimit the position of the interaction chamber in the running configuration. The dot colours identify the six BGO crystals.

the minimum detectable signal. It has two main components:

- natural background;
- beam induced background.

Their contribution varies greatly with the detector size and type, with the extent of the shielding that may be placed around it, with the place where it is installed and finally with the beam energy and the characteristics of the target.

The natural background

The natural background is the result of several contributions [44]:

- the natural radioactivity of the constituent materials of the detector itself;
- the natural radioactivity of the ancillary equipment, supports and shielding placed in the immediate vicinity of the detector;
- radioactivity in the air surrounding the detector;
- the primary and secondary components of the cosmic radiation.

Figure 4.16 shows the natural background spectrum acquired by the BGO detector. Three main peaks are well distinguishable: the ^{208}Tl belonging to the thorium radioactive chain causes the peak at 2614 keV, the ^{214}Bi produced by the uranium chain gives rise to the peak at 2204 keV and finally the very intense peak at 1460 keV is the ^{40}K.
The ventilation system in the laboratory makes air flow inside the experimental room, preventing the radon accumulation close to the detector. Anyway, because of the variation in radon concentration inside the laboratory, the low energy background may also change slightly from time to time. However, as evident in the spectrum, the contribution of the natural background in the region of interest of the $^2\mathrm{H}(\mathrm{p},\gamma)^3\mathrm{He}$ reaction (the green band in figure 4.16) is completely negligible.

The beam induced background

The beam can induce undesired nuclear reactions in the target or in the surrounding materials because of the presence of particular contaminants inside the scattering chamber, giving rise to a beam induced background. This contribution varies from run to run depending on the proton energy because

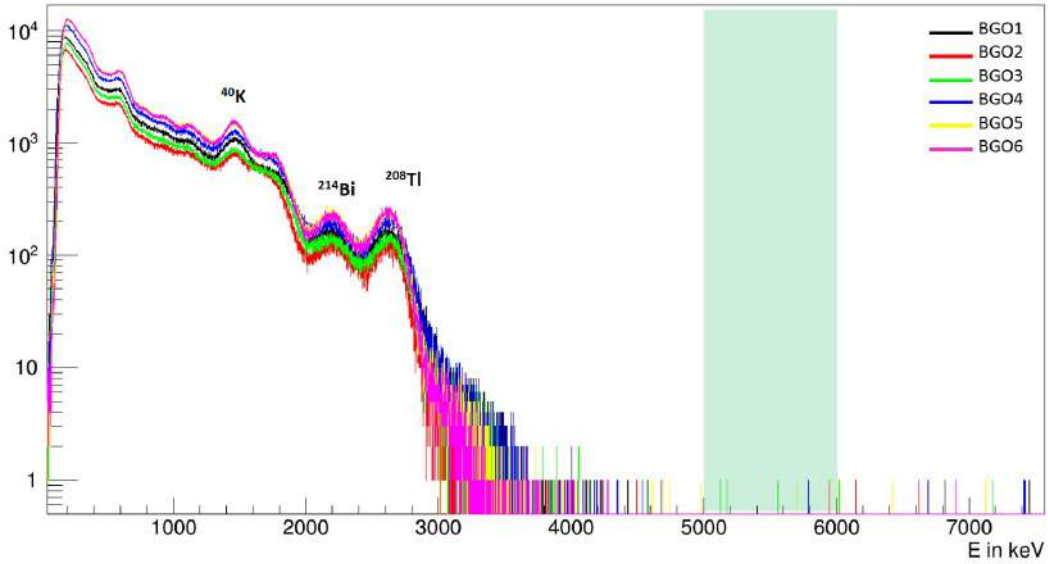

Figure 4.16: BGO natural background spectrum. The vertical green band identifies the region of interest (ROI) for the ^{2}H(p, γ)^{3}He reaction used for the following analysis.

different nuclear reactions may occur causing a significant background, especially if a resonance is populated. Some nuclear reactions can produce photons having energy in the range of ^{2}H(p, γ)^{3}He reaction, according to the Q-value and the beam energy. This not only gives rise to a full energy peak, but also causes a Compton continuum extending over a wide energy range. Changing the proton energy, two beam induced background contributions have been identified: one due to the direct capture ^{12}C(p, γ)^{13}N, giving rise to two photons of energy 2.1 and 2.3 MeV, and the other due to the ^{11}B(p, γ)^{12}C, producing a $\gamma-$ray of 4.4 MeV (figure 4.17). In both cases the peaks fall out of the ROI of the deuterium reaction. The main source of background in this experiment, instead, is the ^{19}F(p, $\alpha\gamma$)^{16}O reaction, having a resonance at $E_{beam} = 340$ keV [46], which gives rise to a 6130 keV photon. The fluorine could be found in the chemical composition of some set-up components, as for example the vacuum o-ring or the teflon calorimeter flange, and consequently its contamination is not removable. Figure 4.18 shows the spectrum measured running in vacuum at different beam energies: for $E_{beam} > 300$ keV the full-energy peak and the first escape of the fluorine resonance peak are well visible, while for $E_{beam} < 300$ keV the beam induced background contribution can be considered negligible. Because of the poor BGO energy resolution, the investigation of the reaction behaviour for $E_{beam} > 300$

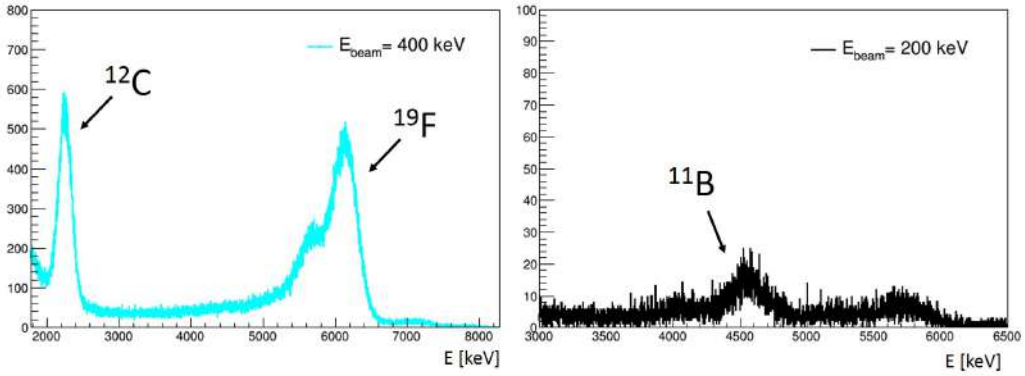

Figure 4.17: The beam induced background spectra obtained in vacuum at 400 keV and 200 keV of proton energy show the carbon and boron contaminations.

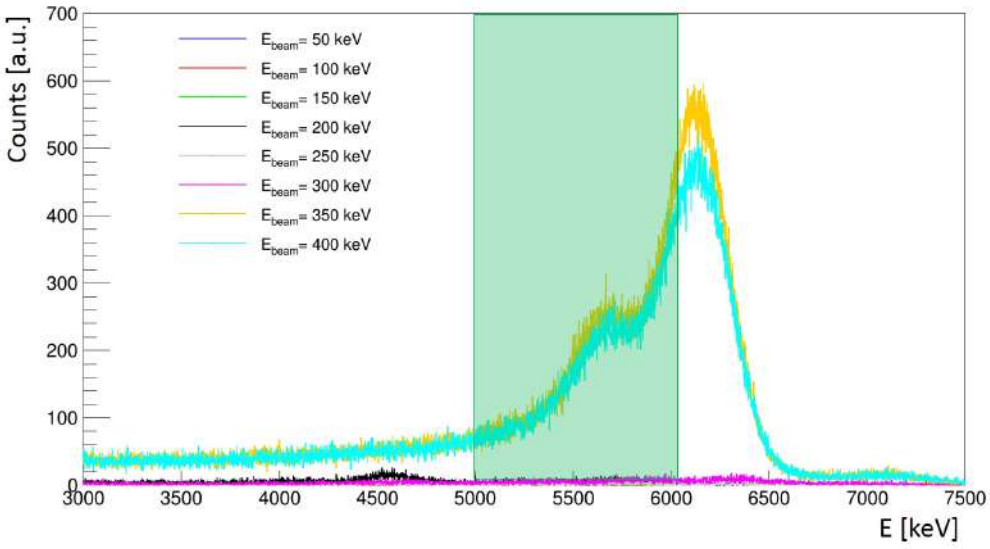

Figure 4.18: Beam induced background spectrum obtained in vacuum changing the proton energy. The vertical green band identifies the reaction ROI used for the analysis.

keV has been performed during the HPGe phase, exploiting the high energy resolution of a germanium detector.

4.1.6 The $^2H(p,\gamma)^3He$ S-Factor calculation

Because of the energy loss of the proton beam passing through the gas, the reaction cross section varies along the target length and the number of target atoms is also changing according to the deuterium pressure profile along the beam path. Fusion reactions can therefore take place in different positions and the emitted photons can be detected by the BGO with an efficiency depending on that position. Being z the coordinate along the beam path and L the target length, the number of detected photons N_γ is given by [3]

$$N_\gamma = N_p \int_0^L \sigma(E(z)) \cdot \rho(z) \cdot \eta(E(z)) dz \tag{4.11}$$

where N_p is the number of projectiles impinging on the calorimeter, ρ the gas density, σ the reaction cross section and η the detection efficiency.
The laboratory energy of the projectiles at z is given by

$$E_{p(z)} = E_{beam} - \int_0^z \frac{dE}{dz} dz \tag{4.12}$$

where E_{beam} is the laboratory accelerator beam energy and $\frac{dE}{dz}$ is the energy loss of protons in the deuterium gas [39]. According to equation (1.23), the cross section of ^{2}H(p,γ)^{3}He is expected to be continuously varying with energy and an effective cross section σ_{eff}, calculated as the average over the interaction energies, can be extracted:

$$\sigma_{eff} = \frac{N_\gamma}{N_p \int_0^L \rho(z) \cdot \eta(E(z)) dz} \tag{4.13}$$

From equation (4.13), the S(E) factor can be deduced, according to definition (1.23), provided that an average interaction energy of the detected capture reactions, $E = E_{eff}$, is introduced

$$S(E) = \sigma_{eff} \cdot E_{eff} \cdot e^{2\pi\eta}. \tag{4.14}$$

E_{eff} and the integral in equation (4.13) are calculated by the Geant3 code for the experimental conditions of each run (i.e. beam energy, target pressures and beam current). The code received as input the measured density profile along the beam path corrected by the beam heating effect.

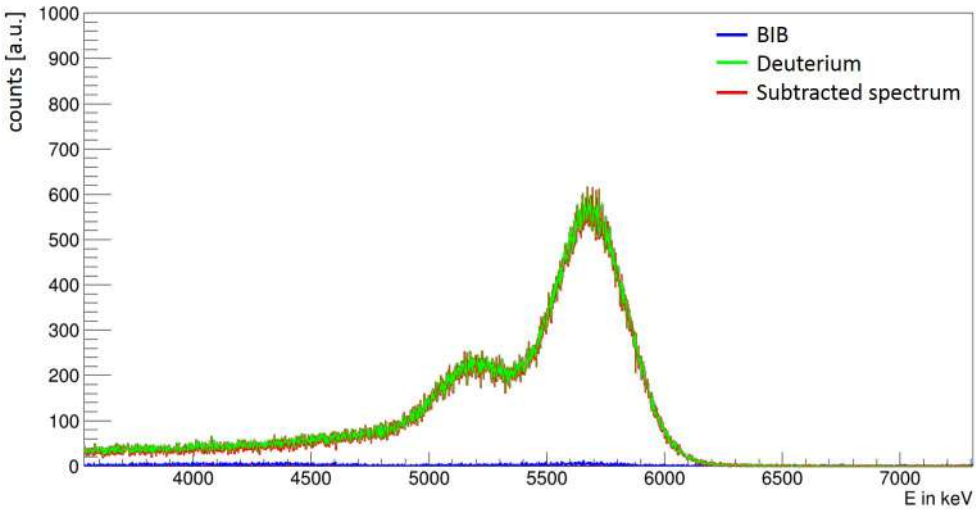

Figure 4.19: ^{2}H(p, γ)^{3}He spectrum at E_p = 150 keV: the green line is the deuterium run spectrum, the blue line the vacuum run spectrum and the red line is effective reaction signal obtained subtracting the background contribution to the deuterium run.

The number of detected events N_γ, instead, has been obtained directly from the BGO spectra. For each investigated energy, two runs have been performed: one with deuterium gas inside the scattering chamber, the other in vacuum in order to evaluate the beam induced background contribution or the eventual deuterium implantation. For each deuterium spectrum, an energy ROI (4000-6500 keV), including the reaction photopeak and its first escape, has been selected. After having subtracted the natural and beam induced background contributions, properly normalized to the charge (figure 4.19), the N_γ quantity has been calculated integrating each BGO crystal spectrum within the ROI and summing up the counts number. The Monte Carlo code has verified that summing up the response of the six independent BGO sectors does not involve a significant loss of information, being the ^{2}H(p, γ)^{3}He reaction characterized by a single $\gamma-$ray per event.

Finally the number of projectiles N_p in equation (4.13) has been deduced from the calorimeter measurements, as explained in section 3.2.

The uncertainty with which the S-factor has been calculated consists of two main contributions: a statistical and a systematic one.
Looking at the definition of S-factor (equation (4.14)) the only term affected by statistical error is the effective cross section. The uncertainty on this quantity has been evaluated propagating the statistical error on N_γ and on N_p. The first is given by the square root of the counts number. For

what concern the second, since N_p depends on the calorimetric power and its electrical calibration (section 3.2), the uncertainty has been calculated as $\sqrt{(W_{cal}\cdot\Delta m)^2+(m\cdot\Delta W_{cal})^2+\Delta q^2}$, being Δm and Δq the errors on the fit parameters of the electrical calibration (equation 3.5) and ΔW_{cal} the uncertainty on the calorimetric power already defined in section 3.2.
The systematic error, instead, has been calculated, according to the propagation law, as follow:

$$\Delta S_{sist.} = \left[\left(\frac{E_{eff}}{e^{-2\pi\eta}}\cdot\Delta(\sigma_{eff})\right)^2+\left(\frac{\sigma_{eff}}{e^{-2\pi\eta}}\cdot\Delta(E_{eff})\right)^2+ + \left(\sigma_{eff}E_{eff}\cdot\Delta(e^{2\pi\eta})\right)^2\right]^{1/2} \tag{4.15}$$

The systematic uncertainty on the effective energy and on the integral in equation (4.13) has been evaluated running the Monte Carlo code for different conditions of the experiment. In particular, considering the uncertainties on the pressure and temperature profiles discussed in section 4.1.1, an upper and a lower density profiles are determined and given as an input to the code. The simulation results on the integral in equation (4.13) are affected by a 2.1% systematic error, while the effective energy E_{eff} by a 0.02%. Finally a 1.5% systematic error has been considered on the calorimeter electrical power due to the uncertainty with which the current is read on the secondary electrons suppression ring used during the calibration: having a current of 3 μA on the ring, with 200 μA on the calorimeter, a conservative maximum error equal to the ring current itself has been assumed.
The results obtained are summarized in table 4.3 with the statistical and systematic uncertainties. Last column reveals that the total error, calculated by summing in quadrature the previous two contributions, is about 3%. Only at low energies a higher error is obtained because of the low beam current during the run, involving a low power difference in calculating W_{cal}.

4.2 The HPGe phase

4.2.1 Detection efficiency

Preliminary test

The set-up efficiency has been measured exploiting the coincidence between two γ-rays emitted in cascade and detected by two different detectors, one of which used as the acquisition trigger.
Before mounting the set-up at the LNGS, the method has been studied and

$E_{c.m.}$ [keV]	S(E) [eV b]	σ_{stat} [%]	σ_{sist} [%]	σ_{tot} [%]
33	0.49	5.6	2.8	6.2
39	0.53	3.5	2.8	4.4
46	0.61	4.9	2.7	5.6
56	0.63	1.8	2.7	3.2
66	0.71	1.5	2.7	3.1
67	0.80	2.5	2.7	3.6
79	0.85	1.5	2.7	3.1
89	0.90	1.2	2.7	3.0
101	1.05	0.5	2.7	2.7
113	1.13	0.9	2.7	2.9
123	1.14	0.8	2.7	2.8
133	1.32	0.7	2.7	2.8
133	1.25	0.8	2.7	2.8
146	1.40	0.8	2.7	2.8
167	1.71	1.0	2.7	2.9
179	1.69	0.7	2.7	2.8
200	2.06	0.8	2.7	2.8

Table 4.3: Measured ^{2}H(p, γ)^{3}He reaction S-factor values as a function of the center of mass energy.

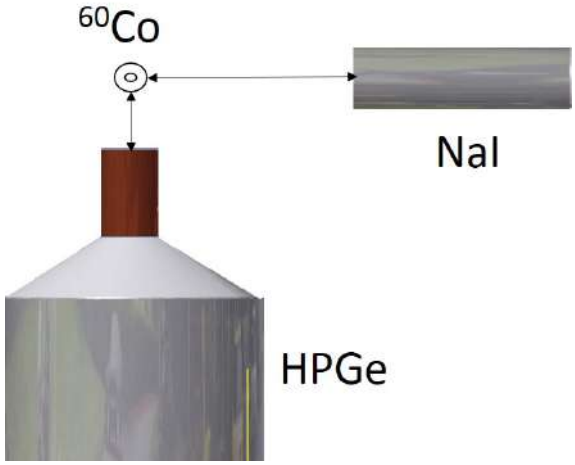

Figure 4.20: Sketch of the experimental set-up realized in Bari for testing the coincidence method for the HPGe efficiency evaluation.

tested at INFN laboratories of Bari using a ^{60}Co source for measuring the efficiency of a HPGe detector of the Bari group at 1.33 MeV of energy through a coincidence with a NaI detector (figure 4.20). The ^{60}Co decays by $\beta-$ emission to ^{60}Ni, producing two photons in cascade with a branching ratio of 99.88%. This means that, for each radioactive decay process, two photons, $\gamma_1 = 1.17$ MeV and $\gamma_2 = 1.33$ MeV, are produced. Whenever the first counter detects an event γ_1, it enables the other counter that can thus detect the cascade emitted photon γ_2. The detection efficiency of the HPGe detector can be evaluated by the ratio between the number of events that has triggered the acquisition and the number of events actually acquired by the detector itself, taking into account the angular correlation function $W(\theta)$ between the two photons. This function for an angle θ between two successive $\gamma-$rays can be written as [47]

$$W(\theta) = \sum_l a_l P_l(cos\theta) \tag{4.16}$$

where a_l are the coefficients dependent on the nuclear spins of the states involved and on the angular momentum carried by the $\gamma-$rays, while P_l are the Legendre polynomials. The sum in this equation involves only the events values of l to conserve the parity.
The ^{60}Co angular correlation function has already been studied and it is well known in literature. As shown in figure 4.21, being $W(\theta = 90^o) = 1$, in the following the efficiency will be calculated considering only the ratio between the two detectors counting number.

In order to calculate the germanium efficiency at 1.33 MeV of energy,

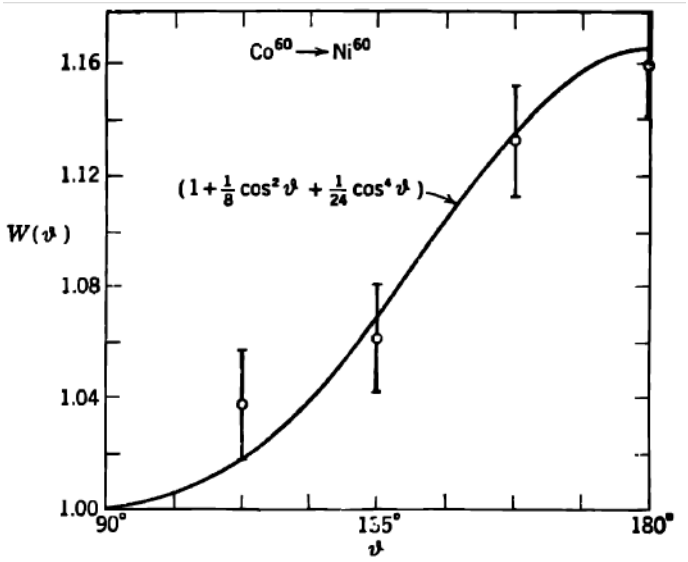

Figure 4.21: ^{60}Co angular correlation function as a function of the angle between the two emitted photons θ [47].

the events at 1.17 MeV have been selected with the NaI detector, using a Single Channel Analyzer (SCA) (figure 4.22). The signals are acquired by an ORTEC $ASPEC-972$ module. As shown in figure 4.22, this module is characterized by two analogical inputs with two corresponding gates enabling the acquisition. Input 1 acquires the analogical germanium signal, while input 2 the NaI one. The gate, the same one for both channels, is given by the scintillator and it is properly processed in order to have logic and analogue signals in time. When the scintillator detects an event in the energy range of interest, the HPGe is enabled and can detect the corresponding photon in cascade. It follows that, if the trigger detector acquires at the same time a partially and a totally absorbed photon, this event does not contribute to the final efficiency evaluation, because the germanium has not been enabled.
Shown below the results of the data analysis of the preliminary test performed in Bari using the set-up described above.
First of all the NaI inclusive spectrum of ^{60}Co has been studied in order to evaluate the background contribution under the triggering peak at 1.17 MeV. As shown in figure 4.23, the spectrum, after having subtracted the natural background, has been fitted taking into account the two gamma photopeaks and the two corresponding Compton edges. The background contribution due to the source has thus been calculated as the ratio between the area under the fitting gaussian A_{range} and the histogram integral I_{range} in the

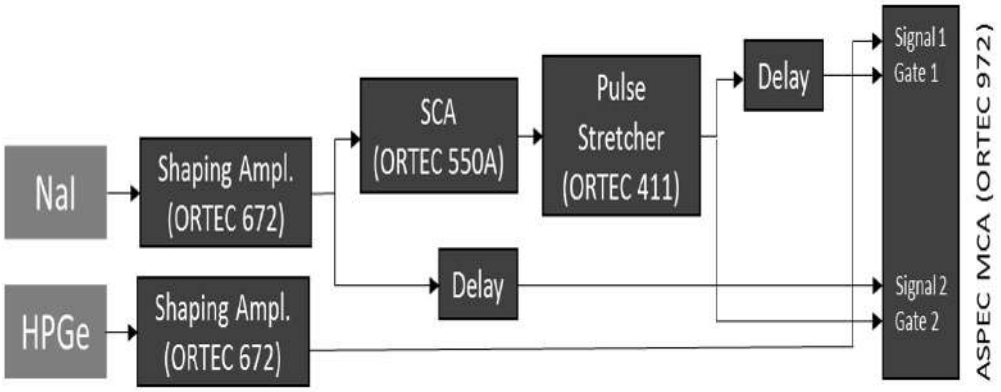

Figure 4.22: Block diagram of the processing signal electronic used for testing the coincidence method.

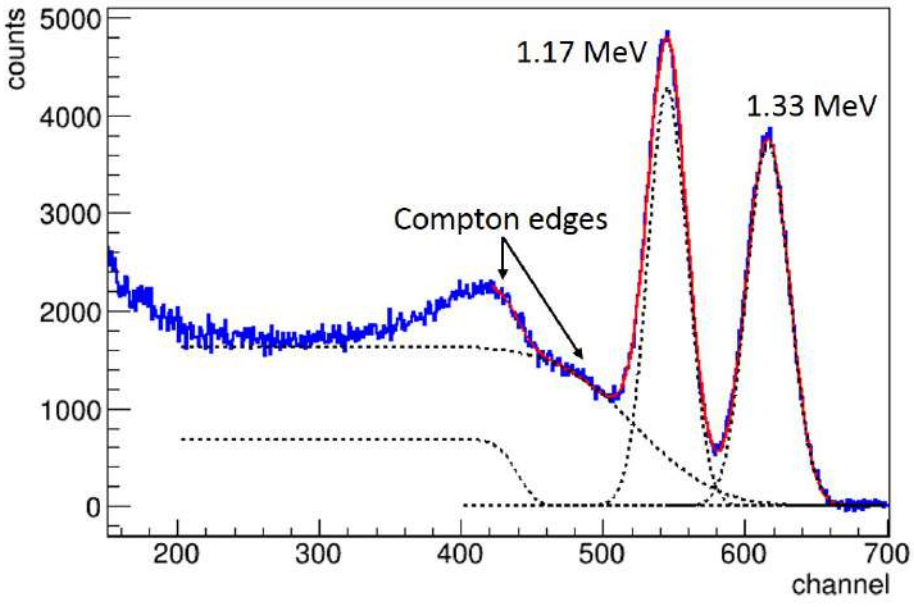

Figure 4.23: Inclusive ^{60}Co spectrum acquired by the NaI detector fitted by a double gaussian and a double erf.

energy range fixed by the SCA:

$$Bkg = 1 - \frac{A_{range}}{I_{range}} = 20.88\% \tag{4.17}$$

The coincidence spectra acquired by the NaI and the HPGe detectors are shown in figure 4.24: the NaI one displays the only peak at 1.17 MeV selected by the SCA module; while the germaniun spectrum reveals the coincidence peak at 1.33 MeV.

Indicating with N_1 the NaI counts number without the natural and the source background contributions and with N_2 the HPGe counts number under the peak at 1.33 MeV, the absolute efficiency can be calculated as

$$\epsilon_{abs} = \frac{N_2}{N_1} = 0.055\% \tag{4.18}$$

and the intrinsic[3] one as

$$\epsilon_{int} = \epsilon_{abs} \cdot \frac{4\pi}{\Omega} = 16.78\% \tag{4.19}$$

where Ω is the solid angle subtended to the germanium detector.
The uncertainty on the efficiency evaluation is given by two contributions: a statistic one, depending on the square root of N_1 and N_2, and a systematic one depending mainly on the choice of the fitting function used for the NaI inclusive spectrum.

In order to check the validity of the measurement, the efficiency evaluated using the coincidence method has been compared with the one provided by the datasheet of the HPGe detector, where the absolute efficiency is given in relation to a known 3x3 NaI efficiency at a source-detector distance of 25 cm ($\epsilon_{NaI} = 1.2 \cdot 10^{-3}$). The ratio in equation 4.20, expressed as a percentage, provides the relative efficiency of the germanium:

$$\epsilon_{rel} = \frac{P_A/[A \cdot t_l]}{\epsilon_{NaI}} \cdot 100 = \begin{cases} 38\% & FWE\ [FactoryWarrantedEfficiency] \\ 44\% & FME\ [FactoryMeasuredEfficiency] \end{cases} \tag{4.20}$$

where P_A is the photopeak counts number, A the source activity and l_t the acquisition live time.
Using a ^{60}Co source, 25 cm far from the detector and having an activity of $726.8Bq \pm 3\%$, the germanium relative efficiency, according to equation 4.20, is 41.13%, in agreement with the tabulated value. It follows that

$$\epsilon_{abs} = \epsilon_{rel} \cdot \epsilon_{NaI} = 0.049\% \tag{4.21}$$

[3]The calculated efficiency value refers to a detector-source distance of 25 cm.

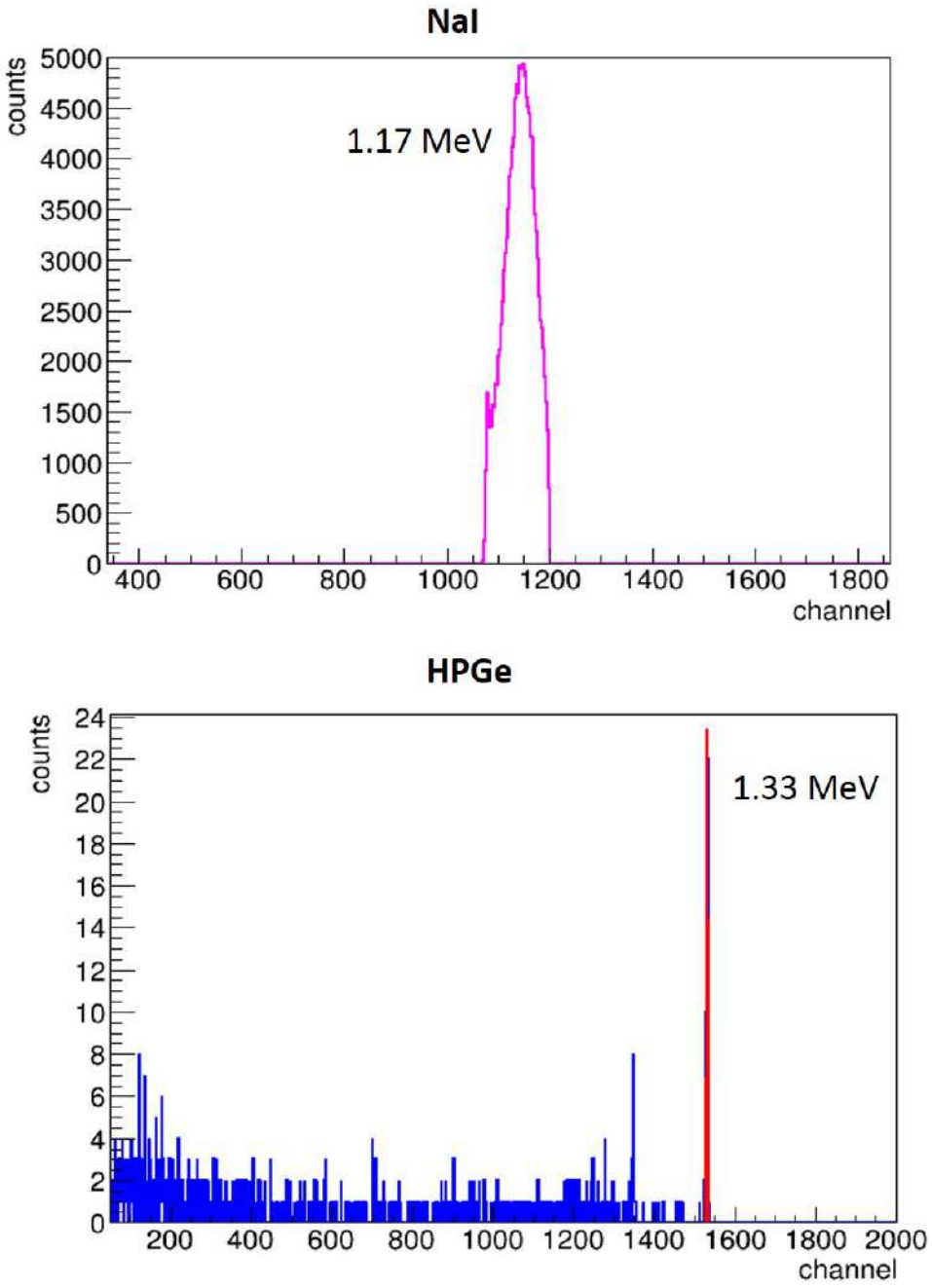

Figure 4.24: The NaI and the HPGe spectra acquired in coincidence configuration. On the top the NaI coincidence spectrum. On the bottom the HPGe one.

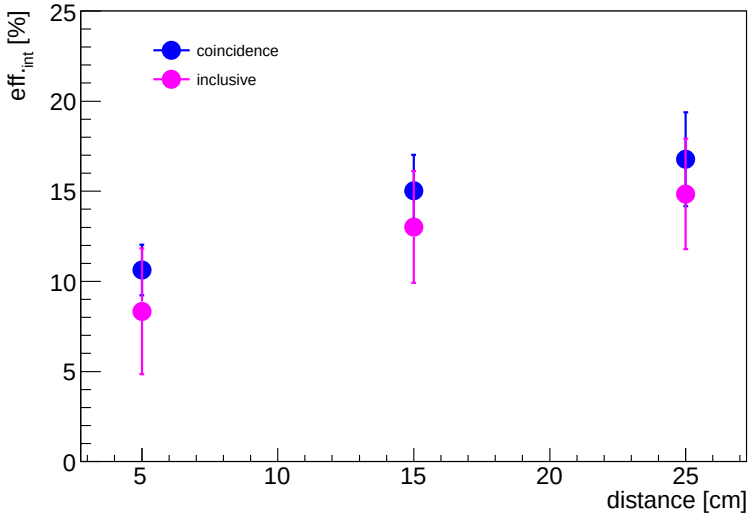

Figure 4.25: Comparison between the germanium efficiency calculated by inclusive method (magenta points) and by coincidence method (blue points).

$$\epsilon_{int} = \epsilon_{abs} \cdot \frac{4\pi}{\Omega} = 14.85\% \tag{4.22}$$

In this case the uncertainty has been calculated propagating the error on the counts number, on the source activity and on the solid angle.
The entire procedure, both for the direct measurement of the efficiency and the coincidence method, has been repeated changing the source-detector distance from 25 cm down to 5 cm. The comparison between the efficiency values calculated using the two methods (figure 4.25) shows a good agreement within the error bar, proving the validity of the coincidence measurement technique.

Efficiency measurement at LUNA

The experimental set-up used at LNGS is schematically drawn in figure 4.26: the HPGe detector (Ge1 in figure), whose efficiency has to be evaluated, is fixed at the centre of the interaction chamber, while the trigger HPGe detector (GE2 in figure) is placed on a movable support moved along the beam axis for all the target length, in 1.5 cm steps, following the source position inside the chamber. This allows the $\gamma-$rays position to be precisely identified, thanks also to a lead collimator having a fissure 1 cm wide put on the Ge2 crystal. In this way the Ge1 efficiency is evaluated for $\gamma-$rays

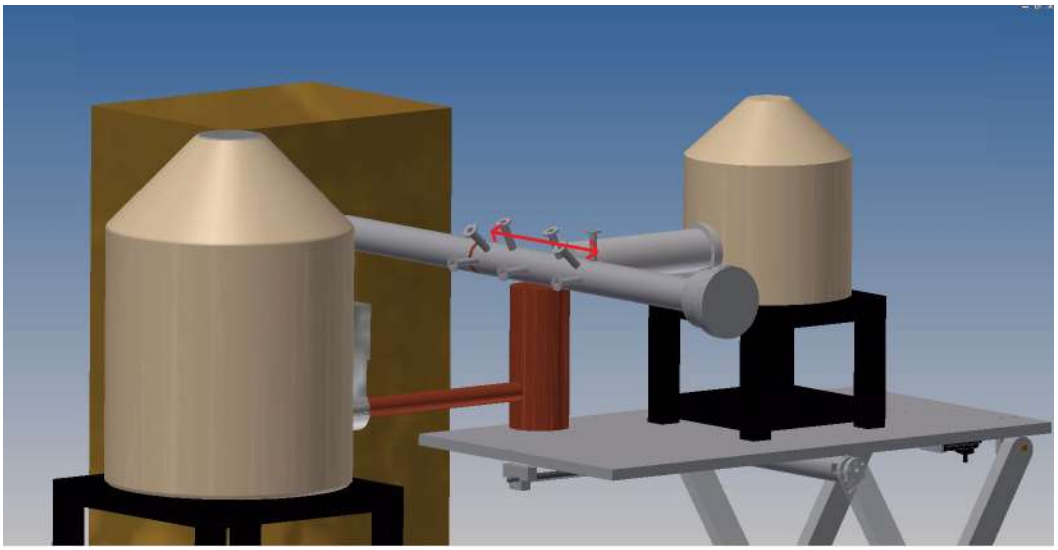

Figure 4.26: Sketch of the coincidence method applied to the 1.3 MeV and 6.1 MeV gammmas.

coming from all the target length.
The main decay channel of the ^{14}N(p,γ)^{15}O resonance at E_r = 259 keV (BR=57.8 %) is particularly useful to determine the germanium efficiency, because it is composed by 2 photons with energy E_{γ_1} = 1384 keV (close to the energy of ^{60}Co $\gamma-$rays, used for investigating the low energy range) and E_{γ_2} = 6172 keV (close to the energy of photons produced by the ^{2}H(p,γ)^{3}He reaction). Figure 4.27 shows the level scheme of the ^{15}O where the coloured arrows indicate the two gamma rays in cascade used for the calibration: the one at 1.3 MeV is used for triggering the reference germanium, the other at 6.1 MeV is used for calibrating the acquisition HPGe (figure 4.26). The $\gamma-\gamma$ angular correlation has to be taken into account for the ^{15}O cascade: knowing the angular momenta and the parity of the intermediate and final states (figure 4.27) $W(\theta)$ has been evaluated for all the three resonances cascades and plotted as a function of the angle θ in figure 4.28.

Currently the data analysis of the germanium phase is still ongoing, so no final efficiency evaluation is available. However the ^{14}N(p,γ)^{15}O spectra acquired by both the germanium detectors are shown in the following. Figure 4.29 (c) shows the trigger germanium spectrum acquired in coincidence configuration, where only the peak selected by the single channel analyser is evident. Figure 4.29 (a) and (b), instead, illustrates the comparison between the spectrum acquired by Ge1 in inclusive and in coincidence configuration showing how, in this last case, only the peak at 6.1 MeV, together with its

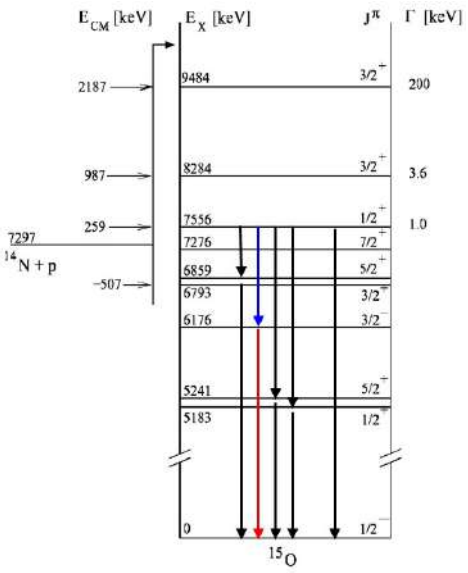

Figure 4.27: Level scheme of ^{15}O near the $^{14}\mathrm{N(p,\gamma)^{15}O}$ threshold.

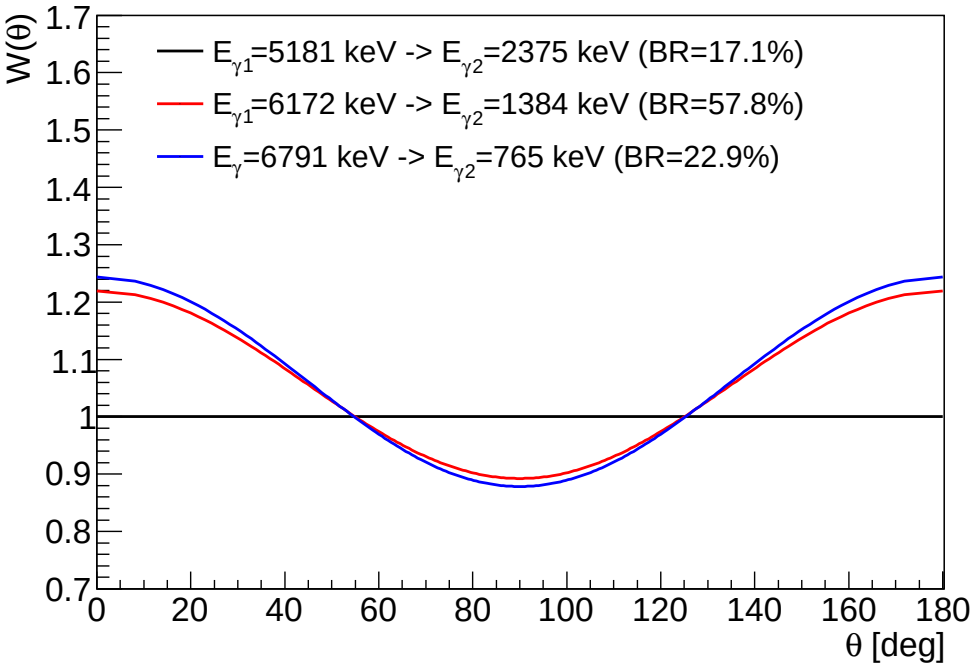

Figure 4.28: Angular correlation function of the three $^{14}\mathrm{N(p,\gamma)^{15}O}$ resonance cascades at $E_r = 259$ keV.

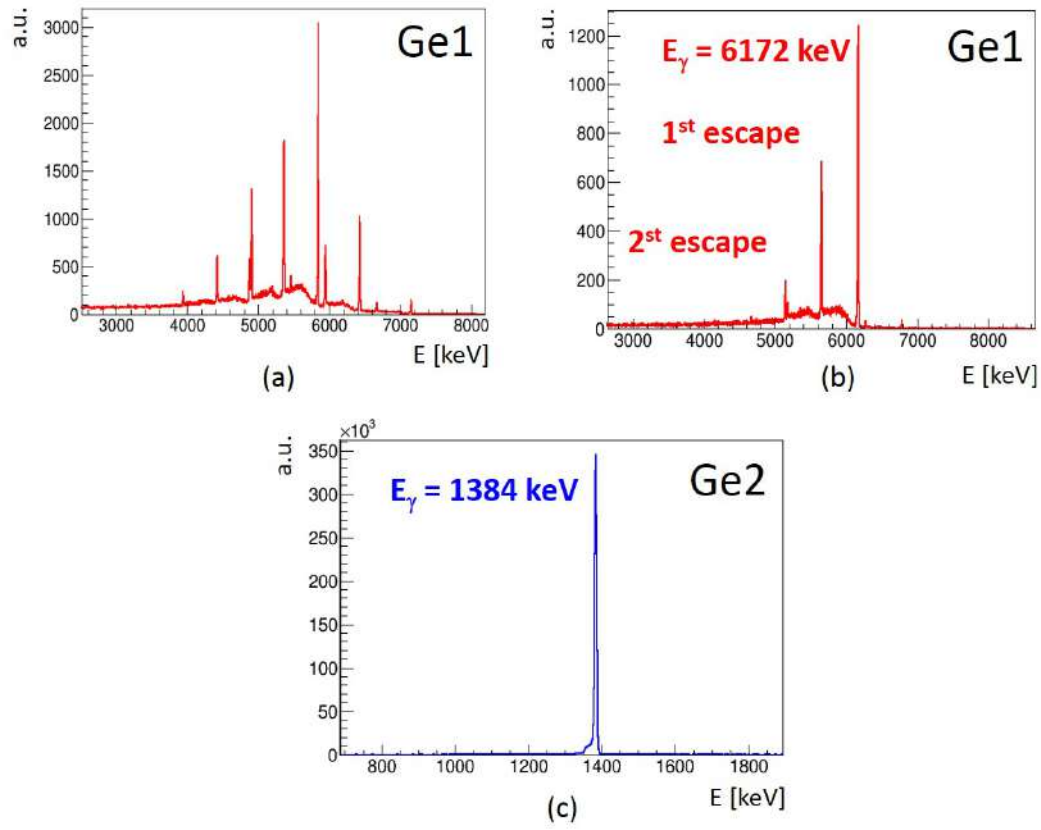

Figure 4.29: ^{14}N(p,γ)^{15}O resonance spectra: (a) Ge1 in inclusive configuration, (b) Ge1 in coincidence configuration, (c) Ge2 in inclusive configuration, with the SCA energy cut at 1384 keV.

first and second escape, are present.

CHAPTER 5

Final results and conclusions

The progress on direct observations of deuterium abundance [16] and the accuracy of CMB data [18] make the lack of ^{2}H(p, γ)^{3}He reaction data at BBN energies the main obstacle to derive the baryon density of the Universe with high accuracy, similar to the one obtained by CMB experiments and to constrain the existence of the so called "dark radiation", composed by undiscovered relativistic species permeating the Universe, such as sterile neutrinos. This is the reason why the LUNA collaboration has measured this reaction cross section in the energy range $30 < E_{c.m.} < 260$ keV, with the goal of reaching an accuracy of a few percent level to solve the tension between data and nuclear calculations and to improve the current 9% uncertainty quoted in the literature data.

The S-factor obtained in the present work is plotted in figure 5.1 together with the literature values in a wide energy range from 0 to 1 MeV: an expected polynomial trend, compatible with the ^{2}H(p, γ)^{3}He behaviour at lower and higher energies, is verified. The values calculated in this thesis work are constantly higher than Ma et al. data: at the lowest energy there is a difference of about 9%, while at the higher values the discrepancy between the two data sets varies from 21% to 33%. It is important to point out that the uncertainty of the present experimental data has been reduced from the previous 9% to about 3%, as reported in table 4.3.
The residual plot in figure 5.2 shows the discrepancy between the theoretical predictions and the two sets of experimental data in the BBN energy range. Since in [31] the S-factor values are tabulated as a function of discrete energy values, the difference with the experimental data is evaluated using a cubic

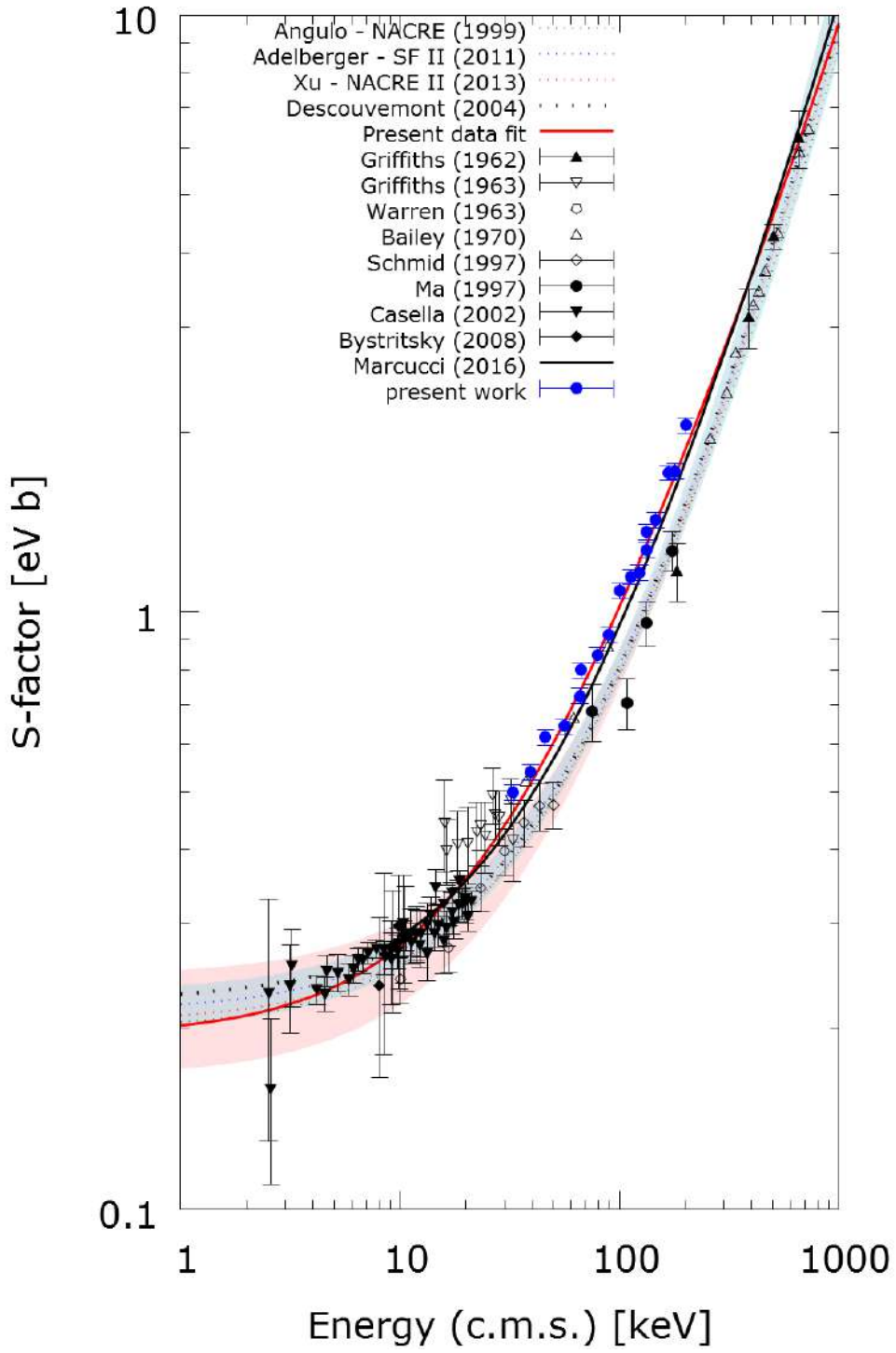

Figure 5.1: $^{2}\mathrm{H}(\mathrm{p},\gamma)^{3}\mathrm{He}$ S-factor plotted as a function of the centre of mass energy. The blue points are the results of the present work.

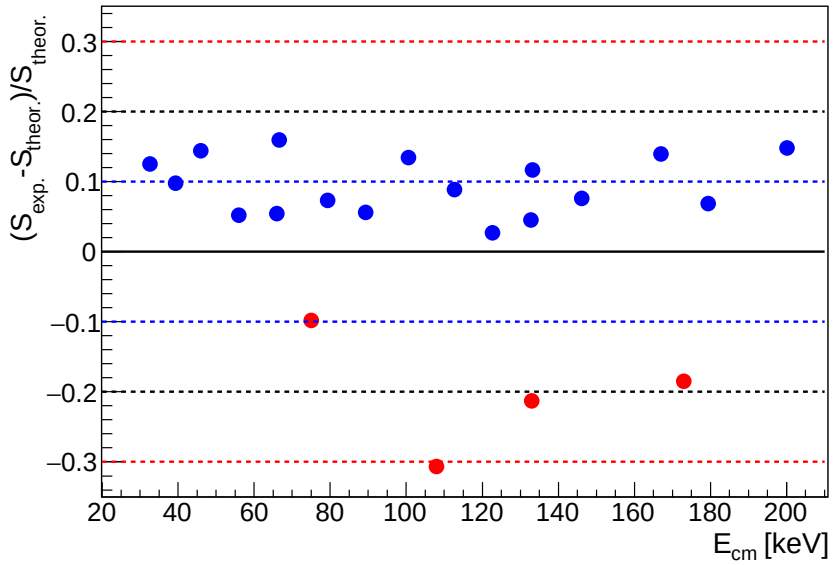

Figure 5.2: Residual plot between the theoretical trend and two data sets (Ma and LUNA).

spline interpolation of the theoretical points. The percentage moving of the experimental data from the theoretical predictions is about 20-30% between Ma data and Marcucci calculations, while a 10-15% discrepancy is found with the LUNA data points.
As stressed in section 2.5, in [27] the authors evaluated the [23], [21], [26] and [19] data, determining the S-factor as a function of the centre of mass energy by fitting the four data sets by a quadratic polynomial in energy (E). Using the same references, with [23] as the only data set available at high energies and substituting the Ma et al. values with the present ones, a new fit has been performed (the red line in figure 5.2):

$$Present\ work \rightarrow S(E) = 0.1948 + 8.1251 \left(\frac{E}{MeV}\right) + 1.392 \left(\frac{E}{MeV}\right)^2 \quad (5.1)$$

$$SF\ II\ [27] \rightarrow S(E) = 0.2145 + 5.5612 \left(\frac{E}{MeV}\right) + 4.6581 \left(\frac{E}{MeV}\right)^2 \quad (5.2)$$

Presently the fit obtained with the BGO data is processed by the PArthENoPE code to compute the new primordial abundances of light elements: starting from nuclear statistical equilibrium conditions the code solves a set of coupled ordinary differential equations, follows the departure from chemical equilibrium of nuclear species and determines their asymptotic abundances as a

function of several input cosmological parameters, as the baryon density and the number of neutrinos families. Until this moment the rate adopted for the ^{2}H(p,γ)^{3}He reaction in the program is taken from the S-factor fit by Adelberger et al. [27], obtaining $^2H/H = 2.61 \cdot 10^{-5}$. As well shown in figure 5.1, the higher reaction cross section, and consequently the higher S-factor, calculated in the present work should lead to a greater deuterium consumption and thus to a lower primordial abundance. In fact, assuming the same baryonic density $\Omega_b h^2 = 0.02226$, the new deuterium abundance evaluation lead to $^2H/H = 2.42 \cdot 10^{-5}$, about 7.3% less than the previous estimation.

At the moment the present goal to measure the ^{2}H(p,γ)^{3}He cross section at the BBN energies with high accuracy has been reached. The data analysis of the HPGe measurement phase should improve the energy range investigated, from the current 200 keV to 360 keV, and provide the angular distribution of the emitted photons, never measured before. Currently most of the experimental data are below 1 MeV, with the only exception of [48] where the cross section has been evaluated in the energy region between 1.7 and 2.3 MeV and with a high uncertainties. Measurements at higher energies will allow to cover a wide range leading to a much better description of the astrophysical factor for this reaction.

APPENDIX A

Brief introduction to cosmology

Our current understanding of the evolution of the universe is based on the hot Big Bang model, known as the standard cosmology.
One of the most fundamental features of the standard cosmology is the expansion of the universe. It was postulated by Hubble thanks to the observation of the galaxy spectra lines redshifts. Plotting the redshift z versus the distance r he found a linear relation, known as the *Hubble law*:

$$z = \frac{H}{c} r \tag{A.1}$$

where the constant of proportionality H is called Hubble constant. Interpreting the redshift as Doppler shift the previous law takes the form

$$v = Hr \tag{A.2}$$

where v is the velocity at which the galaxy moves.
The common unit used to measure the speed of a galaxy is Km/s, while the distance to nearby galaxies is measured in $Megaparsec$ (Mpc) equal to 3.26 million light years. Thus, since the Hubble constant can be obtained by dividing velocity by distance, the unit is $km\, s^{-1}\, Mpc^{-1}$.
Since the distance between two objects is changing over time due to the expansion of the universe, a cosmic scale factor $a(t)$ is introduced as a function of the time to relate the comoving distances[1] for an expanding universe with

[1]Comoving frame is a coordinate system where an observer moves with the Hubble's flow of space expansion and perceives the universe and the cosmic microwave background

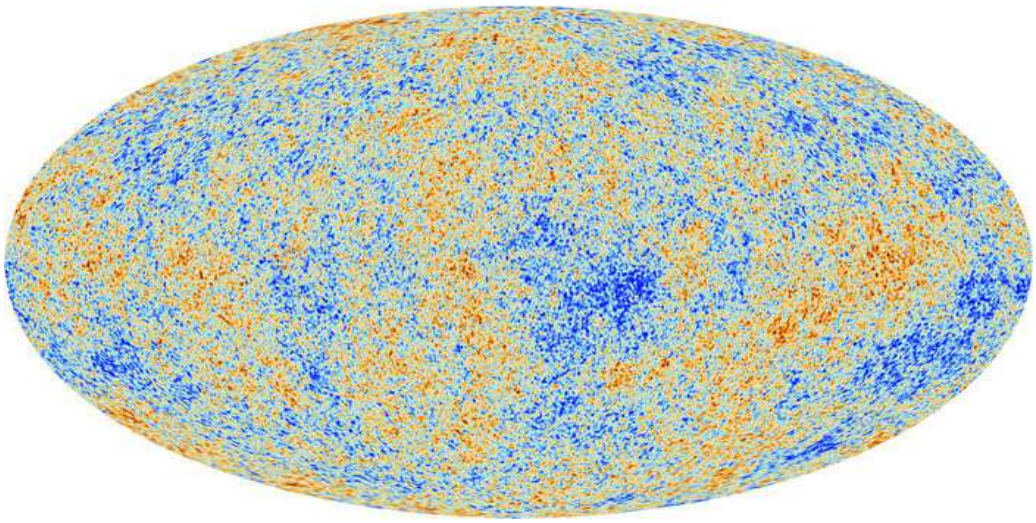

Figure A.1: Cosmic Microwave Background seen by the Plank satellite.

the distance at a reference time, arbitrarily taken to be the present. The proper distance $x(t)$ corresponding to a particular time is thus defined as $x(t) = a(t)r$. It follows that $v = \dot{a}(t) \times r = \dot{a}(t)\frac{x(t)}{a(t)}$ and thus $\frac{\dot{a}(t)}{a(t)} = H$.

A cornerstone of the standard cosmology is the fact that the Universe is homogeneous and isotropic, meaning that its properties are very similar at every point and that there are no preferential directions in space. This assumption dates back to the earliest work of Einstein, who made the assumption not based upon observations, but to simplify the mathematical analysis. Experimental proofs of isotropy and homogeneity has been approached using a number of methods. One of the most convincing observations is referred to as the Cosmic Microwave Background Radiation (CMBR) [49].

The CMBR fills the entire Universe and is leftover radiation from the Big Bang. When the Universe was born, nearly 14 billion years ago, it was filled with hot plasma of particles and photons. In particular, for roughly the first 380,000 years, the photons were constantly interacting with free electrons, meaning that they could not travel long distances. That means that the early Universe was opaque. However, the Universe was expanding and as it expanded, it cooled, as the fixed amount of energy within it was able to spread out over larger volumes. After about 380,000 years, it had cooled to around 3000 Kelvin and at this point, electrons were able to combine with protons to form hydrogen atoms, and the temperature was too low to

radiation to be isotropic. So, for a given pair of comoving objects, while the proper (physical) distance between them grows with the expansion of space, the comoving distance between them remains constant at all times.

separate them again. In the absence of free electrons, the photons were able to move unhindered through the Universe: it became transparent. Over the intervening billions of years, the Universe has expanded and cooled greatly. Due to the expansion of space, the wavelengths of the photons have grown (they have been "redshifted") to roughly 1 millimetre and thus their effective temperature has decreased to just 2.7 Kelvin. These photons fill the Universe today and create a background glow that can be detected by far-infrared and radio telescopes (figure: A.1).

APPENDIX B

Technical drawings of the HPGe phase target chamber

In the following the technical drawings used for realizing the HPGe phase interaction chamber are reported.

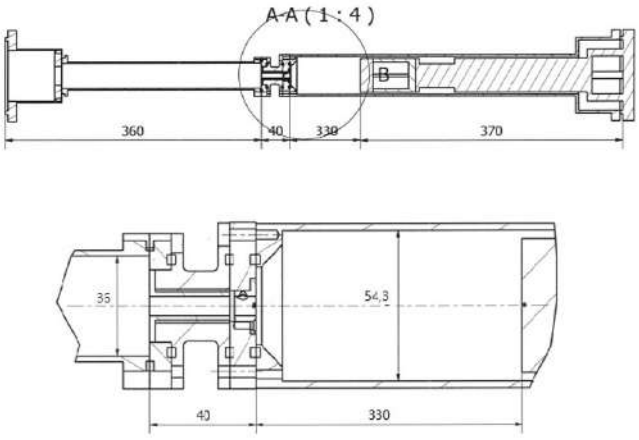

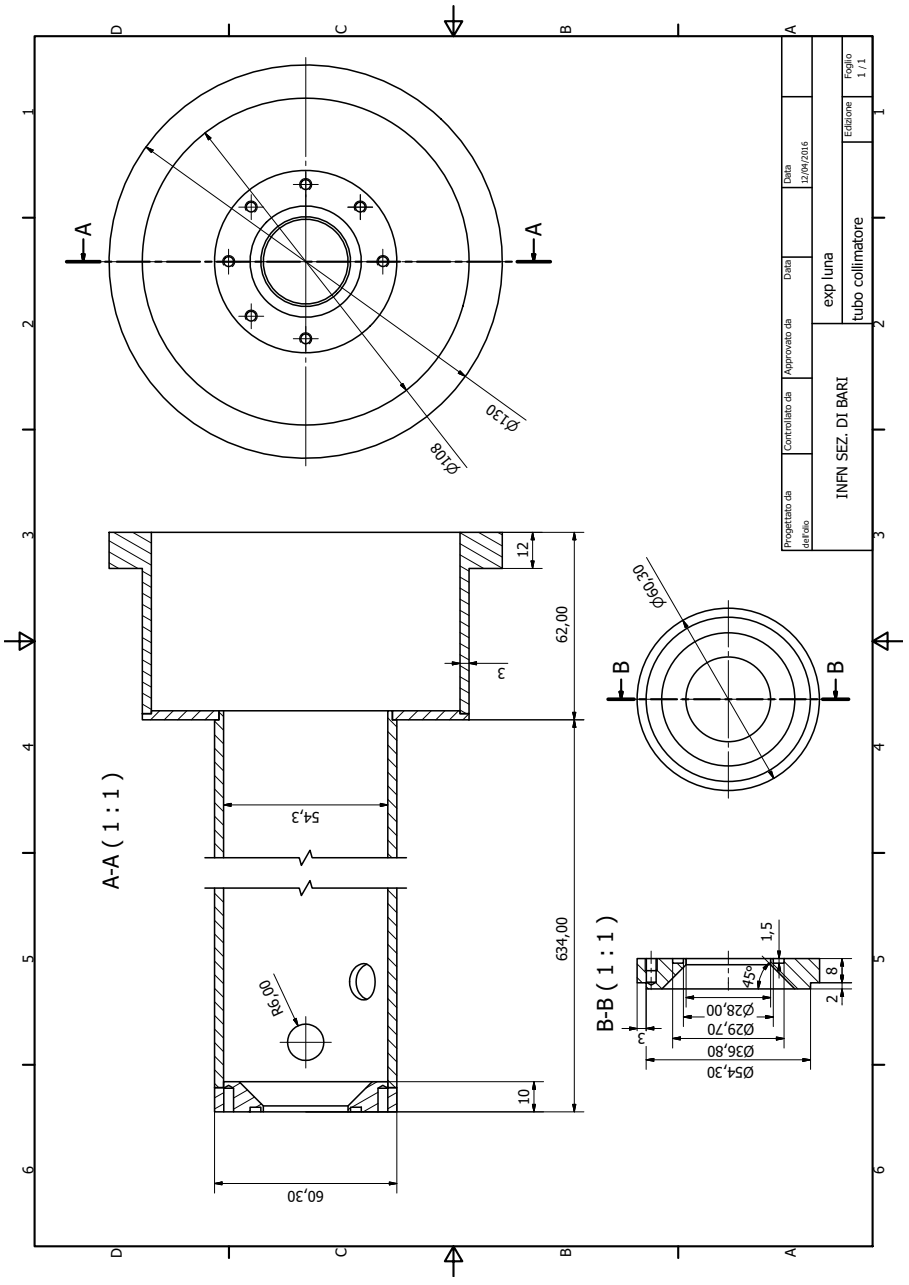
INFN SEZ. DI BARI
exp luna
tubo collimatore
Progettato da dell'oio
Controllato da
Approvato da
Data
Data 12/04/2016
Edizione
Foglio 1 / 1
A-A (1 : 1)
B-B (1 : 1)
Ø130
Ø108
Ø60,30
54,3
62,00
634,00
60,30
R6,00
12
3
10
1,5
45°
8
2
Ø54,30
Ø36,80
Ø29,70
Ø28,00

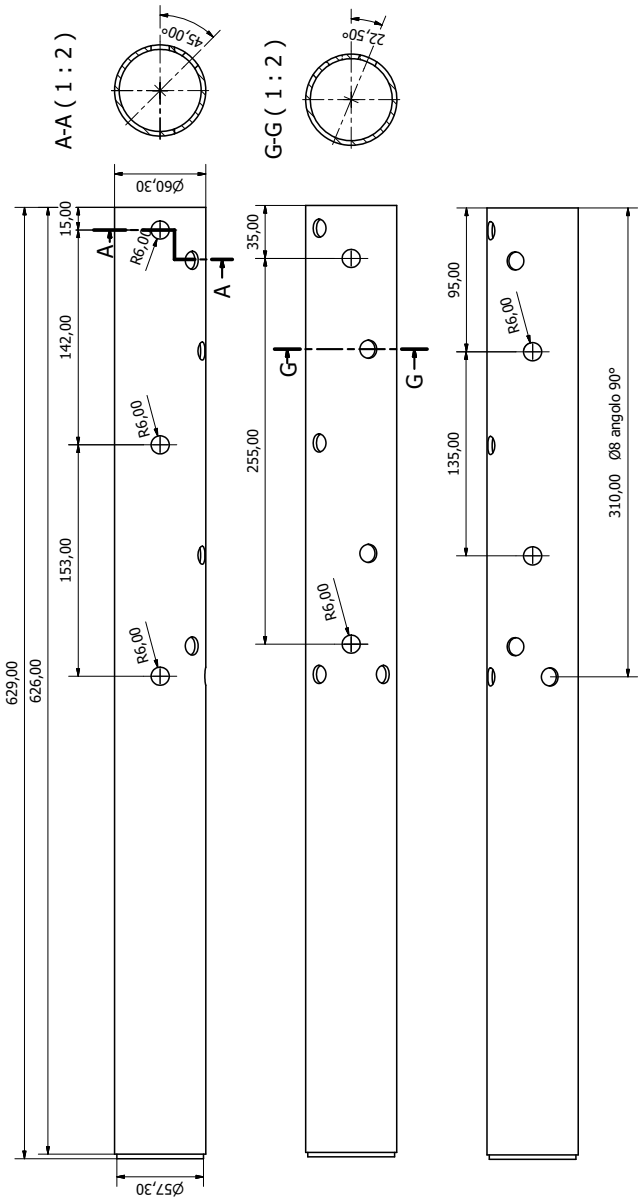
A-A (1 : 2)
45,00°
G-G (1 : 2)
22,50°
Ø60,30
15,00
142,00
153,00
629,00
626,00
R6,00
A
A
35,00
255,00
G
G
95,00
135,00
310,00 Ø8 angolo 90°
Ø57,30

Bibliography

[1] C. E. Rolfs and W. S. Rodney, *Cauldrons in the Cosmos* (The University of Chicago Press, 1988).

[2] A. Finn, *Fundamental University Physics* (Addison-Wesley Publishing Company, 1968).

[3] C. Iliadis, *Nuclearb Physics of Stars* (Wiley-VCH, Weinheim, 2007).

[4] H. Costantini *et al.*, Rep. Prog. Phys. **72**, 086301 (2009).

[5] F. Iocco *et al.*, Phys. Rep. **472**, 1 (2009).

[6] W. Yao *et al.*, J. Phys. **33**, 1232 (2006).

[7] G. Steigman, Annu. Rev. Nucl. Part. Sci. **57**, 463 (2007).

[8] B. Ryden, *Introduction to cosmology* (Addison-Wesley, 2003).

[9] M. Roos, *Introduction to Cosmology* (John Wiley & Sons, Ltd, 2003).

[10] J. Lesgourgues *et al.*, Adv. High Energy Phys. **2012**, 608515 (2012).

[11] S. Weinberg, *Cosmology* (Oxford University Press, 2008).

[12] R. H. Cyburt *et al.*, Astropart. Phys. **17**, 87 (2002).

[13] G. Steigman *et al.*, Phys. Lett. B **66**, 202 (1977).

[14] E. Di Valentino *et al.*, Phys. Rev. D **90**, 023 543 (2014).

[15] O. Pisanti *et al.*, Phys. Commun. **178**, 956 (2008).

[16] R. J. Cooke *et al.*, Ap. J. **781**, 31 (2016).

[17] R. H. Cyburt, Phys. Rev. D **70**, 023505 (2004).

[18] P. collaboration, A&A **594 A13**, 63 (2016).

[19] C. Casella *et al.*, Nucl. Phys. **A 706**, 203 (2002).

[20] G. Griffiths *et al.*, Can.J.Phys. **41**, 724 (1963).

[21] J. Schmid *et al.*, Phys. Rev. C **56**, 2565 (1997).

[22] V. M. Bystritsky *et al.*, Nucl. Inst. Meth. A **595**, 543 (2008).

[23] G. Griffiths *et al.*, Can.J.Phys. **40**, 402 (1962).

[24] G. Bailey *et al.*, Can. J. Phys. **48**, 3059 (1970).

[25] J. B. Warren *et al.*, Phys. Rev. **132**, 1691 (1963).

[26] L. Ma *et al.*, Phys. Rev. C **55**, 588 (1997).

[27] E. G. Adelberger *et al.*, Rev. Mod. Phys **83**, 195 (2011).

[28] C. Angulo *et al.*, Nucl. Phys. A **656**, 3 (1999).

[29] Y. Xu *et al.*, Nucl. Phys. A **918**, 61 (2013).

[30] P. Descouvemont *et al.*, At. Data Nucl. Data Tab. **88**, 203 (2004).

[31] L. E. Marcucci *et al.*, Phys. Rev. Lett. **116**, 102501 (2016).

[32] R. Wiringa *et al.*, Phys. Rev. C **51**, 38 (1995).

[33] B. Pudliner *et al.*, Phys. Rev. Lett. **74**, 4396 (1995).

[34] R. J. Cooke *et al.*, Astr.Ph. J. **781:31**, 16 (2014).

[35] C. Broggini *et al.*, Annu. Rev. Nucl. Part. Sci. **60**, 53 (2010).

[36] A. Formicola *et al.*, Nucl. Inst. Meth. **A 507**, 609 (2003).

[37] F. Ferraro, *Direct measurement of the* $^{22}Ne(p,\gamma)^{23}Na$ *reaction cross section at astrophysical energies*, PhD thesis, Università degli Studi di Genova, 2017.

[38] C. Casella *et al.*, Nucl. Inst. Meth. **A 489**, 160 (2002).

[39] J. F. Ziegler *et al.*, The stopping and the range of ions in matter., SRIM Co, Cester, Maryland, 2008.

[40] C. Melcher *et al.*, Nucl. Inst. Meth. **B 40**, 1214 (1989).

[41] J. Görres *et al.*, Nucl. Inst. Meth. **177**, 295 (1980).

[42] D. Bemmerer *et al.*, Nucl. Phys. **A 779**, 297 (2006).

[43] M. Marta *et al.*, Nucl. Inst. Meth. **A 569**, 727 (2006).

[44] G. F. Knoll, *Radiation Detection and Measurement* (John Wiley and Sons, Inc., 1999).

[45] C. Daigle *et al.*, Phys. Rev. C. **94**, 025803 (2016).

[46] L. Keszthelyi *et al.*, Nucl. Phys. **29**, 241 (1962).

[47] R. D. Evans, *The atomic nucleus* (McGraw-Hill Book Company, 1955).

[48] K. N. Geller *et al.*, Nucl. Phys. A **96**, 397 (1967).

[49] E. W. Kolb and M. S. Turner, *The Early Universe* (Addison-Wesley Publishing Company, 1989).